5-2018

# The Role of CO2 Sublimation in Mass Wasting and Landscape Evolution Under Martian Conditions

Matthew Edwin Sylvest
*University of Arkansas, Fayetteville*

# The Role of $CO_2$ Sublimation in Mass Wasting and Landscape Evolution Under Martian Conditions

A dissertation submitted in partial fulfilment
of the requirements for the degree of
Doctor of Philosophy in Space and Planetary Sciences

by

Matthew Edwin Sylvest
Texas A&M University
Bachelor of Science in Mechanical Engineering, 1990

May 2018
University of Arkansas

This dissertation is approved for recommendation to the Graduate Council.

_____
John C. Dixon, Ph.D.
Dissertation Director

_____
Larry A. Roe, Ph.D.
Committee Member

_____
Kristopher Brye, Ph.D.
Committee Member

_____
Richard Ulrich, Ph.D.
Committee Member

_____
Susan J. Conway, Ph.D.
Ex-officio Committee Member

**Abstract**

Here we present the first set of laboratory experiments under martian atmospheric conditions which demonstrate that the sublimation of $CO_2$ ice from within the sediment body can trigger failure of unconsolidated, regolith slopes, and can measurably alter the landscape. Previous theoretical studies required $CO_2$ slab ice for movements, but we find that only frost is required. Hence, sediment transport by $CO_2$ sublimation could be more widely applicable (in space and time) on Mars than previously thought. This supports recent work suggesting $CO_2$ sublimation could be responsible for recent modification in martian gullies.

A second set of experiments were carried out under martian conditions, investigating the influence of initial slope angle and sediment grain size through on the rate of triggered sediment movement, and on the type of movement (*e.g.*, granular flow or creep). Where the initial study used JSC Mars-1 regolith simulant exclusively, near the angle of repose, these experiments added fine and coarse sand at slope angles down to 10°. We find that the Mars regolith simulant is active down to 17°, the fine sand is only active near the angle of repose and the coarse sand shows negligible movement. Based on our analytical model, motion should be possible at even lower slope angles under martian gravity. We conclude that these mass wasting processes could currently be involved in shaping martian gullies, and intriguingly, $CO_2$-creep process observed in our experiments could provide an alternative explanation for putative solifluction lobes on Mars.

While the sublimation of water ice is a familiar landscape process on Earth, the sublimation of $CO_2$ frost under Mars conditions is not. A comparison of experiments conducted under terrestrial atmospheric conditions with the experiments conducted under martian conditions was performed. We conclude that the rate of pressurization within the pore space of sediment slopes controls both the type and amount of mass wasting triggered. Further, we

propose that the rates of sublimation for water ice under terrestrial conditions are too low to trigger mass wasting, evolving water vapor having ample time to diffuse through the pore space and vent to the atmosphere.

**Acknowledgements**

To Dr. John Dixon, I still remember our first conversation when you helped me understand how I might make myself useful as a planetary scientist. I thank you for your guidance, encouragement and friendship.

To Dr. Susan Conway, I thank you for sharing your expertise and enthusiasm. Working with you has been one of the highlights of this endeavor.

To Dr. Manish Patel, thank you for your generous support and for allowing me to join your team. The worst day in the lab is still a very good day.

**Dedication**

I dedicate this work to my wife, Onedia, who encourages and supports me in all that I do. Recognising my love of "Space" and "Science", she helped me find the path upon which we place this milestone.

I also dedicate this work to my parents, Edwin and Compton Sylvest, who nurtured my curiosity and creativity. They instilled in me a passion for learning, which I share with my sister, Evelyn Sylvest, who inspires me with her own achievements.

Table of Contents

**List of Tables**

**List of Figures**

**List of Published Papers**

Chapter Two:
Sylvest, M.E., Conway, S.J., Patel, M.R., Dixon, J.C., Barnes, A., 2016. Mass wasting triggered by seasonal $CO_2$ sublimation under Martian atmospheric conditions: Laboratory experiments. *Geophysical Research Letters*, 43, 12,363-12,370. https://doi.org/10.1002/2016GL071022.

Chapter Three:
Sylvest, M., Dixon, J., Conway, S., Patel, R., McElwaine, J., Hagermann, A., Barnes, A., 2018. $CO_2$ sublimation in martian gullies: laboratory experiments at varied slope angle and regolith grain sizes, *In*: Conway, S.J., Carrivick, J.L., Carling, P.A., de Haas, T. & Harrison, T.N. (eds) *Martian Gullies and their Earth Analogues.* Geological Society, London, Special Publications. https://doi.org/10.1144/SP467.11.

# 1 Introduction

## 1.1 Historical observations

There are many reasons to study Mars. The first priority for the National Aeronautics and Space Administration's (NASA) Mars Exploration Program is to "determine if Mars ever supported life," either past or extant (MEPAG, 2015). Others are focused on terraforming (*e.g.*, Fogg, 1998) and colonisation to preserve the human species (*e.g.*, Badescu, 2009); while still others are driven by simple curiosity. The earliest known astronomical record of Mars is a symbol on the ceiling of the mortuary temple of Ramesses II, the Ramesseum (Figure 1.1), from *c.* 1270 BCE (Parker, 1974). Three thousand years later, with the aid of the telescope, Giancomo Miraldi correctly hypothesised that the "white spots" he observed at the poles of Mars were ice

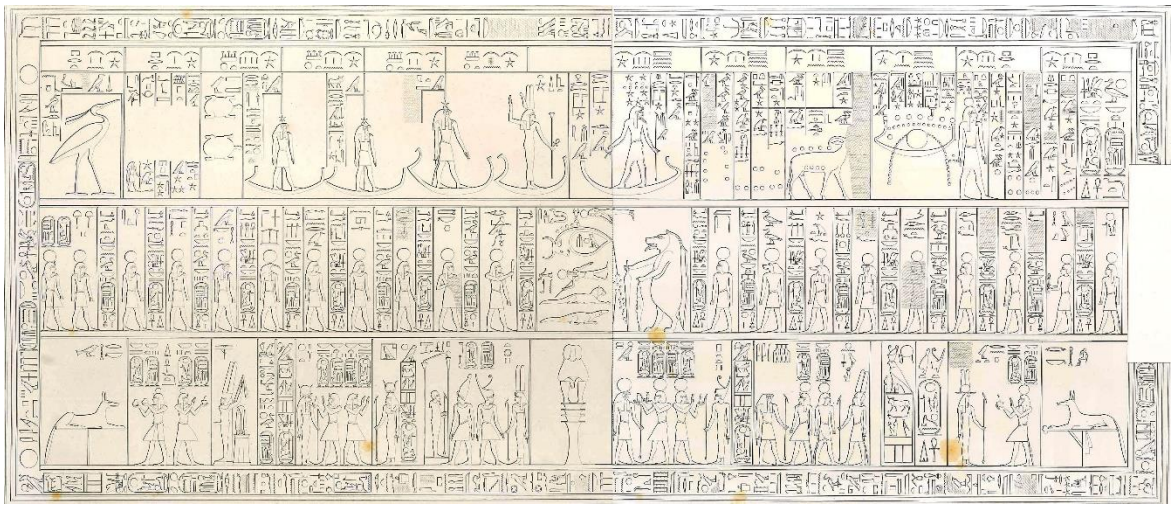

**Figure 1.1.** The astronomical ceiling of the Ramesseum. Tomb of Ramesses II. Image: (Lepsius, 1900)

caps (Silverman, 2017). While many may have imagined that Mars was inhabited, it wasn't until the late 18th century that Sir William Herschel gave voice to the idea by suggesting that "the inhabitants [of Mars] probably enjoy a situation similar to our own," (Herschel, 1784). By the late 19th century, the mapping of martian "canali" by Schiaparelli, fired the imagination of many;

notably, Percival Lowell. In 1906, Lowell published his book "Mars and its Canals," in which he asserts that the canals were part of a global irrigation system, built by martians (Lowell, 1906). Although many astronomers claimed the reported canals did not exist (Robinson et al., 2002), in 1905, Scientific American published photographic evidence (Figure 1.2) of what first Schiaparelli and then Lowell had claimed ("Canals of Mars Photographed," 1905).

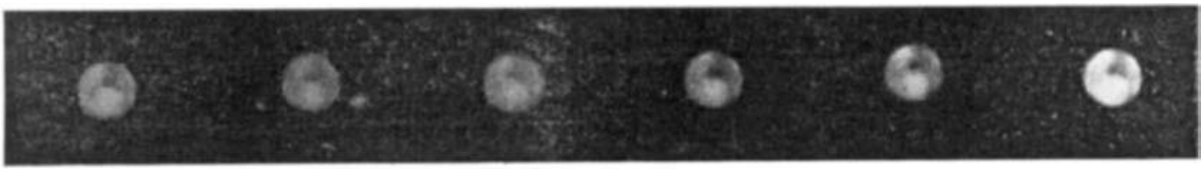

**Figure 1.2.** Photographs of the canals on Mars taken by Dr. Carl Lampland, the assistant director of the Lowell Observatory, ("Canals of Mars Photographed," 1905), for which he won a medal at the Royal Photographic Society of Great Britain's show in 1907.

In the 20th century, speculation about life on Mars turned to the development of hypotheses, as the tools required to identify the essential elements of habitable environments became available. Starting with the July 1965 flyby of Mariner 4, NASA's Mariner missions revealed surprisingly widespread cratering of the martian surface and corrected previous estimates of martian atmospheric pressure (Jones, 2008). While these findings seemed to debase hypotheses for the habitability of Mars, the mapping of Mars by Mariner 9 revealed numerous apparently fluvial features, resembling dry arroyos on Earth (Hartmann and Raper, 1974). Almost three decades later, Malin and Edgett (2000) reported the discovery of gullies on Mars, in images from the Mars Orbiter Camera; further support for a water-formed landscape.

## 1.2 Gullies as Evidence for Water on Mars

The surface of Mars is covered with a wide range of familiar landforms, including volcanos, dunes, canyons and gullies. The similarity of the plan view and 3D morphology of these landforms to their terrestrial counterparts, *e.g.* wet debris flow gullies (Reiss et al., 2011),

or seeping flows (Kreslavsky and Head, 2009), naturally leads to hypotheses for their formation and evolution that are consistent with established models for the terrestrial exemplars.

Among these, gullies are of particular interest as potential markers of habitability, given that terrestrial gullies are primarily formed by the erosion of flowing water (*e.g.*, Kirkby and Bracken, 2009). Ongoing observations have revealed fresh modification and extension of gully channels (Figure 1.3), highlighting the fact that martian gullies are young, active landforms (Diniega et al., 2013; Dundas et al., 2017, 2015, 2012, 2010; Hansen et al., 2013; Pasquon et al., 2017, 2016; Raack et al., 2014), that might reveal the contemporary availability of substantial quantities of liquid water.

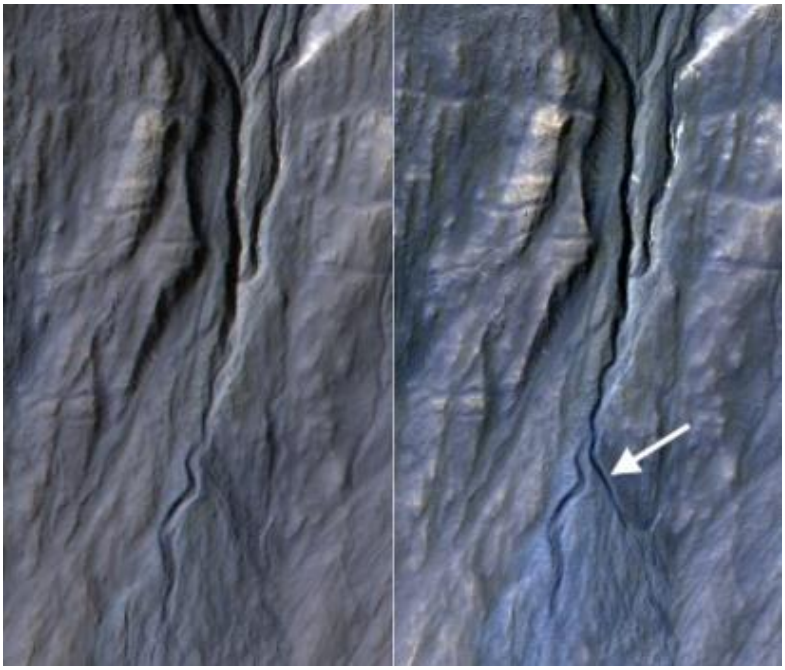

**Figure 1.3.** Image derived from HiRISE observation ESP_030211_1425, illustrating the incision of a new gully channel in the southern highlands Terra Sirenum region. The image on the left is from November 2010, while the image on the right is from May 2013. Credit: NASA/JPL-Caltech/Univ. of Arizona.

## 1.3 Gullies on Earth and Mars

On Earth, classic gullies are frequently defined as permanently incised channel morphologies (Kirkby and Bracken, 2009). When describing martian gullies, Malin and Edgett (2000) identified three characteristic features, including a source alcove, an erosional channel and an alluvial apron (Figure 1.4). This three-part system is now commonly referred to as a classic martian gully. Based on the morphologies of their alcoves, channels and aprons, Auld and Dixon (2016) classified martian gullies into six groups; classic gullies being the largest group, at

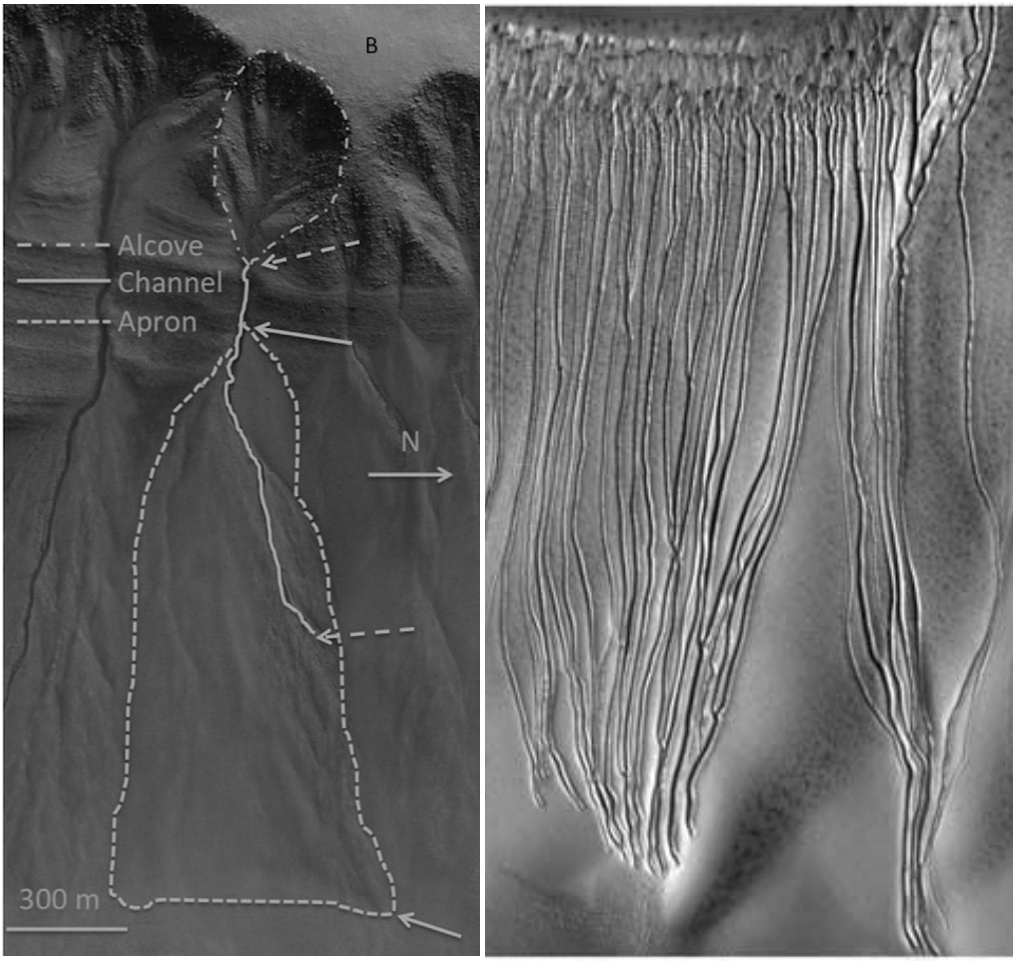


**Figure 1.4.** (left) This image illustrates the classic gully morphology described by Malin & Edgett (2000). The source alcove, transportation channel and depositional apron have been added to HiRISE image ESP_013097_1115 (*Auld and Dixon*, 2016). (right) Linear dune gullies in Russel Crater. HiRISE image PSP_002904_1255, NASA/JPL/University of Arizona.

39.2% of the *c.* 7500 gullies they examined. Of these six groups, most studies have focused exclusively on classic gullies and linear gullies.

Classic gullies are concentrated in two bands in the mid to high latitudes of both northern and southern hemispheres (Figure 1.5). The greatest number of classic gullies (75%) are found in the southern band, between 31°S and 51°S; another 12.5% in the northern band, between 23°N

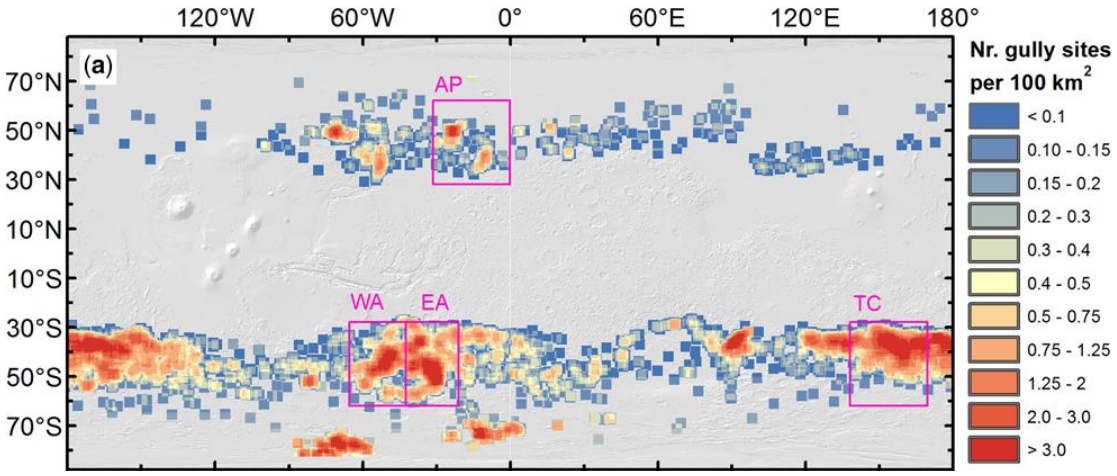


**Figure 1.5.** Distribution of gullies on Mars, represented as the point density of sites observed over 100 km$^2$ regions (Conway et al., 2017).

and 57°N (Auld and Dixon, 2016). Linear gullies (Figure 1.4), present on large sand dunes within the mid-latitudes of both the northern and southern hemispheres (Auld and Dixon, 2016), are long, narrow, levéed grooves, with terminal pits, rather than alluvial fans (Diniega et al., 2013).

While linear gullies are typically situated on pole-facing slopes (Diniega et al., 2013), classic gullies exhibit a strong latitudinal control on orientation (Figure 1.6). Gullies at latitudes less than 40° (north and south) are almost exclusively present on pole-facing slopes; while gullies above 40° are predominantly located on equator-facing slopes, although with more variation than the former (Conway et al., 2017).

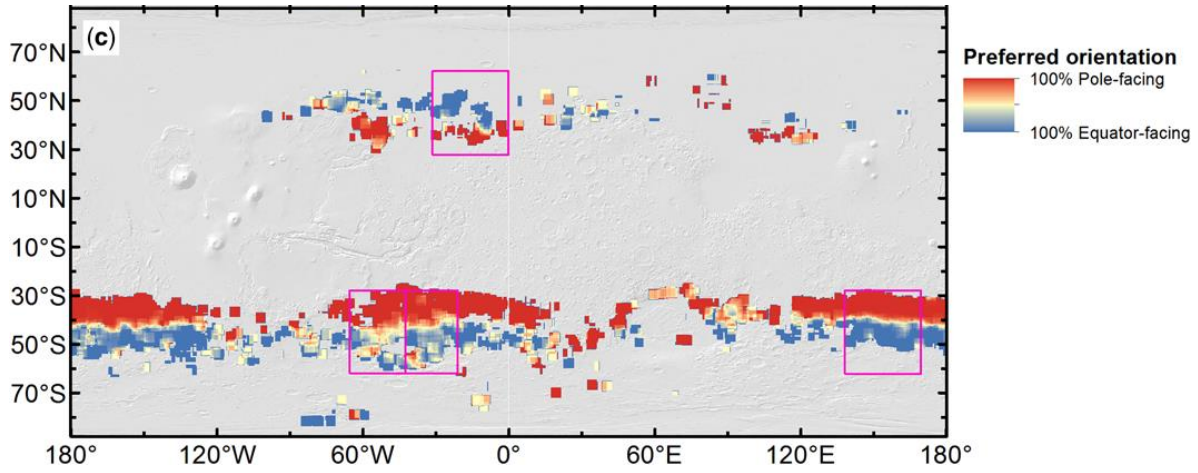


**Figure 1.6.** This map illustrates the relationship between latitude and preferred gully orientation. Notably, gullies at latitudes below 40° are almost exclusively pole-facing, whereas gullies above 40° predominantly face the equator (Conway et al., 2017).

## 1.4 Active Gullies on Mars

Settings of active gullies are not distinct from the global gully population, including mountain slopes, crater walls (Dundas et al., 2015; Harrison et al., 2014; Malin et al., 2006), mid-latitude sand dunes (Diniega et al., 2010b; Harrison et al., 2014; Reiss et al., 2010) and the walls of pits in the south polar region (~71°S) (Hoffman, 2002; Raack et al., 2014). Active gullies, like gullies in general, are concentrated in the southern hemisphere. Reporting on a decade-long survey of gully changes, Dundas et al. (2017) reported that 20% of monitored gullies were active in the southern mid to high-latitudes, and 5% in the northern mid to high-latitudes.

### 1.4.1 Conditions on mars

Mars is currently a cold, arid desert, with surface temperatures ranging from -143°C to 19°C (Haberle et al., 2001), and a maximum of 100 precipitable microns of water vapour (Smith, 2002) in a tenuous 6.1 mbar, 95% $CO_2$ atmosphere (Carr and Head, 2010). Carbon dioxide is abundant, both as a gas, and as solid ice at the surface. Although concentrated in seasonal polar

ice caps (Hess et al., 1979), $CO_2$ ice has been detected on the surface at latitudes down to 32.3° S (Vincendon, 2015). Like Earth, the climate on Mars is seasonal, owing to the tilt of its axis of rotation relative to its orbital plane (25.2° versus 23.4° for Earth). This drives winter expansion and summer retreat of the seasonal ice caps as the ice sublimates into the atmosphere (Hess et al., 1979).

### 1.4.2 Recent activity

Regardless of how they originally formed, gullies are actively changing under current conditions. The apparent lack of liquid water under current Martian surface conditions has increased interest in alternative morphogenetic mechanisms. Several possible agents have been proposed, including surface runoff of water (*e.g.,* Coleman et al., 2009; Conway et al., 2011; Jouannic et al., 2015; Massé et al., 2016) and brines (*e.g.*, Chevrier et al., 2009; Pasquon et al., 2016), slush-flow (Auld and Dixon, 2017), dry granular flows (*e.g.*, Treiman, 2003), debris flows (Védie et al., 2008), gas-fluidized flows (*e.g.*, Pilorget and Forget, 2016; Raack et al., 2017) and flows triggered by the sublimation of seasonal $CO_2$ frost (Sylvest et al., 2018, 2016). The location and timing of gully activity appears to be closely coupled to the occurrence of seasonal $CO_2$ frost, between late winter and early spring (Diniega et al., 2010b; Dundas et al., 2017, 2015, 2012, 2010; Hansen et al., 2015; Pasquon et al., 2017, 2016).

## 1.5 Sublimation of Seasonal $CO_2$ Frost

Recent studies suggest that seasonal freezing and sublimation of $CO_2$ ice could be responsible for present-day gully activity on Mars (Cedillo-Flores et al., 2011; Diniega et al., 2010a; Hansen et al., 2011, 2013). These observations associate the timing of morphological changes in gullies with the seasonal $CO_2$ cycle (Diniega et al., 2010a; Dundas et al., 2014, 2012;

McEwen et al., 2011; Pasquon et al., 2016; Raack et al., 2015; Reiss et al., 2010; Reiss and Jaumann, 2003; Vincendon, 2015), activity consistently observed during late winter, when seasonal frost is beginning to sublimate (Dundas et al., 2017, 2015, 2012, 2010; Hansen et al., 2015; Pasquon et al., 2017, 2016).

## 1.6 Dissertation Goals and Significance

Sublimation is a recognized planetary process (Mangold, 2011). Although primarily identified with pitting or uneven lowering of a surface, sublimation has been implicated as one of several potential mechanisms controlling hillslope processes on Mars (Dundas et al., 2015). However, there are no terrestrial analogues for the action of sublimation in a hillslope context, which hampers the assessment of whether observations are also consistent with formation by sublimation.

### 1.6.1 Previous $CO_2$ sublimation studies

#### 1.6.1.1 Numerical models

Two numerical models have been used to assess the efficacy of downslope transport driven by $CO_2$ slab ice sublimation on Mars. Cedillo-Flores et al. (2011) simulated the fluidization of sediment deposited over sublimating seasonal $CO_2$ frost. Assuming 0.3-100 mm thick layers of sand (100 μm) and dust (3 μm), they calculated whether the sublimation rate of the underlying $CO_2$ would be sufficient to mobilize the sediment on a 25° bed, located at 75°N/S. Results showed that sand was always mobilized, while only dust layers <100 mm thick could be mobilized.

Pilorget and Forget (2016) modeled the mobilization of dry sediment trapped between $CO_2$ slab ice and an underlying water ice-cemented permafrost. This model was optimized for

the linear gullies on the Russell crater megadune at 55°S, exploring slope angles between 10 and 30°. They used a climate model to predict that movements generated this way should be possible anywhere polewards of 60°S and on pole-facing slopes polewards of 25°S.

#### 1.6.1.2 **Experiments**

Only a few experimental studies have examined the potential role of sublimating $CO_2$ frost in hillslope processes. Two of the existing studies, Diniega et al. (2013) and Mc Keown et al. (2017), have focused specifically on linear dune gullies. Diniega et al. (2013) proposed that blocks of $CO_2$ ice could break off from cornices of accumulated seasonal frost, and slide down the dune slopes, levitated by a cushion of $CO_2$ gas. They demonstrated the feasibility of this model by successfully reproducing levied channel forms consistent with linear gully observations in a series of field experiments. Mc Keown et al. (2017) performed laboratory experiments, under terrestrial temperature and pressure that demonstrated the levitation of $CO_2$ ice blocks placed on relatively hot sediment. They also confirmed the potential for the burrowing of these blocks, which might account for terminal pits, unique to linear gullies.

While there have been Mars-focused experimental studies undertaken on the role of slope on the morphological characteristics of slope disturbances under both Earth surface conditions (Coleman et al., 2009; Jouannic et al., 2015) and martian conditions (Jouannic et al., 2015), no studies have systematically examined the role of slope over a range of angles known to support a variety of mass wasting forms, including gullies. Similarly, a few experimental studies have systematically investigated the role of grain size in influencing the movement of debris under Martian atmospheric conditions (Conway et al., 2011). All of these studies, however, examined water flow rather than $CO_2$ frost sublimation.

The overarching motivation behind this study is to investigate the ability of sublimating $CO_2$ to trigger mass wasting and produce hillslope features; and, to constrain the parameters that control the degree and type of slope response. We focus our study on the seasonal (late winter) sublimation of $CO_2$ on Mars for two reasons. Firstly, Mars has a seasonal $CO_2$ condensation-sublimation cycle that is closely linked to many active surface features observed in orbital images (Gardin et al., 2010; Hansen et al., 2011; Kieffer et al., 2006), suggesting a possible causal relationship. Secondly, because ongoing observations and studies of martian hillslope features are more numerous and detailed than those for the other bodies cited above.

## 1.7 Dissertation Outline

Chapter 2 presents a series of experiments that investigate the ability of sublimating $CO_2$ frost to trigger mass wasting of unconsolidated sediment slopes, under martian atmospheric conditions. These experiments were published in *Geophysical Research Letters*, in 2016. A second series of experiments is presented in Chapter 3, which examined the effects of initial slope angle and sediment grain size on mass wasting triggered by $CO_2$ sublimation under martian atmospheric conditions. The results of these experiments were published in the Special Publications series of the Geological Society of London in 2018. Chapter 4 presents a comparison of the results from the experiments of Chapters 2 and 3, performed under martian atmospheric conditions, with experiments conducted under terrestrial conditions. Chapter 5 summarises the conclusions of this research.

## 1.8 References

Anon, 1905. Canals of Mars Photographed. *Scientific American*, 93(6), p.107.

Auld, K.S. & Dixon, J.C., 2017. An experimental investigation into Martian gully formation: a slush-flow model. *In*: Conway, S.J., Carrivick, J.L., Carling, P.A., de Haas, T. & Harrison,

T.N. (eds) *Martian Gullies and their Earth Analogues.* Geological Society, London, Special Publications, 467. https://doi.org/10.1144/SP467.2.

Auld, K.S. & Dixon, J.C., 2016. A classification of martian gullies from HiRISE imagery. *Planetatry and Space Science*, 131, pp.88–101. https://doi.org/10.1016/j.pss.2016.08.002.

Badescu, V., 2009. Mars: *Prospective Energy and Material Resources*, Berlin: Springer. https://doi.org/10.1007/978-3-642-03629-3.

Carr & Head, 2010. Geologic history of Mars. *Earth and Planetary Science Letters*, 294(3), pp.185–203. https://doi.org/10.1016/j.epsl.2009.06.042.

Cedillo-Flores, Y., Treiman, A.H., Lasue, J., Clifford, S.M., 2011. $CO_2$ gas fluidization in the initiation and formation of Martian polar gullies, *Geophysical Research Letters*, 38(21). https://doi.org/10.1029/2011GL049403.

Chevrier, V.F., Ulrich, R., Altheide, T.S., 2009. Viscosity of liquid ferric sulfate solutions and application to the formation of gullies on Mars. *Journal of Geophysical Research*, 114(E6). https://doi.org/10.1029/2009JE003376.

Coleman, K. A., Dixon, J.C., Howe, K.L., Roe, L.A., Chevrier, V., 2009. Experimental simulation of martian gully forms. *Planetary and Space Science*, 57, pp.711–716. https://doi.org/10.1016/j.pss.2008.11.002.

Conway, S.J., Harrison, T.N., Soare, R.J., Britton, A.W., Steele, L.J., 2017. New slope-normalized global gully density and orientation maps for Mars. *In*: Conway, S.J., Carrivick, J.L., Carling, P.A., de Haas, T. & Harrison, T.N. (eds) *Martian Gullies and their Earth Analogues.* Geological Society, London, Special Publications, 467. https://doi.org/10.1144/SP467.3.

Conway, S.J., Lamb, M.P., Balme, M.R., Towner, M.C., Murray, J.B., 2011. Enhanced runout and erosion by overland flow at low pressure and sub-freezing conditions: Experiments and application to Mars. *Icarus*, 211, pp.443–457. https://doi.org/10.1016/j.icarus.2010.08.026.

Diniega, S., Byrne, S., Bridges, N.T., Dundas, C.M., McEwen, A.S., 2010 Seasonality of present-day Martian dune-gully activity. *Geology*, 38(11), pp.1047–1050. https://doi.org/10.1130/G31287.1.

Diniega, S., Hansen, C.J., McElwaine, J.N., Hugenholtz, C.H., Dundas, C.M., McEwen, A. S., Bourke, M.C., 2013. A new dry hypothesis for the formation of martian linear gullies. *Icarus*, 225(1), pp.526–537. https://doi.org/10.1016/j.icarus.2013.04.006.

Dundas, C.M., Diniega, S., Hansen, C.J., Byrne, S., McEwen, A.S., 2012. Seasonal activity and morphological changes in martian gullies. *Icarus*, 220(1), pp.124–143. https://doi.org/10.1016/j.icarus.2012.04.005.

Dundas, C.M., Diniega, S., McEwen, A.S., 2015. Long-term monitoring of martian gully formation and evolution with MRO/HiRISE. *Icarus*, 251, pp.244–263. https://doi.org/10.1016/j.icarus.2014.05.013.

Dundas, C.M., McEwen, A.S., Diniega, S., Byrne, S., Martinez-Alonso, S., Alonso, S.M., Martinez-Alonso, S., 2010. New and recent gully activity on Mars as seen by HiRISE. *Geophysical Research Letters*, 37(7). https://doi.org/10.1029/2009GL041351.

Dundas, C.M., McEwen, A.S., Diniega, S., Hansen, C.J., Byrne, S., McElwaine, J.N., 2017. The formation of gullies on Mars today. *In*: Conway, S.J., Carrivick, J.L., Carling, P.A., de Haas, T. & Harrison, T.N. (eds) *Martian Gullies and their Earth Analogues.* Geological Society, London, Special Publications, 467. https://doi.org/10.1144/SP467.5

Fogg, M.J., 1998. Terraforming Mars: A review of current research. *Advances in Space Research*, 22(3), pp.415–420. https://doi.org/10.1016/S0273-1177(98)00166-5.

Gardin, E., Allemand, P., Quantin, C., Thollot, P., 2010. Defrosting, dark flow features, and dune activity on Mars: Example in Russell crater. *Journal of Geophysical Research: Planets*, 115(E6). https://doi.org/10.1029/2009JE003515.

Haberle, R.M., McKay, C.P., Schaeffer, J., Cabrol, N.A., Grin, E.A., Zent, A.P., Quinn, R., 2001. On the possibility of liquid water on present-day Mars. *Journal of Geophysical Research: Planets*, 106, pp.23317–23326. https://doi.org/10.1029/2000JE001360.

Hansen, C.J., Bourke, M., Bridges, N.T., Byrne, S., Colon, C., Diniega, S., Dundas, C., Herkenhoff, K., McEwen, A., Mellon, M., Portyankina, G., Thomas, N., 2011. Seasonal Erosion and Restoration of Mars' Northern Polar Dunes. *Science (New York, N.Y.)*, 331(6017), pp.575–578. https://doi.org/10.1126/science.1197636.

Hansen, C.J.J., Byrne, S., Portyankina, G., Bourke, M., Dundas, C., McEwen, a., Mellon, M., Pommerol, a., Thomas, N., 2013. Observations of the northern seasonal polar cap on Mars: I. Spring sublimation activity and processes. *Icarus*, 225(2), pp.881–897. https://doi.org/10.1016/j.icarus.2012.09.024.

Hansen, C.J.J., Diniega, S., Bridges, N., Byrne, S., Dundas, C., McEwen, A., Portyankina, G., 2015. Agents of change on Mars' northern dunes: $CO_2$ ice and wind. *Icarus*, 251, pp.264-274. https://doi.org/10.1016/j.icarus.2014.11.015.

Harrison, T.N., Osinski, G.R., Tornabene, L.L., Jones, E., 2015. Global Documentation of Gullies With the Mars Reconnaissance Orbiter Context Camera and Implications for Their Formation. *Icarus*, 252, pp.236-254. https://doi.org/http://dx.doi.org/10.1016/j.icarus.2015.01.022.

Hartmann, W., Raper, O., 1974. The New Mars: The Discoveries of Mariner 9. Scientific and Technical Information Office National Aeronautics and Space Administration, Washington, D.C. NASA-SP-337.

Herschel, W., 1784. On the remarkable appearances at the polar regions of the planet mars, the inclination of its axis, the position of its poles, and its spheroidical figure; with a few hints relating to its real diameter and atmosphere; by William Herschel, Esq. F.R.S. *Philosophical Transactions of the Royal Society of London*, 74, pp.233–273.

Hess, S.L., Henry, R.M., Tillman, J.E., 1979. The seasonal variation of atmospheric pressure on Mars as affected by the south polar cap. *Journal of Geophysical Research: Solid Earth*, 84(B6), pp.2923–2927. https://doi.org/10.1029/JB084iB06p02923.

Hoffman, N., 2002. Active polar gullies on Mars and the role of carbon dioxide. *Astrobiology*, 2(3), pp.313–323. https://doi.org/10.1089/153110702762027899.

Jones, B.W., 2008. Mars before the Space Age. *International Journal of Astrobiology*, 7(2), pp.143–155. https://doi.org/10.1017/S1473550408004138

Jouannic, G., Gargani, J., Conway, S.J., Costard, F., Balme, M.R., Patel, M.R., Massé, M., Marmo, C., Jomelli, V., Ori, G.G., 2015. Laboratory simulation of debris flows over sand dunes: Insights into gully-formation (Mars). *Geomorphology*, 231, pp.101–115. https://doi.org/10.1016/j.geomorph.2014.12.007.

Kieffer, H.H., Christensen, P.R., Titus, T.N., 2006. $CO_2$ jets formed by sublimation beneath translucent slab ice in Mars' seasonal south polar ice cap. *Nature*, 442(7104), pp.793–796. https://doi.org/10.1038/nature04945.

Kirkby, M.J., Bracken, L.J., 2009. Gully processes and gully dynamics. *Earth Surface Processes and Landforms*, 34(14), pp.1841–1851. https://doi.org/10.1002/esp.1866.

Kreslavsky, M.A., Head, J.W., 2009. Slope streaks on Mars: A new "wet" mechanism. *Icarus*, 201(2), pp.517–527. https://doi.org/10.1016/j.icarus.2009.01.026.

Lowell, P., 1906. *Mars and Its Canals*, New York, The Macmillan company; London, Macmillan & co., ltd. [Web.] Retrieved from the Library of Congress. https://lccn.loc.gov/06045164.

Malin, M.C., Edgett, K.S., 2000. Evidence for Recent Groundwater Seepage and Surface Runoff on Mars. *Science*, 288(5475), pp.2330–2335. https://doi.org/10.1126/science.288.5475.2330.

Malin, M.C., Edgett, K.S., Posiolova, L. V, McColley, S.M., Dobrea, E.Z.N., 2006. Present-day impact cratering rate and contemporary gully activity on Mars *Science*, 314(5805), pp.1573–1577. https://doi.org/10.1126/science.1135156

Mars Exploration Program Analysis Group, 2015. Mars Science Goals, Objectives, Investigations, and Priorities: 2015. MEPAG Goals.

Massé, M., Conway, S.J., Gargani, J., Patel, M.R., Pasquon, K., Mcewen, A., Carpy, S., Chevrier, V., Balme, M.R., Ojha, L., Vincendon, M., Poulet, F., Costard, F., Jouannic, G., 2016. Transport processes resulting from metastable boiling water under Mars surface conditions - supplumentary information. *Nature Geoscience*, 9(6), pp.425–428. https://doi.org/10.1038/ngeo2706.

Mc Keown, L.E., Bourke, M.C., McElwaine, J.N., 2017. Experiments On Sublimating Carbon Dioxide Ice And Implications For Contemporary Surface Processes On Mars. *Scientific Reports*, 7(1), p.14181. https://doi.org/10.1038/s41598-017-14132-2.

McEwen, A.S., Ojha, L., Dundas, C.M., Mattson, S.S., Byrne, S., Wray, J.J., Cull, S.C., Murchie, S.L., Thomas, N., Gulick, V.C., 2011. Seasonal flows on warm Martian slopes. *Science (New York, N.Y.)*, 333(6043), pp.740–743. https://doi.org/10.1126/science.1204816.

Parker, R.A., 1974. Ancient Egyptian Astronomy. *Philosophical Transactions of the Royal Society A: Mathematical, Physical & Engineering Sciences*, 276(1257), pp.51–65.

Pasquon, K., Gargani, J., Massé, M., Conway, S.J., 2016. Present-day formation and seasonal evolution of linear dune gullies on Mars. *Icarus*, 274, pp.195–210. https://doi.org/10.1016/j.icarus.2016.03.024.

Pasquon, K., Gargani, J., Nachon, M., Conway, S.J., Massé, M., Jouannic, G., Balme, M.R., Costard, F., Vincendon, M., 2017. Are the different gully morphologies due to different formation processes on the Kaiser dune field? *In*: Conway, S.J., Carrivick, J.L., Carling, P.A., de Haas, T. & Harrison, T.N. (eds) *Martian Gullies and their Earth Analogues.* Geological Society, London, Special Publications, 467.

Pilorget, C., Forget, F., 2016. Formation of gullies on Mars by debris flows triggered by $CO_2$ sublimation. *Nature Geoscience*, 9, pp.65–69. https://doi.org/10.1038/ngeo2619.

Raack, J., Conway, S.J., Herny, C., Balme, M.R., Carpy, S. & Patel, M.R. 2017. Water-induced sediment levitation enhances downslope transport on Mars. *Nature Communications*, 8(1), p.1151. https://doi.org/10.1038/s41467-017-01213-z.

Raack, J., Reiss, D., Appéré, T., Vincendon, M., Ruesch, O., Hiesinger, H., 2015. Present-day seasonal gully activity in a south polar pit (Sisyphi Cavi) on Mars. *Icarus*, 251, pp.226-243. https://doi.org/http://dx.doi.org/10.1016/j.icarus.2014.03.040.

Reiss, D., Erkeling, G., Bauch, K.E., Hiesinger, H., 2010. Evidence for present day gully activity on the Russell crater dune field, Mars. *Geophysical Research Letters*, 37. https://doi.org/10.1029/2009GL042192

Reiss, D., Hauber, E., Hiesinger, H., Jaumann, R., Trauthan, F., Preusker, F., Zanetti, M., Ulrich, M., Johnsson, A., Johansson, L., Olvmo, M., Carlsson, E., Johansson, H.A.B., McDaniel, S., 2011. Terrestrial gullies and debris-flow tracks on Svalbard as planetary analogs for Mars. *Special Paper of the Geological Society of America*, 483, pp.165–175.

Reiss, D., Jaumann, R., 2003. Recent debris flows on Mars: Seasonal observations of the Russell Crater dune field. *Geophysical Research Letters*, 30(6), pp.3–6. https://doi.org/10.1029/2002GL016704.

Moore, P., 2002. "Canals, Martian." *Philip's Astronomy Encyclopedia*, Philip's, p.69.

Silverman, B., 2017. *Mars Missions: A Space Discovery Guide*. Lerner Publications, p.8.

Smith, M.D., 2002. The annual cycle of water vapor on Mars as observed by the Thermal Emission Spectrometer. *Journal of Geophysical Research: Planets*, 107(E11), pp.25–1-25–19. https://doi.org/10.1029/2001JE001522.

Sylvest, M., Dixon, J., Conway, S., Patel, R., McElwaine, J., Hagermann, A., Barnes, A., 2018. $CO_2$ sublimation in martian gullies: laboratory experiments at varied slope angle and regolith grain sizes, *In*: Conway, S.J., Carrivick, J.L., Carling, P.A., de Haas, T. & Harrison, T.N. (eds) *Martian Gullies and their Earth Analogues.* Geological Society, London, Special Publications. https://doi.org/10.1144/SP467.11.

Sylvest, M.E., Conway, S.J., Patel, M.R., Dixon, J.C., Barnes, A., 2016. Mass wasting triggered by seasonal $CO_2$ sublimation under Martian atmospheric conditions: Laboratory experiments. *Geophysical Research Letters*, 43, pp.12,363-12,370. https://doi.org/10.1002/2016GL071022.

Treiman, A.H., 2003. Geologic Settings of Martian Gullies: Implications for Their Origins*Journal of Geophysical Research: Planets*, 108(E4). https://doi.org/10.1029/2002JE001900.

Védie, E. V, Costard, F., Font, M., Lagarde, J.L., 2008. Laboratory simulations of Martian gullies on sand dunes. *Geophysical Research Letters*, 35(21). https://doi.org/10.1029/2008GL035638.

Vincendon, M., 2015. Identification of Mars gully activity types associated with ice composition. *Journal of Geophysical Research: Planets*, 120(11), pp.1859–1879. https://doi.org/10.1002/2015JE004909.

# 2 Mass Wasting Triggered by Seasonal $CO_2$ Sublimation Under Martian Atmospheric Conditions: Laboratory Experiments

M. E. Sylvest[1], S. J. Conway[2,3], M. R. Patel[2,4], J. C. Dixon[1] and A. Barnes[5]

[1]Arkansas Center for Space and Planetary Sciences, University of Arkansas, Fayetteville, Arkansas, USA.

[2]School of Physical Sciences, Open University, Milton Keynes, UK.

[3]Laboratoire de Planétologie et Géodynamique de Nantes-UMR CNRS 6112, Nantes, France.

[4]Space Science and Technology Department, STFC Rutherford Appleton Laboratory, Oxfordshire, UK.

[5]Center for Advanced Spatial Technologies, University of Arkansas, Fayetteville, Arkansas, USA.

**This chapter has been published.**
**Sylvest, M.E., Conway, S.J., Patel, M.R., Dixon, J.C., Barnes, A., 2016. Mass wasting triggered by seasonal $CO_2$ sublimation under Martian atmospheric conditions: Laboratory experiments. *Geophysical Research Letters*, 43, 12,363-12,370. https://doi.org/10.1002/2016GL071022.**

## 2.1 Abstract

Sublimation is a recognized process by which planetary landscapes can be modified. However, interpretation of whether sublimation is involved in downslope movements on Mars and other bodies is restricted by a lack of empirical data to constrain this mechanism of sediment transport and its influence on landform morphology. Here we present the first set of laboratory experiments under martian atmospheric conditions which demonstrate that the sublimation of $CO_2$ ice from within the sediment body can trigger failure of unconsolidated, regolith slopes, and can measurably alter the landscape. Previous theoretical studies required $CO_2$ slab ice for movements, but we find that only frost is required. Hence, sediment transport by $CO_2$ sublimation could be more widely applicable (in space and time) on Mars than previously thought. This supports recent work suggesting $CO_2$ sublimation could be responsible for recent modification in martian gullies.

## 2.2 Introduction

Sublimation is a recognized planetary process [*Mangold*, 2011], primarily identified with pitting or uneven lowering of a surface. Sublimation has been implicated as one of several potential mechanisms controlling hillslope processes on Mars; notably recent erosion and deposition in kilometer-scale gullies (Figure 2.1) [*Dundas et al.*, 2015]. Gully-like features are also reported on Vesta [*Krohn et al.*, 2014; *Scully et al.*, 2015], and are seen on the Moon [*Bart*, 2007].

For recent changes in gullies on Mars and Vesta, alternate processes include formation by flowing water and/or brine [*Malin and Edgett*, 2000; *Scully et al.*, 2015]. These “wet” hypotheses are based on the plan view and 3D morphology of the features, which are consistent with

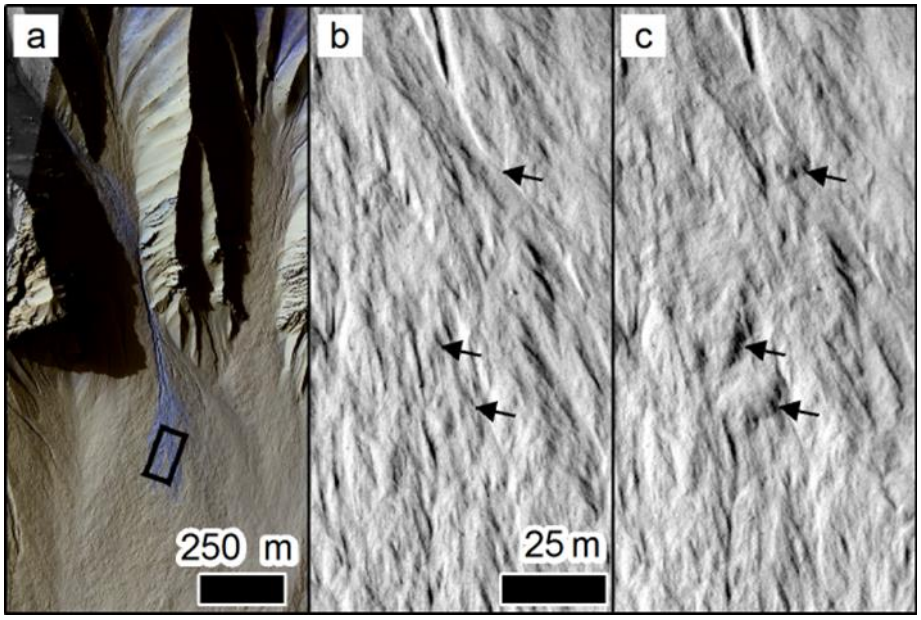


**Figure 2.1.** Features thought to be caused by sublimation on Mars. (a) High Resolution Imaging Science Experiment (HiRISE) image ESP_020661_1440of martian gullies in Gasa crater. Black box indicates location of b and c. (b and c) New gully deposits form in winter when $CO_2$ is present [*Dundas et al.*, 2012; *Vincendon*, 2015] (ESP_012024_1440 and ESP_020661_1440). Image credits: NASA/JPL-Caltech/Univ. of Arizona.

observations of terrestrial analogues, e.g. wet debris flow gullies [*Reiss et al.*, 2011], or seeping flows on Earth [*Kreslavsky and Head*, 2009]. However, there are no terrestrial analogues for the action of sublimation in a hillslope context, which hampers the assessment of whether observations are also consistent with formation by sublimation. The overarching motivation behind this study is therefore to provide experimental data in order to test the ability of sublimation to produce hillslope features and to start to constrain the observables required to identify its action. We focus our study on the seasonal (local spring) sublimation of $CO_2$ on Mars for two reasons. Firstly, Mars has a seasonal $CO_2$ condensation-sublimation cycle that is closely linked to many active surface features observed in orbital images [*Kieffer et al.*, 2006; *Gardin et al.*, 2010; *Hansen et al.*, 2011], suggesting a possible causal relationship. And secondly, because

ongoing observations and studies of martian hillslope features are more numerous and detailed than those for the other bodies cited above.

The only other experiments to date involving mass transport by $CO_2$ sublimation are field experiments which have explored the morphological effect of levitating blocks of $CO_2$ ice moving down slip faces of sand dunes [*Diniega et al.*, 2013]. These experiments were focused on reproducing some of the key features of the so-called "linear" gullies, which are only observed on the surface of large, dark sand dunes in the southern hemisphere of Mars.

Two numerical models have been used to assess the efficacy of downslope transport driven by $CO_2$ slab ice sublimation on Mars. Cedillo-Flores et al. [*Cedillo-Flores et al.*, 2011] simulated the fluidization of sediment deposited over a sublimating slab of $CO_2$ ice. Assuming 0.3-100 mm thick layers of sand (100 μm) and dust (3 μm), they calculated whether the sublimation rate of the underlying $CO_2$ would be sufficient to mobilize the sediment on a 25° bed, located at 75°N/S. They found sand was always mobilized, while only dust layers <100 mm thick could be mobilized. Pilorget and Forget [*Pilorget and Forget*, 2016] modelled the mobilization of dry sediment trapped between $CO_2$ slab ice and an overlying water ice-cemented permafrost. This model was optimized for the "linear" gullies on the Russell crater megadune at 55°S, exploring slope angles between 10 and 30°. They used a climate model to predict that movements generated this way should be possible anywhere polewards of 60°S and on pole-facing slopes polewards of 25°S.

Despite these previous studies being focused on slab ice, there is a lack of observational evidence in support of slab ice occurring equatorward of ~65° [*Kieffer et al.*, 2006]. Also, slab ice requires a long period of time below the condensation temperature in order to develop. $CO_2$ is

known to occur more widely (both spatially and temporally) as surface frost [*Vincendon*, 2015], and this form of $CO_2$ ice has been observed in regions with recent gully modifications. Therefore, in order to assess the ability of more ubiquitous surface frost to trigger downslope movements, we condensed $CO_2$ frost directly on the regolith. We performed four experimental runs, and one control run.

## 2.3 Approach

The three principal requirements of our approach were (1) condense $CO_2$ on/into a regolith slope, without introducing water or other ices; (2) sublimate the $CO_2$ at martian atmospheric temperature and pressure by means of radiant heating; and (3) record resulting regolith activity for visual and photogrammetric analysis. Use of close-range photogrammetric techniques allowed us to determine slope angles, as well as displacement volumes and rates. Simulation of the martian environment was achieved in the Mars Chamber at the Open University, Milton Keynes, UK (Figure 2.4) [*Conway et al.*, 2011a]. Full details of our approach are in the Supporting Information, and we provide a brief summary below.

The regolith was contained within a 30 cm long, cooled, copper test section (Figures S2 and S3). The scale of the test section was limited by the time required to cool the sediment body, and by the field of view of the video cameras used to record the experiments and produce the digital elevation models (DEM) through stereo photogrammetry. Along with atmospheric temperature and pressure, temperatures within the slope were logged at multiple depths along the centerline, near the mid-point and just below the slope crest (Figure 2.5). A shape movement detection algorithm was also applied to each movie pair, providing a heuristic measure of relative slope surface activity levels.

As a first test of the ability of $CO_2$ sublimation to trigger slope failure, the regolith was formed into a stable slope near the angle of repose (22°-33°); the most favorable condition for slope failure. This configuration was used to ensure that even the smallest disturbance resulted in a detectable motion, or failure. The regolith was then cooled to below the freezing point of $CO_2$ (-112 °C) in a dry nitrogen atmosphere (~350 mbar) to ensure the absence of water vapor. Gaseous $CO_2$ was introduced above the regolith, while continuing to cool, in order to condense $CO_2$ on and/or within the regolith. The pressure was then lowered in the chamber to the target pressure of ~5–6 mbar consistent with Mars [*Hess et al.*, 1980]. Finally, the surface was illuminated by a heat lamp for at least ~90 minutes, or until all the recorded temperatures were above -120 °C ($CO_2$ sublimation point at ~5 mbar). The near-surface temperature ranged from $-123$°C to 9°C over the course of the sublimation process. We calculate that the maximum heat flux at the bare regolith surface as ~350 W/m$^2$ (details in the Supporting Information), which is comparable with Viking lander insolation data [*Landis and Appelbaum*, 1990].

### 2.4 Results

All four of the experiments resulted in the downslope transport of material induced by $CO_2$ sublimation. No activity was observed in the control run. In this section, we first describe the nature and timing of the activity, and then present the results from the time series elevation models.

#### 2.4.1 Nature and Timing of Activity

Runs 1, 3 and 4 showed very similar behavior, while run 2 exhibited a number of notable differences. In all experiments, before sublimation began, a visible layer of frost covered the lower one-quarter to one-half of the slope, concentrating along the test section walls, and

particularly at the foot of the slope, where the sediment-depth is ~2 cm (Figures 2.2a and S4). The first detectable movements in each run were shifting grains of $CO_2$ frost, which had no effect on the underlying regolith surface. Mass wasting of regolith started within the first 15 minutes of each run, except for run 2, which became active ~40 min into the run (Figure 2.3a). These initial failures, up to several centimeters wide, started 4 – 10 cm downslope of the crest, and extended to the base of the slope, where they formed depositional lobes (Figures 2.2, 2.4 and Movie 2.1). In runs 1, 3 and 4, slope activity peaked within the first 25 minutes, while run 2 peaked after 60 minutes (Figure 2.3). For all runs, activity continued sporadically after the initial peak (Figure 2.3) and with continued slope failures, grew to the full slope width (Figure 2.2). For runs 1, 3 and 4, activity extended up to the slope crest (Figures 2.2 and 2.4). Slope failures were in the form of granular flows, which initiated below the surface of the slope, proximal to, but never underneath, visible, surface frost. Flows did not appear to disturb surface frost accumulations, generally following lateral contours, and either overran or stopped at the edge of downslope accumulations. Where deposits did cover visible surface frost, the new, overlying surface deposit became pitted by sublimation, occasionally so vigorously agitated as to resemble boiling (Movie 2.2).

Warming of the test section top edges during the second half of each run caused accumulations of $CO_2$ ice to fall onto the slope. None of these events resulted in significant sediment transport. Some later slope failures were characterized by an initial slip, followed by a slow slumping, or sliding of the material deposited by earlier movements in the lower half of the slope. These slumps occurred where visible frost was observed at the start of each run. This slumping behavior is particularly noticeable in accelerated video replay (Movie 2.3).

Run 2 differences included: i) at the start of the run surface frost was confined to within bottom-most 3 cm of the slope, ii) the initial failure occurred at ~40min into the run, with the earliest movement of this failure being some tumbling grains at the mid-point of the slope, and iii) the failures were confined to the lower half of the test section and never propagated to the crest of the slope (Figure 2.8). However, the granular flow nature of the run 2 slope failures was consistent with the other runs.

### 2.4.2 Evolution of Volumes and Slope-angles

As described in the Supporting Information, for each 10 min interval, we calculated the volume eroded and deposited by the flows, which implicitly includes the volume of the $CO_2$ sublimated during the experiment.

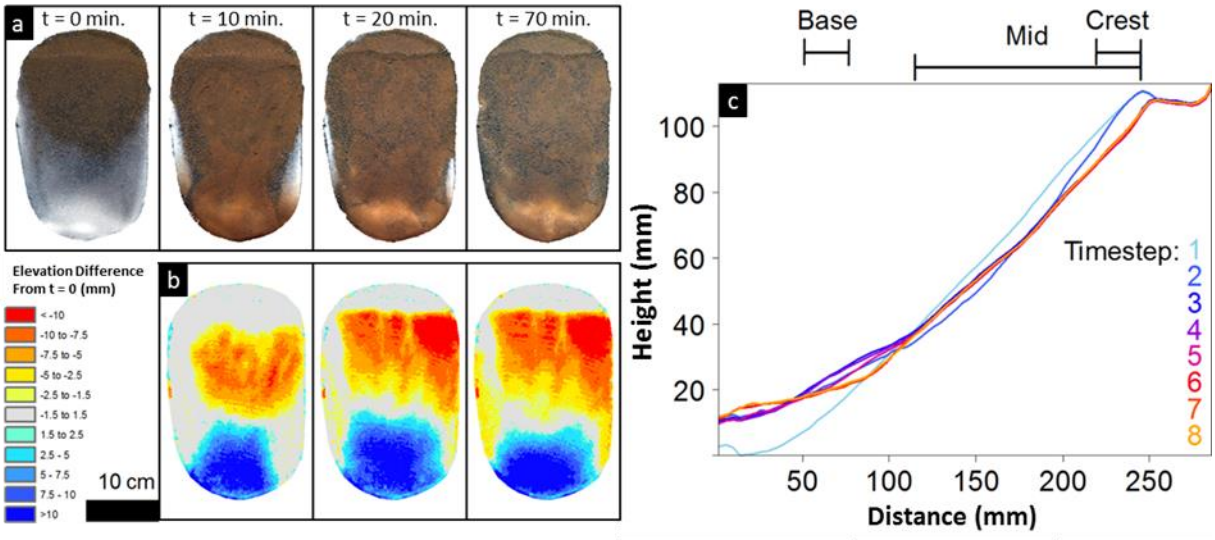


**Figure 2.2.** Evolution of the surface during experiment run 3. (a) Orthophotos showing visible appearance of the surface at t = 0, 10, 20 and 70 min elapsed sublimation. White coloration is $CO_2$ surface frost. (b) Topographic change from t = 0 to t = 10, 20 and 70 min, where red is erosion and blue is deposition. The scale for all images is the same, and the top of every image corresponds to the highest elevation of the test section. (c) Evolution of the topographic long profiles for each time step of run 3. The regions used to measure the slope-angles reported in Table 2.1 are indicated at the top.

Volume transport rates calculated from the DEMs (e.g. Figure 2.2b) were consistent with the timing of surface activity in Figure 2.3a. During the first 10 – 20 min of runs 1, 3 and 4, most erosion takes place in the middle of the slope, initiating 2 – 3 cm below the crest. As each run progresses, most of the upper slope erodes, causing the crest to retreat (Figure 2.2b and Movie 2.4). This phase of activity establishes the maximum areal extent of deposition and encompasses the peak erosion rate shown in Figure 2.3b. Later slope failures, although infrequent and sporadic, continued to transport regolith downslope; however, these were a minor contribution to the overall volume transported (Figures 2.2b and 2.3b). For run 2, activity started later, began mid-slope (concentrated at the edges), never extended up to the slope crest (Figure S6b) and

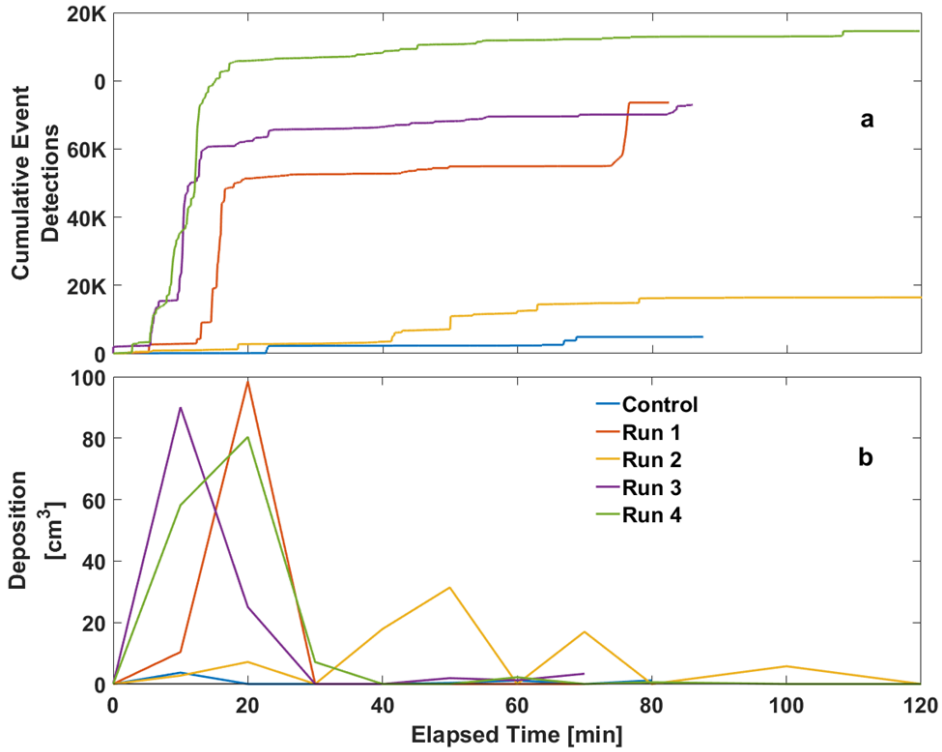


**Figure 2.3.** Sublimation induced "activity" and deposition rate over time for each experimental run. (a) Cumulative plot of "events" detected via motion detection against time. (b) Variation of deposition rate over time for each run, calculated by differencing elevation models at ~10 min time steps.

volumes of sediment were moved sporadically throughout (Figure 2.3). The recorded change in elevation due to erosion was 0.02 – 1.1 cm; and 0.02 – 1.3 cm of deposition for all runs.

The total erosion volume ranges between 122 and 173 $cm^3$ for runs 1, 3, 4; ~3.4% of the initial regolith volume, on average (Table 2.1). For run 2, the erosion volume is 69 $cm^3$; ~1.6% of the initial regolith volume.

**Table 2.1.** Summary of Experimental Results[a]

| | Control | Run 1 | Run 2 | Run 3 | Run 4 |
|---|---|---|---|---|---|
| Total erosion ($cm^3$) | 27.2 | 122.6 | 68.6 | 173.3 | 144.5 |
| Total deposition ($cm^3$) | 3.8 | 85.4 | 46.2 | 101.5 | 127.0 |
| Frost volume ($cm^3$) | n/a | 37.2 | 22.4 | 71.8 | 17.5 |
| Erosion per volume frost | n/a | 3.3 | 3.10 | 2.4 | 8.3 |
| Volume uncertainty | 2.2% | 3.0% | 1.6% | 3.6% | 3.5% |
| *Crest Slope Angles* | | | | | |
| Initial angle | 25.4° | 32.6° | 25.9° | 25.3° | 21.6° |
| Final angle | 25.2° | 27.8° | 26.4° | 31.6° | 31.1° |
| Angle change | -0.2° | -4.7° | 0.5° | 6.3° | 9.5° |
| *Mid-slope Angles* | | | | | |
| Initial angle | 27.8° | 28.3° | 27.2° | 29.7° | 25.7° |
| Final angle | 27.8° | 24.2° | 29.1° | 27.4° | 22.1° |
| Angle change | 0.0° | -4.1° | 1.9° | -2.3° | -3.55° |
| *Base Slope Angles* | | | | | |
| Initial angle | 29.7° | 18.3° | 26.2° | 22.7° | 23.2° |
| Final angle | 29.8° | 13.7° | 10.1° | 8.30° | 5.87° |
| Angle change | 0.1° | -4.6° | -16.1° | -14.4° | -17.3° |
| Angle uncertainty | 1.1% | 2.0% | 1.0% | 3.0% | 1.1% |
| Average initial slope temperature (°C) | -150.4 | -142.3 | -143.5 | -143.5 | -143.6 |
| Average Initial basal slope temperature (°C) | -168.0 | -161.8 | -171.2 | -167.5 | -167.1 |
| Sublimation duration (min) | 88 | 87 | 109 | 86 | 121 |

[a]Regolith volume for all runs was 4330 $cm^3$.

The deposition volume is between 85 and 127 $cm^3$ (~2.4% of the initial volume on average) for runs 1, 3 and 4, and ~1.1% for run 2. Erosion generally exceeded deposition, which we interpret as being due to the removal of the condensed $CO_2$ ice. As direct measurement of the $CO_2$ ice volume was infeasible, the difference between erosion and deposition volumes was used

to estimate a minimum solid $CO_2$ volume (Table 2.1). For all runs, sublimation of 1 $cm^3$ of $CO_2$ ice resulted in the erosion of 2.4 – 8.3 $cm^3$ of regolith (Table 2.1).

We measured an average reduction of slope along the centerline of ~4.1° for runs 1, 3 and 4 (Table 2.1); ~90% of that change occurring within the first 20 minutes of the run (Figure 2.2c). These failures initiated on slope angles between 22° and 32° (crest-angles in Table 2.1). Over the course of the experiment, slope-angles were retained at the crest of the profile but declined in both the mid-slope and base slope areas (Figures 2.2c and S6). For run 2, late activity was restricted to the mid-portion of the slope, and this failure initiated at an angle of 25.6° (Figure 2.8). For the later slumps in runs 1, 3 and 4, initiation at angles as low as 13° were observed (Figure 2.8a). These late slumps account for the majority of the volume difference seen in Figure 2.2, between t=20 min and t=70 min, in the bottom half of the test section.

## 2.5 Discussion

### 2.5.1 Physical Processes and Comparison to Previous Models

From our observations, we hypothesize that the porous nature of the regolith allows gas to infiltrate and freeze in the cold subsurface during the condensation procedure. Then, during the rapid production of gas during sublimation, the regolith pores restrict gas-escape, allowing pore pressure to increase to the point of slope failure.

This mechanism triggered failures at angles less than the static angle of repose ~38° [*Sullivan et al.*, 2011], but nearer the dynamic angle of repose ~29° [*Hofmann*, 2014], which suggests that sublimation provides the initial destabilization, and is followed by a non-fluidized granular flow. However, further work is required in order to properly substantiate this observation. Later failures, initiating in areas originally covered with frost, were triggered at

slope angles significantly below the dynamic angle of repose (down to 13°). We propose this is a result of the sublimation of an underlying layer of $CO_2$ ice both triggering and fluidizing the flow. This second mechanism is consistent with the model presented by Cedillo-Flores et al. [2011], in which a solid $CO_2$ slab overlain with up to 10 cm of aeolian-emplaced regolith (sand or dust), a highly unstable configuration, subsequently fluidizes.

In this first phase of experimentation, we did not intend to quantify the effects of the reduced gravity of Mars, relative to the Earth. However, theoretical considerations predict that the escaping gas velocity required to fluidize particles would be lower on Mars than on Earth e. This suggests the slope failures we observed would be more easily triggered and more erosive on Mars; thus, the results presented here may be conservative with respect to this sublimation process on Mars.

Failures were initiated in areas devoid of visible frost. This is significant, as the visible/spectral presence of $CO_2$ frost has been associated with present-day gully-activity on Mars [*Hugenholtz*, 2008; *Vincendon*, 2015], including the extension of "thin" deposits [*Malin et al.*, 2006; *McEwen et al.*, 2007], and particularly the development of new channels (Figure 2.1a-c) and new, meters-thick deposits [*Dundas et al.*, 2015]. We hypothesize that the cold temperature and high albedo of the surface frost accumulations in our experiments inhibit sublimation underneath the frost, and if thick enough may indurate the surface. Sediment movement triggered by this type of $CO_2$ sublimation on Mars, may therefore be most likely to initiate adjacent to visible frost, or after visible frost has disappeared from the surface. As a result of these observations we suggest future experiments should carefully examine the partitioning between surface and subsurface frost.

### 2.5.2 Implications for Interpreting Slope Processes on Mars

While the spatial scale of our experiments does not allow direct comparison with full-scale surface features, like gullies, our results do establish the potential for $CO_2$ sublimation to trigger mass wasting of dry, unconsolidated material on sloping surfaces under martian environmental conditions. This supports the assertions of previous research that $CO_2$ sublimation could be responsible for recent movements detected in gullies, and seasonal sediment flows observed on martian dunes [*Diniega et al.*, 2010; *Reiss et al.*, 2010; *Dundas et al.*, 2012; *Pasquon et al.*, 2016]. As noted earlier, the particular mechanism explored here only applies to movements which occur in the absence of slab ice. The movement of 1-2 m scale-boulders down the gully channels in the presence of visible $CO_2$ frost observed by Dundas et al. [2015] is also unlikely to be caused by the mechanism discussed here but warrants further experimental investigation. The latitudinal distribution of recurring slope lineae (RSL) [*McEwen et al.*, 2014] is not consistent with the seasonal extent of $CO_2$ frost [*Vincendon*, 2015; *Piqueux et al.*, 2016]; hence this mechanism could not universally be applied to these features. The distribution of slope streaks [*Sullivan et al.*, 2001; *Schorghofer et al.*, 2002] has recently been found to correlate with the night-time occurrence of $CO_2$ frost in areas with high dust and low thermal inertia, at mid- to equatorial latitudes [*Piqueux et al.*, 2016]. Piqueux et al. [2016] estimate that up to 350 μm of frost could be deposited onto the surface at night and that deposition of frost into the subsurface would require subsurface cold traps. While our experiments were focused on seasonal frost, our observations support the need for subsurface frost deposits to initiate sediment movements.

Our observations suggest that this is a slope-limited process, similar to other gravity driven mass wasting processes, such as wet debris flows and landslides [*Lague and Davy*, 2003;

*DiBiase et al.*, 2012]. We emphasize that we do not expect angular limits found in our experiments to apply on Mars due to the difference in gravitational acceleration; however, this observation shows that the $CO_2$ sublimation process is feasible beyond the domain of gravity triggered granular flows. Brusnikin et al. [*Brusnikin et al.*, 2016] reported a slope limit of 18-20°, below which they found very few initiations of granular flows, and suggested these flows are limited by the dynamic angle of friction. This is consistent with our finding that granular flows not fluidized by sublimating ice initiate at angles >20°, in our experiments. Because slope angle is often a key factor used to distinguish between different geomorphic processes [*Lanza et al.*, 2010; *Conway et al.*, 2011b], this is an important area which warrants further investigation to further constrain the slope-limits of this type of sublimation-triggered slope failure.

Our experimental results show that $CO_2$ sublimation can trigger movement without the ice being in the form of a slab. Thus, $CO_2$ sublimation could be a more widely active agent of surface alteration than previously assumed, particularly in light of the discovery of an equatorial, diurnal $CO_2$ cycle [*Piqueux et al.*, 2016].

Gully modifications have been reported at mid-latitudes on Mars, where seasonal surface frost can be on the order of millimeters to centimeters thick [*Vincendon*, 2015], and volumes of displaced sediment have been estimated at tens to hundreds of cubic meters [*Dundas et al.*, 2015]. Based on our calculated rate of sediment displacement per $CO_2$ ice volume (Table 2.1 and Supplemental Information), the aforementioned thickness and displacement volume ranges require areas of frost-laden sediment hundreds to tens of thousands of square meters. This is consistent with the observation that source areas commonly display "minor morphological effects" [*Dundas et al.*, 2015].

### 2.5.3 Wider Implications

Understanding how $CO_2$ interacts with geological materials under martian conditions is fundamental to our interpretation of current geomorphological activity, atmospheric evolution, and the history of water on Mars. Forms such as gullies, for example, are found over much of the surface of Mars [*Harrison et al.*, 2015], and were initially interpreted as evidence for the action of substantial quantities of liquid water [*Malin and Edgett*, 2000]. The possibility of $CO_2$-induced gully modification means water may not always be necessary to form such features [*Dundas et al.*, 2015]. A deeper understanding of the mechanism of hillslope modification by sublimation is required before we can interpret present-day changes; much less attempt to interpret landscape evolution over the Amazonian period.

In a wider context, sublimation affects the surfaces of other terrestrial planets. Hence, understanding sublimation as a sediment transport mechanism has implications beyond Mars, and will guide interpretation of data coming from a wide-range of current and future planetary space missions.

## 2.6 Conclusions

We have demonstrated for the first time, in the laboratory, that sublimation of condensed $CO_2$ frost, under martian atmospheric conditions, can trigger mass wasting of unconsolidated regolith. These results provide one possible explanation for recent modifications observed in gullies, without the need for liquid water. The observed slope failures are dry granular flows, apparently triggered by the sublimation of $CO_2$ ice condensed in the regolith pore space. Fluidization of regolith over subsurface frost may allow for sediment transport at angles below the dynamic angle of repose. The $CO_2$ frost sublimation trigger mechanism may have broader

spatial and temporal applicability on Mars than $CO_2$ slab mechanisms. It may also help explain the behavior and distribution of enigmatic martian slope streaks, as diurnal $CO_2$ frost has recently been found to correlate with their distribution. Although not directly simulated in these experiments, our results suggest sublimating diurnal $CO_2$ frost may help explain the behavior and distribution of enigmatic martian slope streaks, recently found to correlate with diurnal $CO_2$ frost locations.

These experiments represent an important first step in understanding the role of sublimation as a landscape-forming process in the solar system and underline the urgent need for further laboratory work to constrain the limits (slope angle, grainsize, etc.) of $CO_2$-driven processes to support meaningful comparisons between observed morphologies and formation processes.

## 2.7 Acknowledgements

Funding was provided for M.E.S. by the Open University, the Sturgis International foundation and the University of Arkansas Graduate School. We thank D. Rothery and R. Thomas for discussions related to the broader implications of the work; T. Ringrose for his collaboration and guidance in the laboratory. S.J.C. acknowledges funding from the Leverhulme Trust in support of this work (grant RPG-397) and from the French Space Agency CNES. M.R.P. acknowledges support from the UK Space Agency (grant ST/I003061/1) and the EU Horizon 2020 Program (UPWARDS-633127). Data supporting the conclusions can be found within the figures and table presented in the main text and within the online supporting information.

## 2.8 References


Allen, C.C., Morris, R.V., Karen, M.J., Golden, D.C., Lindstrom, M.M., Lockwood, J.P. (1998), Martian Regolith Simulant JSC Mars-1, in *Lunar and planetary science conference XXVIII*, p. 1690.

Bart, G. D. (2007), Comparison of small lunar landslides and martian gullies, *Icarus*, 187(2), pp.417–421. https://doi.org/10.1016/j.icarus.2006.11.004.

Brusnikin, E. S., M. A. Kreslavsky, A. E. Zubarev, V. D. Patratiy, S. S. Krasilnikov, J. W. Head, and I. P. Karachevtseva (2016), Topographic measurements of slope streaks on Mars, *Icarus*, 278, pp.52–61. https://doi.org/10.1016/j.icarus.2016.06.005.

Cedillo-Flores, Y., Treiman, A.H., Lasue, J., Clifford, S.M. (2011), $CO_2$ gas fluidization in the initiation and formation of Martian polar gullies, *Geophysical Research Letters*, 38(21). https://doi.org/10.1029/2011GL049403.

Conway, S.J., Lamb, M.P., Balme, M.R., Towner, M.C., Murray, J.B., 2011a. Enhanced runout and erosion by overland flow at low pressure and sub-freezing conditions: Experiments and application to Mars. *Icarus,* 211, pp.443–457. https://doi.org/10.1016/j.icarus.2010.08.026.

Conway, S.J., Balme, M.R., Murray, J.B., Towner, M.C., Okubo, C.H. & Grindrod, P.M. 2011b. The indication of Martian gully formation processes by slope-area analysis. *In*: Balme, M.R., Bargery, A.S., Gallagher, C.J. & Gupta, S. (eds) *Martian Geomorphology*. Geological Society, London, Special Publications, 356, pp.5–20. https://doi.org/10.1144/SP356.10.

DiBiase, R. A., A. M. Heimsath, and K. X. Whipple (2012), Hillslope response to tectonic forcing in threshold landscapes, *Earth Surface Processes and Landforms*, 37(8), pp. 855–865. https://doi.org/10.1002/esp.3205.

Diniega, S., Byrne, S., Bridges, N.T., Dundas, C.M., McEwen, A.S., 2010 Seasonality of present-day Martian dune-gully activity. *Geology,* 38(11), pp.1047–1050. https://doi.org/10.1130/G31287.1.

Diniega, S., Hansen, C.J., McElwaine, J.N., Hugenholtz, C.H., Dundas, C.M., McEwen, A. S., Bourke, M.C., 2013. A new dry hypothesis for the formation of martian linear gullies. *Icarus,* 225(1), pp.526–537. https://doi.org/10.1016/j.icarus.2013.04.006.

Dundas, C.M., Diniega, S., Hansen, C.J., Byrne, S., McEwen, A.S., 2012. Seasonal activity and morphological changes in martian gullies. *Icarus,* 220(1), pp.124–143. https://doi.org/10.1016/j.icarus.2012.04.005.

Dundas, C.M., Diniega, S., McEwen, A.S., 2015. Long-term monitoring of martian gully formation and evolution with MRO/HiRISE. *Icarus,* 251, pp.244–263. https://doi.org/10.1016/j.icarus.2014.05.013.

Harrison, T.N., Osinski, G.R., Tornabene, L.L., Jones, E., 2015. Global Documentation of Gullies With the Mars Reconnaissance Orbiter Context Camera and Implications for Their

Formation. *Icarus*, 252, pp.236-254. https://doi.org/http://dx.doi.org/10.1016/j.icarus.2015.01.022.

Hess, S.L., Ryan, J.A., Tillman, J.E., Henry, R.M. & Leovy, C.B. 1980. The annual cycle of pressure on Mars measured by Viking Landers 1 and 2. *Geophysical Research Letters*, 7(3), pp.197–200. https://doi.org/10.1029/GL007i003p00197.

Hofmann, M. (2014), Dynamics of Granular Material on Small Bodies, Ph.D. Dissertation, Technischen Universität Braunschweig. https://www.mps.mpg.de/phd/theses/dynamics-of-granular-material-on-small-bodies.

Hugenholtz, C. H. (2008), Frosted granular flow: A new hypothesis for mass wasting in martian gullies, *Icarus*, 197(1), pp.65–72. https://doi.org/10.1016/j.icarus.2008.04.010.

Kieffer, H.H., Christensen, P.R., Titus, T.N., 2006. $CO_2$ jets formed by sublimation beneath translucent slab ice in Mars' seasonal south polar ice cap. *Nature*, 442(7104), pp.793–796. https://doi.org/10.1038/nature04945.

Kreslavsky, M.A., Head, J.W., 2009. Slope streaks on Mars: A new "wet" mechanism. *Icarus*, 201(2), pp.517–527. https://doi.org/10.1016/j.icarus.2009.01.026.

Krohn, K. Jaumann, R., Hoogenboom, T., Wagner, R., Buczkowski, D.L., Garry, B., Williams, D.A., Yingst, R.A., Scully, J., De Sanctis, M.C., Kneissl, T., Schmedemann, N., Kersten, E., Stephan, K., Matz, K., Pieters, C.M., Reusker, F., Roatsch, T., Schenk, P., Russell, C.T., Raymond, C.A., 2014. Mass movement on Vesta at steep scarps and crater rims, *Icarus*, 244, 120–132. https://doi.org/10.1016/j.icarus.2014.03.013.

Lague, D., Davy, P. 2003. Constraints on the long-term colluvial erosion law by analyzing slope-area relationships at various uplift rates in the Siwaliks Hills (Nepal), *Journal of Geophysical Research: Solid Earth*, 108(2). https://doi.org/10.1029/2002JB001893.

Landis, G.A., Appelbaum, J., 1990. Design considerations for Mars photovoltaic power systems, *Photovoltaic Specialists Conference, 1990. Conference Record of the Twenty First IEEE*, pp. 1263–1270.

Lanza, N.L., Meyer, G.A., Okubo, C.H., Newsom, H.E.,Wiens, R.C., 2010. Evidence for debris flow gully formation initiated by shallow subsurface water on Mars, *Icarus*, 205(1), pp.103–112. https://doi.org/10.1016/j.icarus.2009.04.014.

Malin, M.C., Edgett, K.S., 2000. Evidence for Recent Groundwater Seepage and Surface Runoff on Mars. *Science*, 288(5475), pp.2330–2335. https://doi.org/10.1126/science.288.5475.2330.

Malin, M.C., Edgett, K.S., Posiolova, L. V, McColley, S.M., Dobrea, E.Z.N., 2006. Present-day impact cratering rate and contemporary gully activity on Mars *Science*, 314(5805), pp.1573–1577. https://doi.org/10.1126/science.1135156

Mangold, N., 2011. Ice sublimation as a geomorphic process: A planetary perspective, *Geomorphology*, 126(1), pp.1–17. https://doi.org/10.1016/j.geomorph.2010.11.009.

McEwen, A.S., Hansen, C.J., Delamere, W.A., Eliason, E.M., Herkenhoff, K.E., 2007. A closer look at water-related geologic activity on Mars, *Science*, 317(5845), pp.1706–1709. https://doi.org/10.1126/science.1143987.

McEwen, A.S., Dundas, C.M., Mattson, S.S., Toigo, A.D., Ojha, L., Wray, J.J., Chojnacki, M., Byrne, S., Murchie, S.L., Thomas, N., 2014. Recurring slope lineae in equatorial regions of Mars, *Nature Geoscience*, 7(1), pp.53–58. https://doi.org/10.1038/ngeo2014.

Pasquon, K., Gargani, J., Massé, M., Conway, S.J., 2016. Present-day formation and seasonal evolution of linear dune gullies on Mars. *Icarus*, 274, pp.195–210. https://doi.org/10.1016/j.icarus.2016.03.024.

Pilorget, C., Forget, F., 2016. Formation of gullies on Mars by debris flows triggered by $CO_2$ sublimation. *Nature Geosciences*, 9, 65–69. https://doi.org/10.1038/ngeo2619.

Piqueux, S., Kleinböhl, A., Hayne, P.O., Heavens, N.G., Kass, D.M., McCleese, D.J. Schofield, J.T., Shirley, J.H. 2016. Discovery of a widespread low-latitude diurnal $CO_2$ frost cycle on Mars: Low-Latitude $CO_2$ Frost on Mars, *Journal of Geophysical Research:Planets*, 121(7), pp.1174-1189. https://doi.org/10.1002/2016JE005034.

Reiss, D., Erkeling, G., Bauch, K.E. & Hiesinger, H. 2010. Evidence for present day gully activity on the Russell crater dune field, Mars. *Geophysical Research Letters*, 37(6). https://doi.org/10.1029/2009GL042192.

Reiss, D. Hauber, E., Hiesinger, H., Jaumann, R., Trauthan, F. Preusker, F., Zanetti, M., 2011. Terrestrial gullies and debris-flow tracks on Svalbard as planetary analogs for Mars, *Geological Society of America*, 483, pp.165–175. https://doi.org/10.1130/2011.2483(11).

Schorghofer, N., Aharonson, O., Khatiwala, S., 2002. Slope streaks on Mars: Correlations with surface properties and the potential role of water, *Geophysical Research Letters*, 29(23), pp.41-1-41-4. https://doi.org/10.1029/2002GL015889.

Scully, J.E.C., Russell, T., Yin, A., Jaumann, R., Carey, E., Castillo-Rogez, J., McSween, H.Y., Raymond, C.A., Reddy, V., Le Corre, L., 2015. Geomorphological evidence for transient water flow on Vesta, *Earth and Planetary Science Letters*, 411, pp.151–163. https://doi.org/10.1016/j.epsl.2014.12.004.

Sullivan, R., Thomas, P., Veverka, J., Malin, M., Edgett, K.S., 2001. Mass movement slope streaks imaged by the Mars Orbiter Camera, *Journal of Geophysical Research: Planets*, 106(E10), pp.23607–23633.

Sullivan, R., Anderson, R., Biesiadecki, J., Bond, T., Stewart, H., 2011. Cohesions, friction angles, and other physical properties of Martian regolith from Mars Exploration Rover wheel trenches and wheel scuffs, *Journal of Geophyssical Ressearch: Planets*, 116(E2). https://doi.org/10.1029/2010JE003625.

Vincendon, M., 2015. Identification of Mars gully activity types associated with ice composition. *Journal of Geophysical Research: Planets*, 120(11), pp.1859–1879.

https://doi.org/10.1002/2015JE004909.

## 2.9 Appendix A: Supporting Information

### A1. Methods

The centerpiece of the experimental apparatus was the 1 m diameter, 2 m long Mars Chamber, housed at The Open University, Milton Keynes, UK (Figures S5). The experimental procedure consisted of five steps: (1) preparation of the regolith slope model, (2) purging and replacing the chamber atmosphere, (3) cooling the regolith, (4) condensing the $CO_2$ as frost, and (5) insolating the regolith while recording any surface modification.

#### A1.1. Step 1 - Slope Preparation

For each simulation, we raked JSC Mars-1 regolith simulant into a slope at or near the angle of repose (~30°). A widely used standard regolith simulant, JSC Mars-1 is a well characterized volcanic tephra, with a broad particle size distribution between 13 μm < 1 mm [*Allen et al.*, 1998]. We first stirred the regolith to homogenize the grain distribution and break up any aggregation. Next, we raked the regolith up the slope, to produce a uniform, meta-stable slope, keeping the position of the crest, the maximum depth (~12 cm) and minimum depth (~2 cm) consistent for each run (Figure 2.5b). Initial slopes for each run are listed in Table 2.1.

The test section, containing the model slope, consisted of a rectangular box, made of a single, continuous coil of copper tubing, approximately 30 cm long, 20 cm wide and 12 cm deep (inside dimensions). A copper sheet, ~1 mm thick, was braised to the bottom of the coiled sides (Figure 2.5b). The test section was also fitted with a copper lid (~1 mm sheet) and a mechanical opening mechanism (Figure 2.6).

Thermocouples were arranged to measure the temperature profile through the depth of the slope in two locations along the centerline (Figure 2.5b). One array of 4 thermocouples was positioned 4 cm from the rear wall of the test section, in the thickest section of the slope. The second array, with 3 thermocouples, was positioned approximately mid-slope, 14 cm from the rear wall of the test section. The thermocouple wires were routed along the bottom and sides of the section to avoid mechanically influencing slope stability. Temperatures were monitored and recorded throughout the remaining four steps of each experiment with a Pico Technologies PicoLog system. Chamber pressure was monitored with a Pirani gauge and recorded manually.

### A1.2. Step 2 - Atmosphere Preparation

After sealing the model slope within the Mars Chamber, vacuum pumps were used to reduce the chamber pressure to approximately 20 mbar. During this procedure, $CO_2$ was allowed to flow through the $CO_2$ delivery system to displace any trapped air and moisture, and then the system closed, while still pressurized with CP grade $CO_2$. After closing the test section lid to prevent disruption of the prepared slope, the chamber was backfilled with Zero grade $N_2$ to a pressure of 350 mbar. This cycle was then repeated, leaving the chamber pressure at 350 mbar.

### A1.3. Step 3 - Regolith Cooling

Having established a dry atmosphere (non-condensing for the full range of operating temperature and pressure of the experiment), liquid $N_2$ was piped through the test section coil (Figure 2.5a) in order to cool the regolith. The target maximum near-surface temperature was empirically determined to be cold enough to prevent the surface from warming above frost point for $CO_2$ when introducing warm $CO_2$ gas above the slope. The cooling process took from 6.5 to 10.5 hours to reach a target near-surface temperature of -112 °C.

### A1.4. Step 4 - Condensing $CO_2$ Frost

With the model slope at or below the target surface temperature, precooled $CO_2$ gas was introduced through the test section lid assembly. In order to prevent disturbing the regolith, the gas flow was controlled, with a two-stage pressure regulator and needle-valve, then fed through a diffuser affixed to the inside of the test section lid (Figures S3a and S4).

During the cooling process, the chamber pressure typically reduced to ~160 mbar. As the focus of this study is on the sublimation process, rather than the condensation of $CO_2$ frost, the chamber pressure was not reduced until the end of the condensation step, thus allowing frost to condense more readily than under martian conditions. During the last 20 minutes of condensation, the vacuum pumps were engaged to reduce the chamber pressure to the 5 – 7 mbar target range before starting the sublimation step.

### A1.5. Step 5 - Sublimation & Data Collection

In the final step of the experimental procedure, a 500 W halogen lamp was used to irradiate the slope surface, promoting sublimation of the $CO_2$ frost, while a pair of high definition video cameras stereographically recorded the slope surface (Figure 2.5a). The recorded near-surface temperature, measured along the slope centerline, ~4 cm from the back edge of the test section (Figure 2.5b), ranged from -122 °C to 30 °C, over the course of the sublimation process.

## A2. Photogrammetric methods

Two matched Sony HDR-CX330 camcorders were affixed to a purpose-built mount with a stereo baseline of ~9 cm and a height above surface of ~65 cm (Figures S3a and S4). Videos were recorded in AVCHD Progressive 1920 × 1080 format, at 30 fps, interlaced. An array of

photo-identifiable coded targets with known coordinates was used to scale, position, and orient the photogrammetric model within a local reference frame (Figure 2.6). The position of each coded target was photogrammetrically surveyed using a calibrated Canon 5D MkII DSLR camera with a 50 mm fixed lens and EOS Systems PhotoModeler Scanner v 2014 software. This survey was used to define the three-dimensional reference frame relative to the plane upon which the targets were affixed, and to export the precise (overall RMS of 0.2 pixels, overall point precision of 0.46 mm) XYZ coordinates of each coded target.

Each pair of movies was synchronized, and pairs of frame captures taken at 10 minute intervals, using Sony Vegas Pro 13.0 video production software. The captured image pairs and coded target coordinates were used to photogrammetrically derive fully referenced digital elevation models (DEMs) in Agisoft PhotoScan Pro 1.1.6. The maximum possible synchronization error is half of one frame, or ~17 ms.

To establish uniform camera orientation parameters for each image pair within an experimental run, we used images from all of the captured time steps, supplemented with images recorded from various positions around the box before the start of cooling, to provide a much larger, set of virtual cameras than the two actually used. After masking-out the regolith slope and measuring each coded target, this collection of images was used in the PhotoScan "Align Photos" step to compute the camera location and orientation for each image. After this group alignment procedure, a sequence of DEMs was produced for each pair of images (one pair for each time step), while masking the surrounding box. Additional tie points were iteratively added to fill sparse regions of the dense point cloud, resulting in a continuous surface model. Finally, we exported DEMs and orthophotos with 1.0 mm grid sizes. Random noise in the DEMs,

resulting from slight mismatches between image pairs, was estimated at ~1.5 mm vertical magnitude by taking the maximum absolute residual of a polynomial curve fitted to the long profile through the centerline of the initial, undisturbed slope. Planar placement of the photogrammetric markers, combined with instability of the camera mount, resulted in horizontal errors on the order of 1.0 mm. Consequently, the volumes and slopes calculated within each experimental run are reliable for comparison, but cross comparisons between runs and extraction of absolute slope values are less reliable.

### A3. Motion detection

We estimated the surface activity for each run using the VideoLAN VLC Media Player motion detection filter. After synchronizing the two video recordings, each recording was masked, to prevent detection of extraneous movements other than the regolith, and then combined into a single, composite video. The VLC log output generated during playback provided a count of all detected shape movements from both channels during playback of the composite video. While this procedure does not yield an absolute number of detected events, it does provide a consistent means for the comparison of the level and timing of activity for the regolith surface from run to run.

### A4. Volume and slope analyses

The DEMs were used to calculate erosion, deposition and slope angles for each time step and for the whole experiment. In order to calculate erosion and deposition volumes, the DEM for a given time step was differenced with the DEM from the previous time step (Figure 2.2). Errors in volume were calculated by considering the propagation of errors from the RMS error reported by PhotoScan, which we used as representative of the uncertainty of the scaling and position of

the DEM. This was considered to dominate over other errors, such as measurement of the control points and test section. We used the RMS values reported by PhotoScan in the x, y and z dimensions as representative of the uncertainty ($\sigma_x$, $\sigma_y$, $\sigma_z$ respectively) over the scale of the test-section (width = 30.0 cm, length = 20.0 cm, and depth = 12.0 cm); therefore the error for each time step was considered to be the same, giving $((\sigma_x/x)^2 + (\sigma_y/y)^2 + (\sigma_z/z)^2)^{0.5}$, where z = mean slope depth for each run (Table 2.2). Volume uncertainties were from 1.6% to 3.6% (Table 2.1). Slope profiles were generated by extracting all elevation data, within a 4 cm swath along the centerline, and averaging every 4 mm. To calculate the crest, mid, and bottom slopes of the profile, a linear least squares fit was performed on the following intervals: (a) crest, from the crest to 25 mm below crest, (b) mid, from the crest to 40% of the profile length, and (c) bottom, 50–70 mm along the profile. These intervals are marked on Figure 2.2c. The slopes reported in Figure 2.8 are those of linear-fits performed on the profile data over a moving window of five points. The dominant source of volume error was considered to be the uncertainty of scaling and position of the DEM. We used propagation of errors on the PhotoScan RMS values ($\sigma_x$ and $\sigma_z$) to estimate the resulting slope uncertainties, giving $((\sigma_x/x)^2 + (\sigma_z/z)^2)^{0.5}$, where x = the minimum slope baseline (20 mm), and z = mean slope depth for each run (Table 2.1). Errors on slopes are ~1.0–3.0% (Table 2.1).

## A5. Surface heat transfer analysis

The heat transferred to the bare regolith surface was estimated as the sum of the radiative contributions and a conductive component from the $CO_2$ gas above the surface:

$$q_{tot} = q_{rl} + q_{rc} + q_{cg} \quad (1)$$

where $q_{rl}$ radiant heat is supplied by the 500 W halogen lamp, $q_{rc}$ is the radiant heat from the chamber wall, and $q_{cg}$ is the heat conducted from the $CO_2$ gas above the surface. The analysis was based on conditions at the onset of the sublimation stage of the experiment, as this represents the highest temperature gradients; thus, ensuring that heating was maintained at or below martian conditions. Given the rarefied atmosphere and lack of disturbance inside the chamber, forced convection was assumed negligible; and given that the regolith surface was ~140°C colder than the chamber atmosphere, buoyancy effects were also ignored.

The average value of $q_{rl}$, ~358 ppf, was based on measurements with an Apogee Instruments Quantum Meter QMSS photosynthetic photon flux meter. Using a luminous efficacy of 19.8 lm/W for a tungsten halogen lamp, $q_{rl} = 88.5$ W/m$^2$.

Treating the chamber wall as a black body and the regolith surface as a gray body; neglecting atmospheric absorption and re-radiation; and assuming a shape factor of one, we calculate the radiation from chamber wall as:

$$q_{rc} = \sigma(1-\alpha)(T_c^4 - T_s^4) \qquad (2)$$

where $T_c$ is the temperature of the chamber walls, $T_s$ is the regolith surface temperature, $\sigma$ is the Stefan-Boltzmann constant, and $\alpha$ is the surface albedo. The albedo for JSC Mars-1 regolith simulant was taken as 0.526 [*Pommerol et al.*, 2013]. The chamber wall temperature was estimated to be approximately equal to the laboratory room temperature, typically ~20°C, due to the great mass of the chamber. The regolith surface temperature was estimated at -120°C based on thermocouple data. The radiant component is then 183.35 W/m$^2$.

Heat conduction from the $CO_2$ gas above the surface is given by:

$$q_{cg} = \frac{k(T_a - T_s)}{l} \quad (3)$$

is 75.2 W/m$^2$; where $k$ is the thermal conductivity of $CO_2$ gas at the average temperature of the thermal boundary layer, $4.48 \times 10^{-3}$ W/m·K, and $l$ is the thickness of the thermal boundary layer, ~8.35 mm, based on thermocouple data at the regolith surface (-120°C), 5 mm above the surface (-116°C), and at the chamber wall (20°C). $T_a$ is the ambient temperature of the chamber atmosphere, and $T_s$ the regolith surface temperature. Summing the contributions as in equation (1), the total estimated heat flux at the regolith surface, $q_{tot}$, is ~$347 \pm 30$ W/m$^2$.

## A6. References


Allen, C.C., Morris, R.V., Karen, M.J., Golden, D.C., Lindstrom, M.M., Lockwood, J.P. (1998), Martian Regolith Simulant JSC Mars-1, in *Lunar and planetary science conference XXVIII*, p. 1690.

Morgan, G.A., Head, J.W., Forget, F., Madeleine, J.B., Spiga, A. (2010), Gully formation on Mars: Two recent phases of formation suggested by links between morphology, slope orientation and insolation history, *Icarus*, 208(2), pp.658–666. https://doi.org/10.1016/j.icarus.2010.02.019.

Pommerol, A., Thomas, N., Jost, B., Beck, P., Okubo, C., McEwen, A. (2013), Photometric properties of Mars soils analogs, *Journal of Geophysical Research: Planets*, 118(10), pp.2045–2072. https://doi.org/10.1002/jgre.20158.


**Figure 2.4.** Mars Chamber (center), vacuum pump (bottom), liquid nitrogen supply (left), $CO_2$ gas cooler (front left of center).

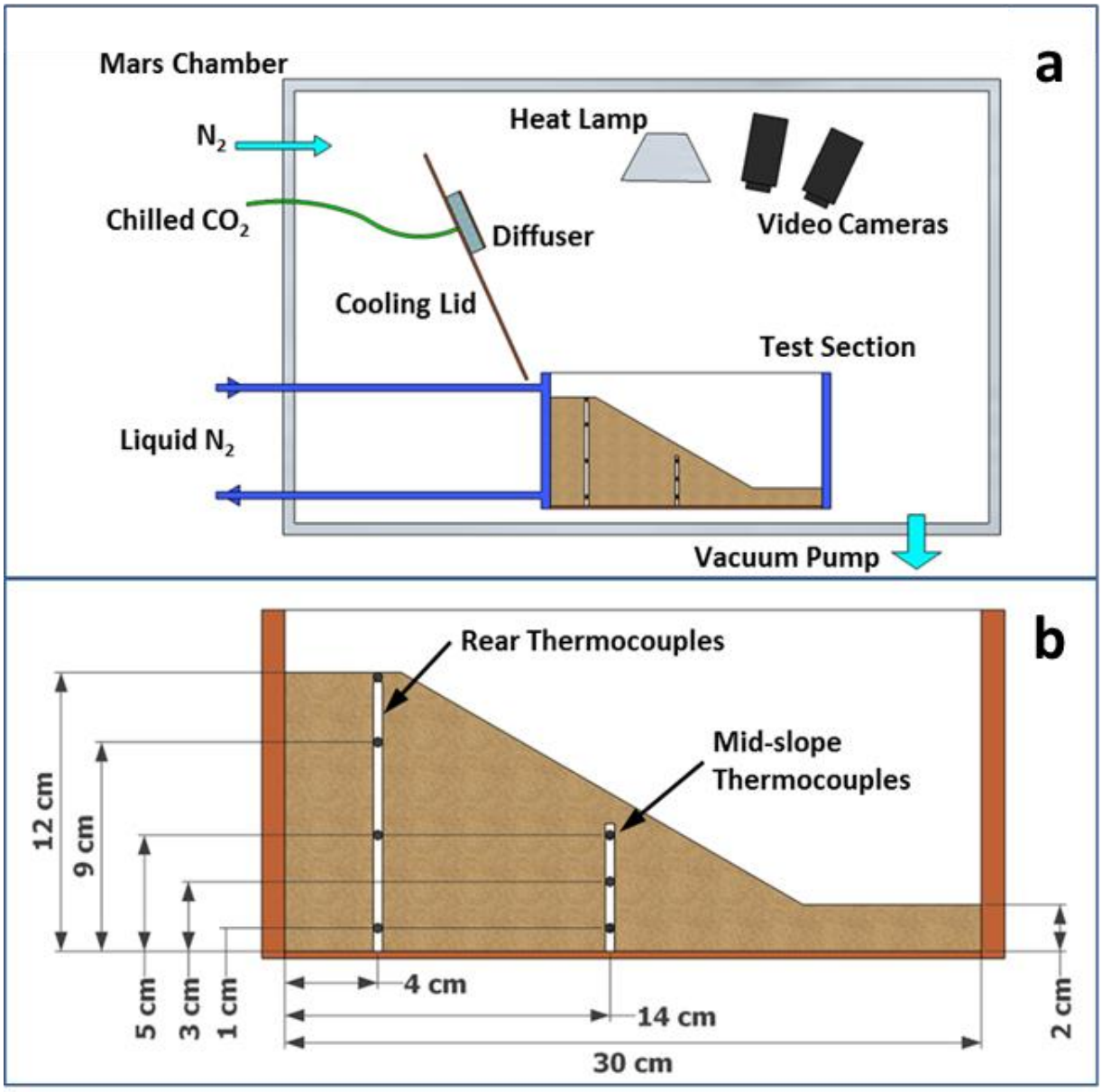


**Figure 2.5.** Schematic diagrams of test section layout and dimensions. (a) Schematic of the interior of the mars chamber, with relative positions of test section, pivoting cooling lid, heat lamp and cameras. (b) Schematic of test section and slope showing position of thermocouples along centreline.

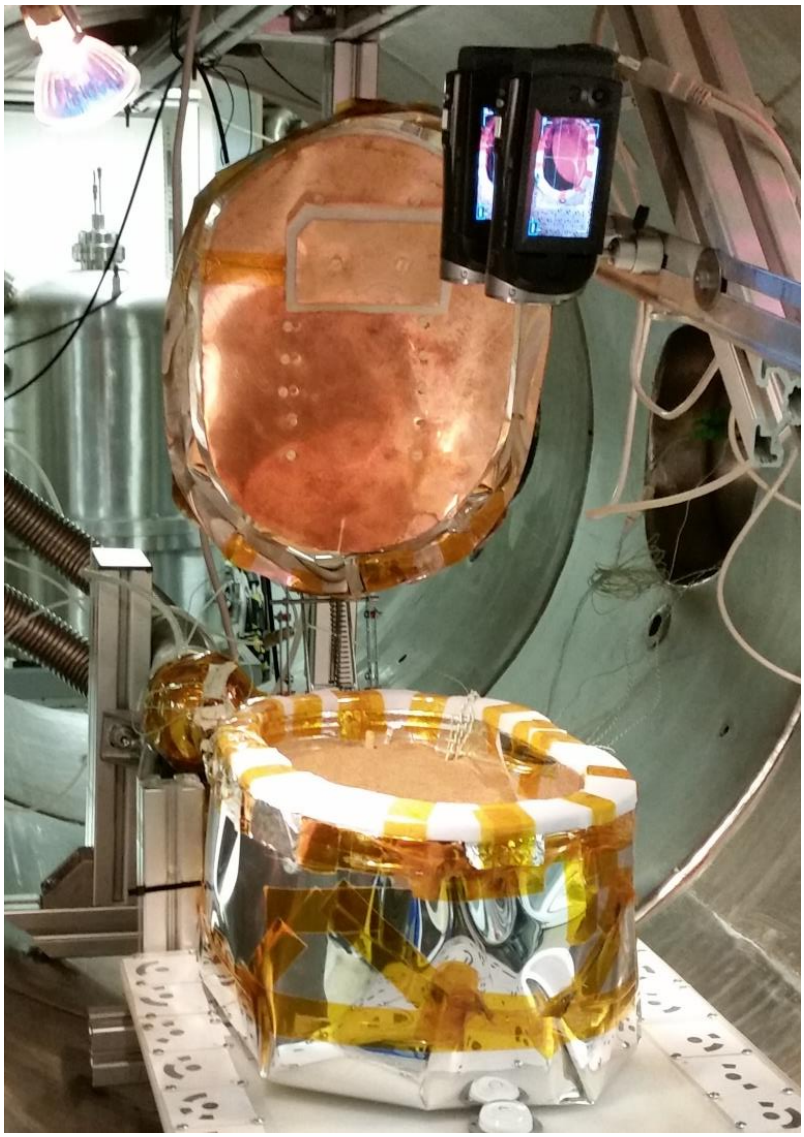

**Figure 2.6.** Configuration of the test section, within the Mars Chamber. Towards the front of the image, the insulated copper container with the regolith in place. The liquid $N_2$ lines enter at rear. Hinged at the rear of the test section is copper cooling cover with $CO_2$ inlet diffuser.


**Figure 2.7.** Orthophoto of the regolith surface at start of sublimation for Run 1. Slope crest is at the top of the image. The width of the test section is 30 cm.

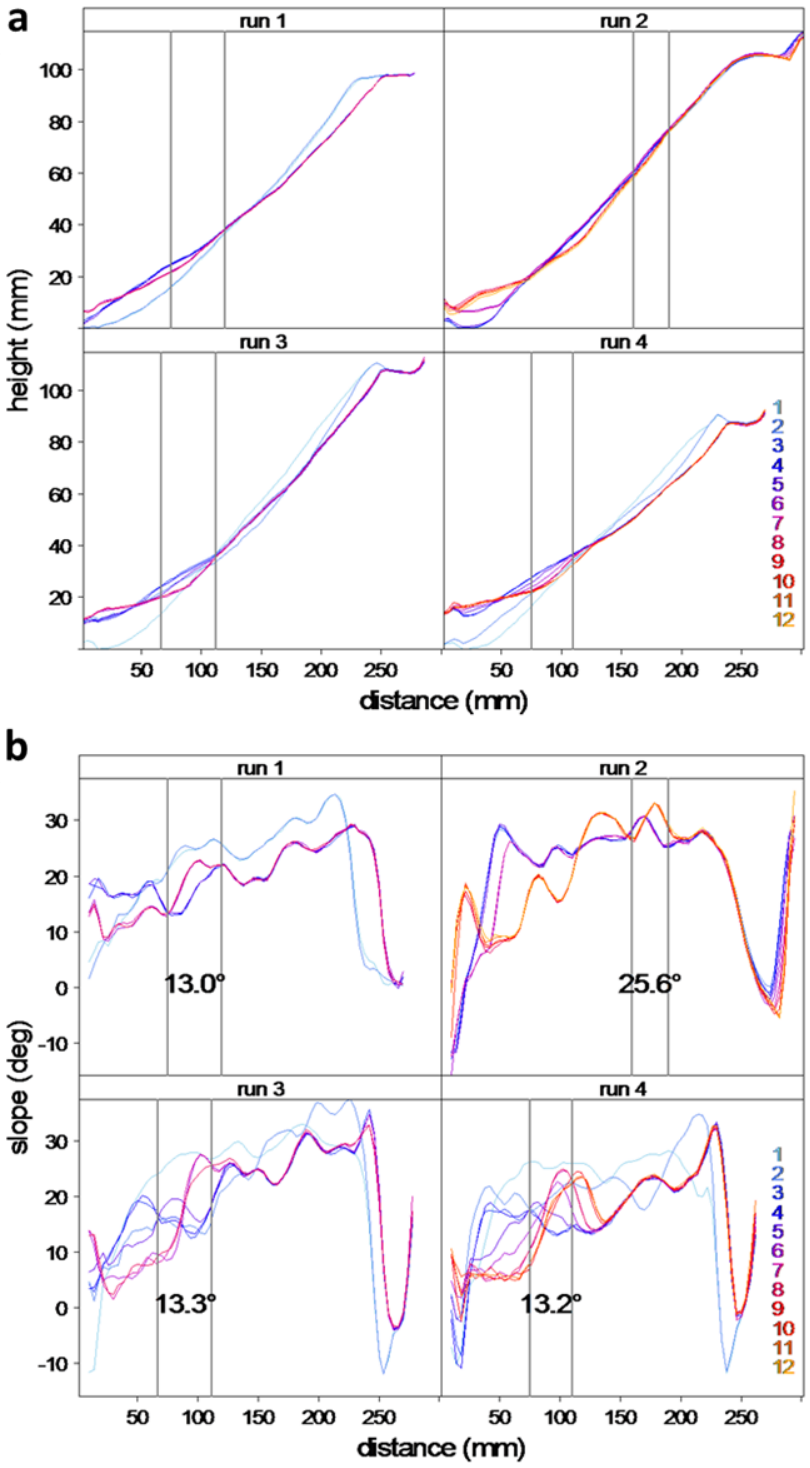


**Figure 2.8.** (a) Topographic long profiles of the three experimental runs. Colors indicate the time step for each profile. Region encompassed by grey vertical lines is the source area for late mass wasting events. (b) Corresponding slope profiles. Slopes given are the minimum slopes of the regolith within those zones.

**Table 2.2.** Mean slope heights used for determining slope angle uncertainties.

| | Control Run | Run 1 | Run 2 | Run 3 | Run 4 |
|---|---|---|---|---|---|
| Mean Height (cm) | 9.0 | 8.6 | 8.9 | 8.9 | 7.5 |

**Movie 2.1.** Example of a typical early slope failure. The failure starts mid-slope, just above the limit of visible surface frost. It grows to a maximum width of ~8 cm, eroding to within ~3 cm of the slope crest. Pitting can be observed at the toe of the slope, where deposition has mantled the surface frost. (Run 3 - normal speed).

**Movie 2.2.** Example of a low-angle, late slope failure associated with vigorous, sublimation-induced pitting of mantling regolith at the foot of the slope, giving the impression of boiling. (Run 3 - normal speed).

**Movie 2.3.** A representative sequence of late, low-angle, slumping failures, confined to the original limits of visible surface frost. (Run 4 - 64X normal speed).

**Movie 2.4.** Example of sustained slope failure during the period of maximum surface activity (Figure 2.3), eroding upslope into the crest. (Run 1 - normal speed).

## 2.10 Appendix B: Authorship Certification


**Arkansas Center for Space and Planetary Sciences**
**Stone House North**
**University of Arkansas**
**Fayetteville AR 27201**

**http://www.spacecenter.uark.edu**

E-mail: csaps@uark.edu

Office: (479) 575-7625
Fax: (479) 575-7778

April 13, 2018

To Whom it May Concern:

I hereby certify that my student Matthew Sylvest is the first author of this paper " Mass wasting triggered by seasonal CO2 sublimation under Martian atmospheric conditions: Laboratory experiments" and that he completed more than 51% of the work reported in the paper.

Sincerely

John C. Dixon
Professor Emeritus and Dissertation Director.

# 3 $CO_2$ Sublimation in Martian Gullies: Laboratory Experiments at Varied Slope Angle and Regolith Grain Sizes

M. E. Sylvest[1,2], J. C. Dixon[1], S. J. Conway[2,3], M. R. Patel[2,4], J. N. McElwaine[5,6], A. Hagermann[2] and A. Barnes[7]

[1]Arkansas Center for Space and Planetary Sciences, University of Arkansas, Fayetteville, Arkansas, USA.

[2]School of Physical Sciences, Open University, Milton Keynes, UK.

[3]Laboratoire de Planétologie et Géodynamique de Nantes-UMR CNRS 6112, Nantes, France.

[4]Space Science and Technology Department, STFC Rutherford Appleton Laboratory, Oxfordshire, UK.

[5]Department of Earth Sciences, Durham University, Durham, UK.

[6]Planetary Science Institute, Tucson, Arizona, USA.

[7]Center for Advanced Spatial Technologies, University of Arkansas, Fayetteville, Arkansas, USA.

**This chapter has been published.**
**Sylvest, M., Dixon, J., Conway, S., Patel, R., McElwaine, J., Hagermann, A., Barnes, A., 2018. $CO_2$ sublimation in martian gullies: laboratory experiments at varied slope angle and regolith grain sizes, *In*: Conway, S.J., Carrivick, J.L., Carling, P.A., de Haas, T. & Harrison, T.N. (eds) *Martian Gullies and their Earth Analogues.* Geological Society, London, Special Publications. https://doi.org/10.1144/SP467.11.**

## 3.1 Abstract

Martian gullies were initially hypothesized to be carved by liquid water, due to their resemblance to gullies on Earth. Recent observations have highlighted significant sediment transport events occurring in Martian gullies at times and places where $CO_2$ ice should be actively sublimating. Here we explore the role of $CO_2$ sublimation in mobilizing sediment through laboratory simulation. In our previous experimental work, we reported the first observations of sediment slope movement triggered by the sublimation of $CO_2$ frost. We used a Mars regolith simulant near the angle of repose. The current study extends our previous work by including two additional substrates, fine and coarse sand, and by testing slope angles down to 10°. We find that the Mars regolith simulant is active down to 17°, the fine sand is active only near the angle of repose and the coarse sand shows negligible movement. Using an analytical model, we show that under Martian gravity motion should be possible at even lower slope angles. We conclude that these mass-wasting processes could be involved in shaping Martian gullies at the present day and intriguingly the newly reported $CO_2$-creep process could provide an alternative explanation for putative solifluction lobes on Mars.

## 3.2 Introduction

When initially observed by the Mars Global Surveyor (Figure 3.1), Martian gullies were reasoned to have been formed by flowing water (Malin & Edgett 2000). With the observation of active modification and extension of gullies (Dundas et al. 2012), the apparent lack of liquid water under current Martian surface conditions leads to increased interest in alternative formative mechanisms. $CO_2$ is abundant on Mars, both as a gas (accounting for *c.* 95% of the atmosphere;

Bargery et al. 2011) and as solid ice at the surface. Although concentrated in seasonal polar ice caps (Hess et al. 1979), $CO_2$ ice has been detected on the surface at latitudes down to 32.3° S

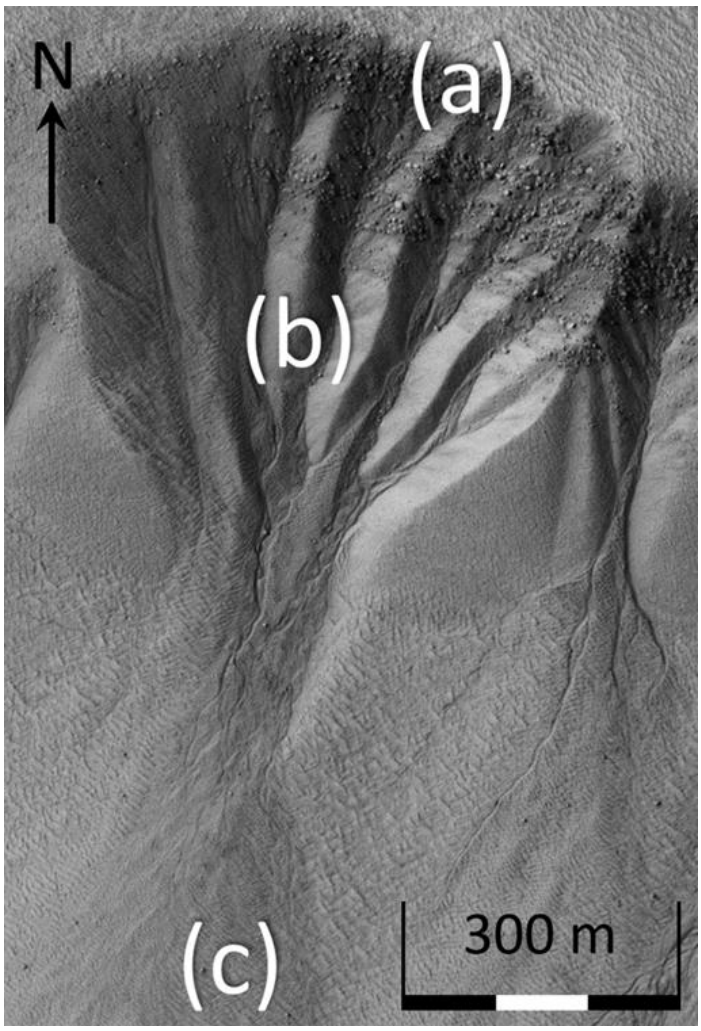


**Figure 3.1.** A HiRISE gully monitoring image of a series of typical Mars gullies with source alcoves converging downslope (a) into a transport channel (b), which opens onto extensive depositional fans (c). Image: ESP_048424_1105_red – NASA/JPL/University of Arizona.

(Vincendon 2015). Like Earth, the climate on Mars is seasonal, owing to the tilt of its axis of rotation relative to its orbital plane (25.2° v. 23.4° for Earth) driving winter expansion and summer retreat of the seasonal ice caps as the ice sublimates into the atmosphere (Hess et al. 1979).

Recent studies suggest that seasonal freezing and sublimation of $CO_2$ ice could be responsible for present-day gully activity on Mars (Diniega et al. 2010; Cedillo-Flores et al. 2011; Hansen et al. 2011; Dundas et al. 2012). These observations associate the timing of morphological changes with the seasonal $CO_2$ cycle (Reiss & Jaumann 2003; Dundas et al. 2010, 2012, 2014; Reiss et al. 2010; McEwen et al. 2011; Raack et al. 2015; Vincendon 2015; Pasquon et al. 2016) while experimental simulations (Diniega et al. 2013; Sylvest et al. 2016; Mc Keown et al. 2017) and numerical simulations (Cedillo-Flores et al. 2011; Pilorget & Forget 2016) demonstrate the efficacy of $CO_2$ slope mobilization models.

This work explores the ability of seasonal $CO_2$ frost to trigger slope failures of unconsolidated regolith. Previous experiments by Sylvest et al. (2016) established the ability of $CO_2$ frost to trigger mass wasting on slopes under Martian atmospheric conditions. Those experiments, however, were all conducted on slopes of JSC Mars-1 regolith simulant at approximately the angle of repose. This steep slope angle was chosen as it was the most likely to produce observable initial disruptions in a relatively short period of time. Yet clearly, Martian gullies and other mass wasting forms on Mars occur over a range of slope angles: for instance, gullies commonly occur on slopes ranging from 10° to 30° (Dickson et al. 2007; Conway et al. 2015). JSC Mars-1 is a fine-grained volcanic tephra ranging in size from 13 μm to 1 mm (Allen et al. 1998), yet on Mars there is an exceedingly wide range of grain size distributions to be found in the soils at the planet's surface, ranging from very fine sand to coarse sand, together with a fine dust component (McGlynn et al. 2011).

While there have been Mars-focused experimental studies undertaken on the role of slope on the morphological characteristics of slope disturbances under both Earth surface conditions

(Coleman et al. 2009; Jouannic et al. 2015) and Martian conditions (Jouannic et al. 2015), no studies have systematically examined the role of slope over a range of angles known to support a variety of mass wasting forms, including gullies. Similarly, a few experimental studies have systematically investigated the role of grain size in influencing the movement of debris under Martian atmospheric conditions (Conway et al. 2011a). These studies, however, examined water flow rather than $CO_2$ frost sublimation. The experiments reported in this paper explore the influence of sediment grain size and initial slope angle on the ability of sublimating $CO_2$ ice to trigger mass wasting under Martian conditions.

## 3.3 Methods

A total of 28 experimental runs, including two control runs, were performed in the Mars Simulation Chamber (MSC) at the Open University, Milton Keynes, UK (Figure 3.2). This


**Figure 3.2.** The Large Mars Planetary Environmental Simulations Chamber (centre), vacuum pump (bottom), liquid nitrogen supply (left) and $CO_2$ gas cooler (front left of centre).

cylindrical vacuum chamber, 2 m long by 1 m in diameter, is capable of replicating Martian atmospheric temperatures and pressures. Three regolith simulants were used at several initial slope angles, summarized in Table 3.1.

**Table 3.1.** Regolith simulants and initial slope angles

| Regolith simulant | Bulk density (g $cm^{-3}$) | Porosity | Permeability ($m^2$) | Particle density (g $cm^{-3}$) | Initial slope angles | | | | | |
|---|---|---|---|---|---|---|---|---|---|---|
| | | | | | 10° | 15° | 17.5° | 20° | 25° | AOR (*c.* 30°) |
| *JSC Mars-1 | 0.871 | 0.637 | $2.34 \times 10^{-12}$ | 2.40 | X | X | X | X | X | X |
| †Fine Sand | 1.68 | 0.373 | $1.51 \times 10^{-10}$ | 2.68 | X | X | n.d. | X | X | X |
| †Coarse Sand | 1.7 | 0.365 | $5.99 \times 10^{-10}$ | 2.68 | n.d. | n.d. | n.d. | n.d. | n.d. | X |

*Sizemore and Mellon, 2008
†Laboratory analysis from Conway *et al.* (2011*b*)
n.d. – no data

Each simulant was first tested at the angle of repose (AOR), as this is the least stable initial slope angle possible, and therefore the most likely condition to support the triggering of mass wasting (Sylvest et al. 2016). Subsequent angles were then selected based on the observed results of each previous run for that simulant.

The apparatus and procedures used for this work were adapted from Sylvest et al. (2016). Each run required preparation of the initial slope, preparation of the chamber atmosphere, cooling of the slope, condensation of $CO_2$ frost and, finally, sublimation of the frost. The only modifications to the methods of Sylvest et al. (2016) were in the initial slope preparation. Below, we present the slope preparation procedure and briefly summarize the remaining procedures.

Slope preparation started with vacuum drying the regolith, followed by stirring to disaggregate any clumps and to help maintain a consistent initial bulk density and grain sorting between runs (Sylvest et al. 2016). The initial slope angle was then prepared by raking the regolith into a smooth, uniform slope with a plastic spatula. The angle was checked with a spirit-level protractor at three locations across the crest slope zone (Figure 3.4a). The nominal slope angle for the run (Table 3.1) was based on the crest slope zone. The same *c.* 30 cm long, 20 cm wide, 12 cm deep test section from Sylvest et al. (2016) was reused.

The MSC was initially evacuated and purged with $N_2$ to remove moisture and provide a noncondensing atmosphere for the regolith cooling procedure. The regolith was cooled by flowing liquid $N_2$ through the test section coils (Sylvest et al. 2016) until the maximum near-surface temperature was cold enough to ensure condensation (−120°C, Table 3.5) of the relatively warm $CO_2$ gas (*c.* −20°C) at reduced chamber pressure (*c.* 350 mbar, Table 3.5). The chamber pressure typically reduced to *c.* 160 mbar during the cooling procedure, without pumping.

During the condensation procedure, $CO_2$ gas, cooled in a heat exchanger by the exhausted liquid N2 (Figure 3.2), was gently diffused (Figures 3.3d & 3.4b) over the regolith slope with the test section lid closed (Figures 3.3f & 3.4b). By keeping the lid closed, the $CO_2$ frost was prevented from forming on the horizontal photogrammetric markers which were glued to aluminium mounting surfaces. The chamber pressure was pumped down to a representative Mars surface pressure of 5–7 mbar (Table 3.5; Hess et al. 1980) during the final 20 min of the frost condensation procedure.

Finally, the test section lid was opened and the frosted regolith surface exposed to a simulated insolation of *c.* 350 W m−2 maximum heat flux (Table 3.5) while recording the surface with stereo videography for photogrammetric analyses (Figure 3.4b; Sylvest et al. 2016).

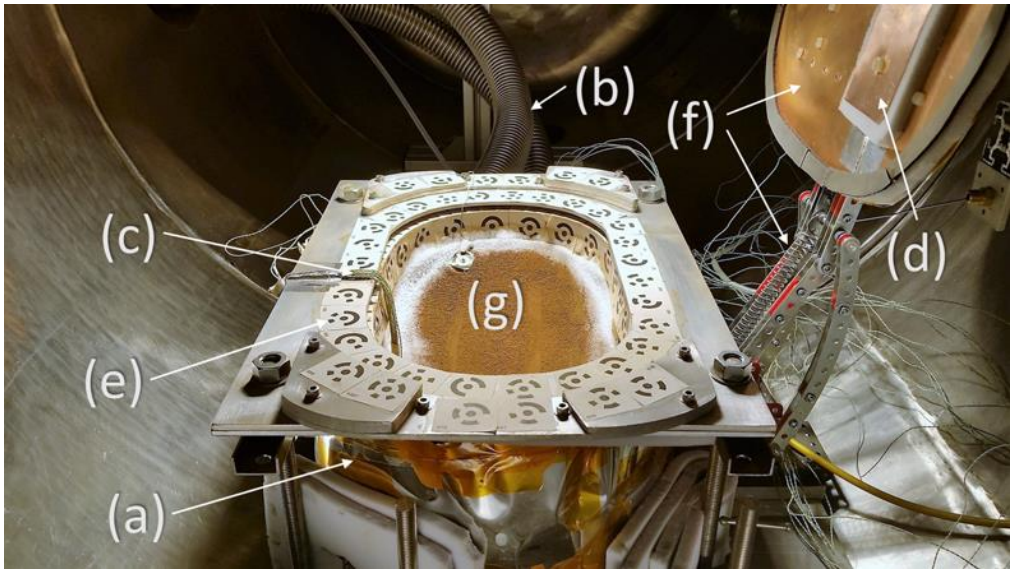


**Figure 3.3.** A view of an experiment inside the Mars chamber, at the start of sublimation. (a) The copper-coil regolith cooling box, externally insulated with open-celled foam and Mylar. (b) Insulated liquid nitrogen supply and exhaust lines. (c) Thermocouple wires were routed along the box wall and bottom to reach the thermocouple trees (Figure 3.4a) with minimal influence on the regolith. (d) The $CO_2$ inlet diffuser reduced the likelihood of disturbing the regolith surface during the condensation procedure. (e) Coded photogrammetric targets were affixed at multiple heights and orientations. (f) The box lid and actuator were used to isolate the regolith from thermal radiation during the cooling and condensation procedures, exposing the surface only for the sublimation procedure. (g) The regolith simulant for this run was JSC Mars-1. Parallel, long-slope marks were left from the protractor used during slope preparation.

For each run, initial and terminal slope angles were recorded manually. Temperatures were recorded continuously at several depths in two locations along the centreline of the slope (Figure 3.4a) and are summarized in Table 3.6. Pressure within the MSC was logged manually throughout each run (Sylvest et al. 2016).

### 3.3.1 Regolith simulants

JSC Mars-1, fine sand and coarse sand were selected as regolith simulants to identify possible controls on slope stability related to $CO_2$ ice sublimation, primarily owing to grain size distributions, but also to regolith composition. JSC Mars-1, a volcanic tephra, is the finest grained of the three simulants, with a broad grain size distribution from 13 μm to 1 mm (Allen et

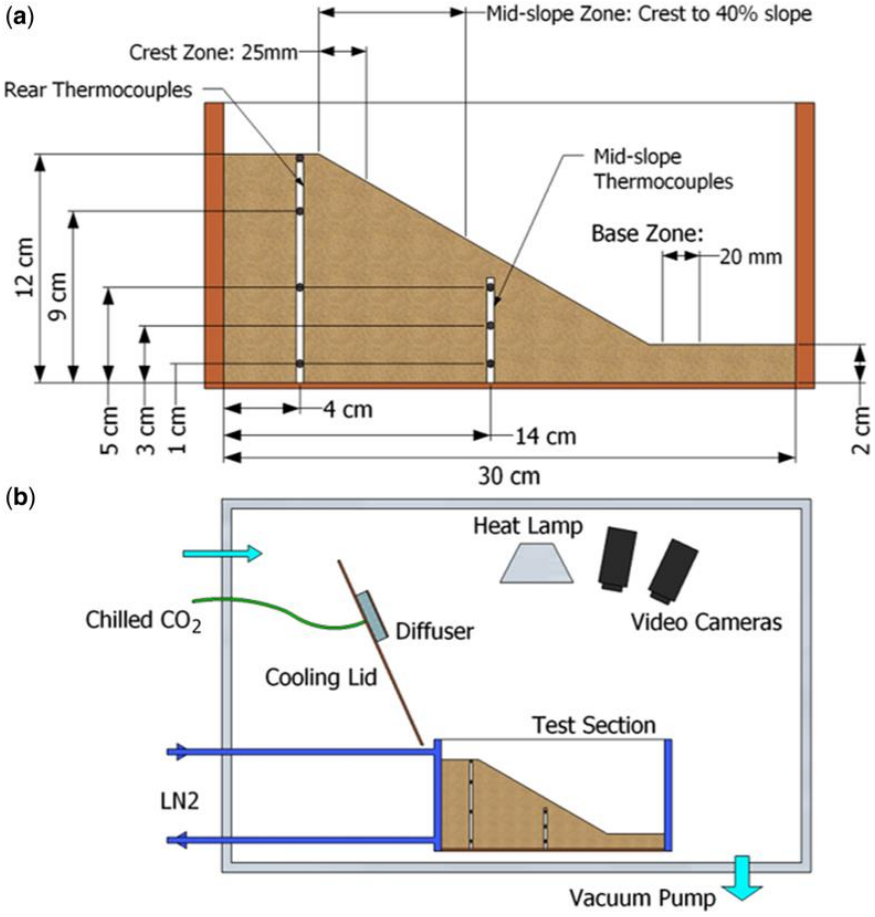


**Figure 3.4.** Mars Chamber schematics. (a) Cut-away of copper cooling box with nominal dimensions. The two thermocouple trees were positioned along the centreline of the box. In all but the first six runs, an additional thermocouple (not shown) was positioned near the surface at the toe of the slope, *c.* 2 cm from the box wall. The 'Crest', 'Mid-slope' and 'Base' slope zones are also indicated. (b) Interior of the Mars Chamber, llustrating the relative positions of the cooling box, video cameras and heat lamp. The cooling lid remained closed throughout the cooling and condensation procedures, and then opened for sublimation.

al. 1998). The fine sand regolith simulant is a well-sorted, dry silica sand with particle sizes between 100 and 300 μm. Based on sieve analysis, the coarse sand is poorly sorted, with particle sizes between 3 mm and 125 μm. The hydraulic properties pertinent to slope stability and fluid dynamic analyses of all three simulants are listed in Table 3.1. Grain size distributions are presented in Appendix A (Figures A1–A3).

### 3.3.2 Photogrammetric methods

The photogrammetric methods used for this study are an extension of those developed by Sylvest et al. (2016). As in that work, two identical Sony HDR-CX330 camcorders were used to simultaneously and stereoscopically record slope surface activity in high definition (Figure 3.4b). Coded photogrammetric targets were precisely located at multiple levels and orientations on the cooling box (Figure 3.3e). These targets provide external control for all aspects of the photogrammetric project, establishing a common three-dimensional frame of reference (and therefore scale) for all aspects of the photogrammetric models. The video recordings were then processed (Figure 3.5) to produce quantitative data. Each pair of videos was synchronized, and then image pairs were captured at 10 min time steps using Sony Vegas Pro 13 (Sylvest et al. 2016). The image pairs were imported into Agisoft PhotoScan Pro 1.2.6 and a series of digital elevation models (DEMs) was generated, one DEM for each time step.

There are two primary steps involved with the DEM production. The first step involves applying a photogrammetric bundle adjustment to determine interior (i.e. focal length, principal point and lens distortions) and exterior (i.e. camera positions and orientations) camera parameters. This step will henceforth be referred to as image alignment. The second step is the extraction of a dense 3D surface using multi-view stereo techniques. It is important to note that

the two primary camera positions provided full stereoscopic coverage for all coded targets and the experimental surface. However, typically more than two camera positions are necessary to photogrammetrically model the above-mentioned camera parameters. Therefore, in order to improve the overall geometry of the photogrammetric block, the two primary camera positions were supplemented with images recorded from various positions around the box before the start of cooling, thus providing a much larger, virtual set of cameras. The use of these additional camera positions and coded targets with known coordinates (i.e. control points) provides a strong photogrammetric network with a reprojection error of less than one pixel.

During the image alignment step in PhotoScan, the regolith surface was masked out of each image and a sparse set of 3D tie points was generated using the 'Align Photos' tool. This process involves automatically detecting and matching corresponding features across overlapping images. The coded targets were also detected by PhotoScan and the known coordinates for these targets were provided. In some instances, PhotoScan incorrectly measured and/or labelled the coded targets and manual adjustments of the marker(s) were necessary (Figure 3.5). After necessary marker corrections were made, the photogrammetric block was then optimized using the bundle adjustment. Next, a dense 3D surface was extracted from the primary image pair and the resulting surface geometry compared with the known dimensions of the box. If the model was unsatisfactory, the marker locations for each coded target were manually refined in each image, and additional tie points could be added, based on the nature of the error. This process was repeated (Figure 3.5) until consecutive results were unimproved.

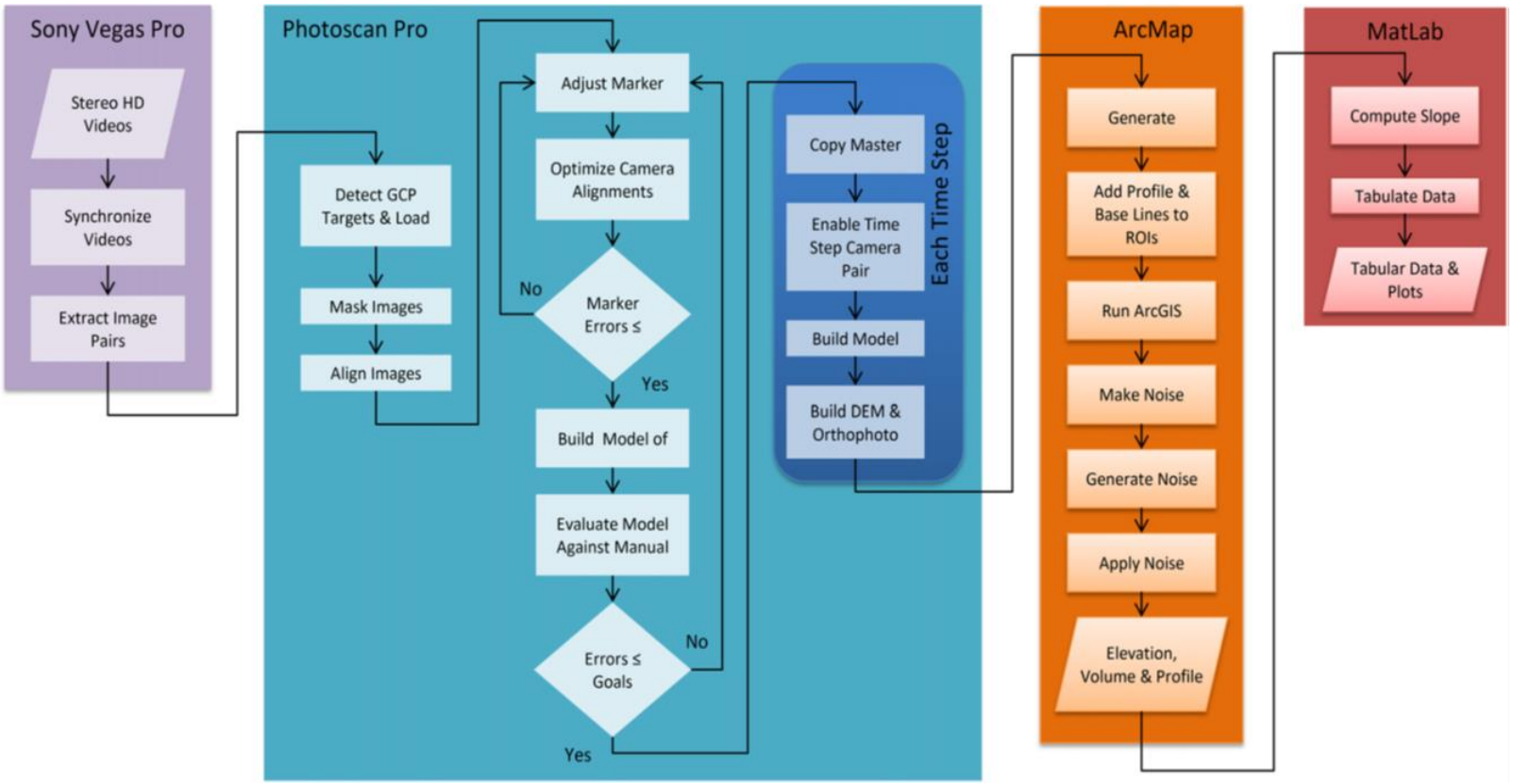


**Figure 3.5.** Photogrammetric pipeline. The procedure for extracting data from the stereo video recordings made use of three principal software packages. Sony Vegas Pro was used to synchronize and extract coordinated image pairs for each DEM. Photoscan Pro was used to develop the DEMs based on the image pairs and physically measured target locations. Additionally, known hardware dimensions and measured slope angles were used to evaluate the accuracy of each DEM. The DEMs were then processed with ArcMap to derive volumetric and angular changes between DEMs. Finally, MatLab was used to compute slope angles and prepare the data for interpretation and presentation.

After the image alignment procedure, a sequence of DEMs (e.g. Figure 3.7b) at 1mm/pixel resolution were produced (one for each pair of images), now masking all but the slope inside the box. Likewise, a sequence of corresponding orthophotos at *c.* 0.29 mm/ pixel (e.g. Figure 3.7a) was produced. Rasters of the elevation differences between consecutive DEMs were calculated in ESRI ArcMap 10.3.1. The region of interest (ROI) for each sequence of DEMs was determined within ArcMap by combining all the orthophotos for the sequence into a single shape that encapsulates the full extents of all the DEMs.

The difference rasters were multiplied by the DEM cell size (1 × 1 mm) to determine the erosional and depositional volumes. The volume of frost condensed on each slope was taken as the net deposition between the pre-condensation time step and the start of the sublimation procedure. The DEMs were also used to generate long profiles, used to characterize slope angles. The long profiles were generated by constructing a ROI 4 cm wide along the length of the slope in each DEM and averaging the heights every 4 mm along the slope. Linear least squares fits were applied to the binned data in the three zones, crest, mid and base, as indicated in Figure 3.4a.

In order to reduce systematic volumetric noise artefacts in the DEMs, a new filtering procedure was added to the original methodology of Sylvest et al. (2016). For each difference raster, representing the change elevations between two DEMs, ArcMap was used to find contiguous volumes of transported regolith. A mask was generated by eliminating all but those volumes with areal extents below an interactively determined threshold, typically around 40 $cm^2$. This volume filter mask was then applied to the original difference raster, thereby reducing the photogrammetric noise. The filtered results were then imported into MathWorks Matlab 2016a in

order to calculate slope angles and changes of angle for each slope zone (Figure 3.4b), as well as to tabulate and plot the data.

### 3.3.3 Control runs and error estimation

The list of potential sources of error in the photogrammetric results, and the difficulty in assessing the contribution of any one of these sources, renders a direct error computation impractical (Raack et al. 2017). In order to quantify the 'uncertainty envelope' on a case-by-case basis, we evaluated differences in DEMs for slope regions known (by observation) to be devoid of sediment movement (as detailed later in this section). Table 3.7 lists the potential sources of error we have identified with our methods.

Control runs were performed for JSC Mars-1 and fine sand. A control run was deemed unnecessary for coarse sand, given the lack of substantial sediment movement observed for those runs. No sediment transport was observed for either of the two control runs. The control runs were configured at an initial slope at the static AOR and followed the same protocol used for the data runs, except that no $CO_2$ was introduced into the chamber during the condensation phase of the experiment. (See Sylvest et al. 2016 for full details of the experimental procedures.)

We did not use the control runs to calculate the errors on volumes and slopes, as potential sources of error, such as those listed in Table 3.4, varied between runs. For example, dense accumulations of surface frost are particularly difficult to model under the harsh lighting of the simulated insolation. The direction and intensity of the lamp (Figure 3.4b) tends to eliminate shadows necessary to detect the surface features, which in turn are required for the dense surface reconstruction. Also, the high albedo of the frost tends to oversaturate the camera sensor, further obscuring features on the surface of the frost. Hence, during runs with more extensive surface

frost coverage, noise in the surface model was more significant than for other runs. To allow for these variabilities, we developed a method to estimate errors using the difference DEMs for each run individually. Specifically, for each run, a small ROI (4.67 $cm^2$) was located on a portion of the slope where no movement was visually observed. The vertical noise was estimated as the mean change of elevation over the ROI, when comparing the first and last DEMs of the run. As in Sylvest et al. (2016), horizontal coordinate error estimates were based on the RMS errors for the coded target locations reported by PhotoScan, which were *c.* 1.0 mm for all runs. The equivalent vertical error for each of the runs, derived from the noise estimation procedure described above, ranged from 0.43 to 2.29 mm (Appendix A, Table 3.9). As in Sylvest et al. (2016), the standard accumulation of errors formulae were applied to these numbers in order to provide error estimates for each measured result.

## 3.4 Results

In the following sections, we describe the shared features of all the experiments, including how these volumes of sediment were transported, their magnitudes and the observed changes in slope angle. Then, we discuss the results for each sediment type separately.

### 3.4.1 Quantitative results

Substantial volumes of sediment were transported for JSC Mars-1 at initial slope angles from 17.5° to the AOR (*c.* 30°) and for fine sand at the AOR (Table 3.2). Between 1% and 14% of the total sediment volume was transported at initial target slope angles between 17.5° and the static angle of repose (AOR *c.* 30°) for JSC Mars-1, while between 2% and 4% of the total sediment volume was transported at the AOR for fine sand, also *c.* 30° (Table 3.3). Measured volumes of observed sediment transport for coarse sand at the AOR were less than 1% of the slope volume,

well below the noise level of the photogrammetric results of 1.3% of the total slope volume (run 26, Table 3.5). Owing to the lack of sediment transport for coarse sand at the AOR, no additional runs were conducted with gentler slopes (Table 3.2). The maximum volumes eroded and deposited for all runs were 10.9% and 14.0% of the total slope volume, respectively, both recorded for run 24 (Table 3.3). These volumes correspond to maximum changes in slope elevation 47 mm for erosion, and 42 mm for deposition (Table 3.3).

**Table 3.2.** Summary of regolith movement vs. initial slope angle

| | 10° | 15° | 17.5° | 20° | 25° | AOR (*c.* 30°) |
|---|---|---|---|---|---|---|
| JSC Mars-1 | o | O | ✓ | ✓ | n.d. | ✓ |
| Fine Sand | ✓ | O | n.d. | o | o | ✓ |
| Coarse Sand | n.d. | n.d. | n.d. | n.d. | n.d. | ✓ |

'✓'—substantial slope movement observed.
'o'—no substantial slope movement observed.
n.d.—no data for this initial slope angle.
Angles are initial target slope angles. Photogrammetrically measured values are presented in Table 3.3.
AOR: Static angle of repose

Initial and final slope angles for each slope zone (Figure 3.4a) are reported in Table 3.3, along with their associated angular changes. For the majority of the 25 runs with photogrammetric data, the angles of the crest and mid-slope zones changed very little (−1.1 ± 0.4° and −1.3 ± 0.4° on average, respectively). Only two JSC Mars-1 runs (runs 20 and 24, Table 3.3) underwent crest slope angle reductions greater than 8°. Base slope zone angles reduced by 3.6 ± 0.3° on average. No statistically significant correlations were found between initial slope

angle or initial frost volume with elevation, volumetric or angular changes (see Appendix A for correlation results).

### 3.4.2 Sediment transport types

Sediment transport was observed in 20 of the 26 experimental runs conducted. Four types of sediment transport were identified in various combinations for each of the runs in Table 3.4. The most readily observed type is discrete granular flow. These flows are up to several centimetres wide and can extend as far as the base of the slope, where they form depositional fans and lobes. They generally display well-defined areal extents and occur on all but the gentlest slopes. When occurring concurrently, discrete flows frequently coalesce into larger composite flows, occasionally encompassing the full breadth and majority of the length of the slope. These flows can initiate on slope regions with no topographically induced instabilities, but only initiate on regions devoid of visible surface frost. Discrete granular flows were present in 19 of the 20 runs in which sediment transport was observed and recorded.

Second, in terms of volume transport, creep movements are more difficult to observe, generally requiring accelerated video playback to see their subtler movements. However, the areal extents of some creep movements were large enough to suggest substantial sediment transport

**Table 3.3.** Slope angle, elevation and volume changes

| Run ID | Sediment | Nominal slope angle [°] | Base slope angle | | | Mid-slope angle | | | Crest slope angle | | | Elevation Change | | | Volumes | | | |
|---|---|---|---|---|---|---|---|---|---|---|---|---|---|---|---|---|---|---|
| | | | Initial [°] | Final [°] | Change [°] | Initial [°] | Final [°] | Change [°] | Initial [°] | Final [°] | Change [°] | Erosion [mm] | Deposition [mm] | Mean [mm] | Regolith total [$cm^3$] | Erosion [$cm^3$] | Deposition [$cm^3$] | Frost [$cm^3$] |
| 1 | Fine Sand | 10° | 10.21±0.07 | 10.60±0.08 | 0.39±0.10 | 11.97±0.09 | 11.80±0.08 | -0.17±0.12 | 12.64±0.09 | 12.66±0.09 | 0.02±0.13 | -4.00±0.57 | 11.00±0.57 | -0.05±0.04 | 3622±26 | 14.87±0.11 | 13.38±0.10 | 33.49±0.24 |
| 2 | Fine Sand | 15° | 14.28±0.09 | 14.22±0.09 | -0.06±0.13 | 16.94±0.11 | 16.60±0.10 | -0.34±0.15 | 22.33±0.14 | 21.60±0.13 | -0.73±0.19 | -6.00±0.47 | 0.00±0.47 | -0.24±0.01 | 3276±20 | 10.63±0.07 | 0.00±0.00 | 16.52±0.10 |
| 3 | Fine Sand | 20° | 23.33±0.23 | 24.27±0.24 | 0.94±0.34 | 21.98±0.22 | 21.68±0.22 | -0.30±0.31 | 22.43±0.22 | 22.62±0.23 | 0.19±0.32 | -4.00±0.82 | 0.00±0.82 | -0.20±0.01 | 3154±32 | 7.55±0.08 | 0.00±0.00 | 19.07±0.19 |
| 4 | Fine Sand | 25° | 23.15±0.21 | 22.94±0.21 | -0.21±0.30 | 23.34±0.21 | 22.95±0.21 | -0.39±0.30 | 23.08±0.21 | 22.68±0.21 | -0.40±0.30 | -3.00±0.64 | 6.00±0.64 | 0.44±0.02 | 2712±25 | 1.69±0.02 | 17.72±0.16 | 51.89±0.47 |
| 5 | Fine Sand | 25° | 25.76±0.18 | 25.88±0.18 | 0.12±0.26 | 24.33±0.17 | 24.07±0.17 | -0.26±0.24 | 25.53±0.18 | 24.56±0.17 | -0.97±0.25 | -3.00±0.54 | 7.00±0.54 | 0.10±0.02 | 3478±25 | 4.61±0.03 | 11.91±0.08 | 79.96±0.57 |
| 6 | Fine Sand | AOR | 34.02±0.61 | 32.51±0.58 | -1.51±0.84 | 30.97±0.55 | 30.43±0.54 | -0.54±0.78 | 32.97±0.59 | 29.26±0.52 | -3.71±0.79 | -8.00±1.32 | 5.00±1.32 | -1.56±0.03 | 3391±61 | 75.92±1.36 | 1.55±0.03 | 20.28±0.36 |
| 7 | Fine Sand | AOR | 34.91±0.32 | 30.47±0.28 | -4.44±0.42 | 30.43±0.28 | 30.50±0.28 | 0.07±0.39 | 31.23±0.28 | 30.93±0.28 | -0.30±0.40 | -7.00±0.59 | 23.00±0.59 | -0.49±0.07 | 3057±28 | 69.13±0.62 | 42.36±0.38 | 12.76±0.12 |
| 8 | Fine Sand | AOR | 31.07±0.96 | 25.32±0.79 | -5.75±1.24 | 31.01±0.96 | 27.58±0.86 | -3.43±1.29 | 29.07±0.90 | 33.62±1.04 | 4.55±1.38 | -12.00±2.29 | 16.00±2.29 | 0.91±0.06 | 3471±108 | 88.85±2.75 | 131.14±4.07 | 37.97±1.18 |
| 9 | JSC Mars-1 | 10° | 9.54±0.07 | 8.81±0.06 | -0.73±0.09 | 11.44±0.08 | 11.16±0.08 | -0.28±0.11 | 15.45±0.11 | 14.60±0.11 | -0.85±0.15 | -5.00±0.58 | 3.00±0.58 | 0.06±0.02 | 3322±24 | 2.84±0.02 | 5.34±0.04 | 1.01±0.01 |
| 10 | JSC Mars-1 | 15° | 13.18±0.09 | 13.86±0.09 | 0.68±0.13 | 14.46±0.10 | 14.45±0.10 | -0.01±0.14 | 15.94±0.11 | 15.74±0.11 | -0.20±0.15 | -7.00±0.54 | 4.00±0.54 | -0.05±0.02 | 4158±28 | 12.84±0.09 | 1.46±0.01 | 4.28±0.03 |
| 11 | JSC Mars-1 | 15° | 12.08±0.08 | 11.91±0.08 | -0.17±0.11 | 15.21±0.10 | 15.20±0.10 | -0.01±0.14 | 16.58±0.11 | 16.43±0.11 | -0.15±0.16 | -4.00±0.57 | 0.00±0.57 | -0.23±0.01 | 4296±29 | 6.58±0.04 | 0.00±0.00 | 20.37±0.14 |
| 12 | JSC Mars-1 | 15° | 17.24±0.21 | 17.22±0.21 | -0.02±0.29 | 17.87±0.22 | 17.54±0.21 | -0.33±0.30 | 23.79±0.29 | 23.50±0.28 | -0.29±0.40 | -6.00±1.00 | 0.00±1.00 | -0.39±0.01 | 3872±47 | 23.43±0.28 | 0.00±0.00 | 45.43±0.55 |
| 13 | JSC Mars-1 | 17.5° | 22.99±0.24 | 20.81±0.22 | -2.18±0.32 | 18.29±0.19 | 18.61±0.19 | 0.32±0.27 | 21.86±0.23 | 20.86±0.22 | -1.00±0.32 | -13.00±0.83 | 5.00±0.83 | -0.11±0.04 | 3949±41 | 17.95±0.19 | 15.68±0.16 | 3.98±0.04 |
| 14 | JSC Mars-1 | 17.5° | 21.27±0.18 | 18.86±0.16 | -2.41±0.24 | 16.94±0.14 | 17.42±0.15 | 0.48±0.20 | 17.60±0.15 | 16.67±0.14 | -0.93±0.20 | -8.00±0.69 | 14.00±0.69 | 0.87±0.05 | 3672±31 | 25.08±0.21 | 8.22±0.07 | 11.46±0.10 |
| 15 | JSC Mars-1 | 17.5° | 18.06±0.09 | 17.65±0.09 | -0.41±0.13 | 18.27±0.10 | 17.86±0.09 | -0.41±0.13 | 18.71±0.10 | 16.81±0.09 | -1.90±0.13 | -4.00±0.43 | 11.00±0.43 | 1.46±0.03 | 4055±21 | 0.00±0.00 | 67.44±0.35 | 113.06±0.59 |
| 16 | JSC Mars-1 | 17.5° | 14.65±0.13 | 17.17±0.15 | 2.52±0.20 | 17.78±0.16 | 17.34±0.15 | -0.44±0.22 | 14.64±0.13 | 15.10±0.13 | 0.46±0.19 | -6.00±0.72 | 8.00±0.72 | -0.81±0.03 | 3995±35 | 1.57±0.01 | 20.03±0.18 | 27.76±0.25 |
| 17 | JSC Mars-1 | 20° | 23.42±0.21 | 20.44±0.19 | -2.98±0.28 | 18.07±0.17 | 17.89±0.16 | -0.18±0.23 | 14.42±0.13 | 12.16±0.11 | -2.26±0.17 | -8.00±0.70 | 8.00±0.70 | -0.47±0.04 | 3477±32 | 19.46±0.18 | 14.57±0.13 | 4.02±0.04 |
| 18 | JSC Mars-1 | 20° | 18.85±0.30 | 14.63±0.23 | -4.22±0.38 | 19.17±0.31 | 19.17±0.31 | 0.00±0.43 | 12.17±0.20 | 12.61±0.20 | 0.44±0.28 | 0.00±0.71 | 9.00±0.71 | 1.40±0.02 | 2302±35 | 30.17±0.46 | 78.36±1.20 | 18.47±0.28 |
| 19 | JSC Mars-1 | 20° | 22.00±0.28 | 18.91±0.24 | -3.09±0.37 | 17.00±0.22 | 16.45±0.21 | -0.55±0.30 | 16.90±0.22 | 16.48±0.21 | -0.42±0.30 | 0.00±0.55 | 6.00±0.55 | 0.88±0.01 | 2102±27 | 2.40±0.03 | 72.66±0.93 | 56.83±0.73 |
| 20 | JSC Mars-1 | AOR | 23.20±0.18 | 16.93±0.13 | -6.27±0.22 | 34.06±0.26 | 27.36±0.21 | -6.70±0.34 | 39.53±0.30 | 30.20±0.23 | -9.33±0.38 | -18.00±0.79 | 18.00±0.79 | 0.92±0.08 | 4779±37 | 150.43±1.16 | 187.60±1.44 | 113.61±0.87 |
| 21 | JSC Mars-1 | AOR | 24.96±0.28 | 9.96±0.11 | -15.00±0.30 | 26.56±0.30 | 28.36±0.32 | 1.80±0.43 | 22.25±0.25 | 23.17±0.26 | 0.92±0.36 | -9.00±0.95 | 14.00±0.95 | -0.55±0.05 | 4054±45 | 78.06±0.87 | 45.59±0.51 | n/d |
| 22 | JSC Mars-1 | AOR | 22.53±0.33 | 8.58±0.13 | -13.95±0.35 | 27.47±0.40 | 24.51±0.36 | -2.96±0.54 | 27.52±0.40 | 29.13±0.43 | 1.61±0.59 | -13.00±1.32 | 24.00±1.32 | 0.34±0.08 | 4737±69 | 136.92±2.01 | 154.34±2.26 | 41.95±0.62 |
| 23 | JSC Mars-1 | AOR | 23.88±0.47 | 5.76±0.11 | -18.12±0.49 | 25.04±0.50 | 21.33±0.42 | -3.71±0.65 | 23.87±0.47 | 27.54±0.55 | 3.67±0.72 | -13.00±1.37 | 24.00±1.37 | 2.11±0.09 | 2917±58 | 78.73±1.56 | 157.71±3.12 | 108.01±2.14 |
| 24 | JSC Mars-1 | AOR | 31.66±0.22 | 19.60±0.14 | -12.06±0.26 | 29.35±0.20 | 16.36±0.11 | -12.99±0.23 | 35.60±0.25 | 20.64±0.14 | -14.96±0.28 | -47.00±0.55 | 42.00±0.55 | 2.33±0.21 | 3726±26 | 373.81±2.58 | 481.96±3.32 | 37.15±0.26 |
| 25 | Coarse Sand | AOR | n/d | n/d | n/d | n/d | n/d | n/d | n/d | n/d | n/d | n/d | n/d | n/d | n/d | n/d | n/d | n/d |
| 26 | Coarse Sand | AOR | 30.79±0.49 | 30.00±0.48 | -0.79±0.68 | 33.79±0.54 | 31.98±0.51 | -1.81±0.74 | 32.51±0.52 | 32.26±0.51 | -0.25±0.73 | -5.00±1.20 | 15.00±1.20 | 0.50±0.05 | 3605±57 | 9.98±0.16 | 32.23±0.51 | 64.80±1.03 |

n/d: No data

**Table 3.4.** Observed sediment transport types

| | | | Discrete flow | | Creep | | Gas entrainment | | Grain tumbling | |
|---|---|---|---|---|---|---|---|---|---|---|
| Run ID | Regolith simulant | Initial slope angle | Timing [s] | Areas | Timing [s] | Areas | Timing [s] | Areas | Timing [s] | Areas |
| 1 | Fine sand | 10° | | | | | | | | |
| 2 | Fine sand | 15° | | | | | | | | |
| 3 | Fine sand | 20° | | | | | | | | |
| 4 | Fine sand | 25° | | | | | | | | |
| 5 | Fine sand | 25° | | | | | | | | |
| 6 | Fine sand | AOR | | | 30 – 6720 | Mid & crest edges | | | | |
| 7 | Fine sand | AOR | 2509 – 4007 | Centre, base | 3483 – 5952 | Full width, mid | 3880 – 4019 | Toe bubbling | | |
| 8 | Fine sand | AOR | 588 – 666 | Crest-toe | 312 – 5979 | Crest-toe | | | | |
| Control* | Fine sand | AOR | | | | | | | | |
| 9 | JSC Mars-1 | 10° | | | 166 – 913 | Mid & crest edges | 373 – 5589 | Crest TC tree | | |
| 10 | JSC Mars-1 | 15° | 174 – 420 | Lower Mid; crest TC[§] tree | 42 – 1112 | Mid; along frost edges | 252 – 5962 | Crest & mid TC tree; eroded & slumped areas | | |
| 11 | JSC Mars-1 | 15° | 60 – 186 | Mid | 810 – 1260 | Mid & base | 60 – 6055 | TC trees & proximal; along frost edges | | |
| 12 | JSC Mars-1 | 15° | 5236 – 5237 | Mid; RHS mid | 155 – 5368 | Base; upper mid | | | | |
| 13 | JSC Mars-1 | 17.5° | 18 – 574 | Crest & mid | 171 – 1058 | Base deposits | 0 – 6367 | Crest along frost edge; vigorous boiling toe deposits | | |
| 14 | JSC Mars-1 | 17.5° | 32 – 780 | Mid | | | 171 – 6257 | Crest TC tree; base & toe | | |
| 15 | JSC Mars-1 | 17.5° | 682 – 6049 | Mid; mid & crest | 99 – 5219 | Mid | 444 – 6065 | Upper TC tree; mid TC tree | | |
| 16 | JSC Mars-1 | 17.5° | 41 – 6651 | Mid & crest | 0 – 789 | Mid & base | 44 – 6541 | Crest & mid TC trees | | |
| 17 | JSC Mars-1 | 20° | 240 – 4625 | Mid & sink holes RHS | | | 490 – 8106 | Toe & crest TC tree; RHS mid | | |
| 18 | JSC Mars-1 | 20° | 140 – 2181 | Crest; crest, mid & base | | | 231 – 6060 | Base deposits; mid TC tree | | |
| 19 | JSC Mars-1 | 20° | 162 – 547 | Mid & LHS crest | | | 369 – 6051 | Mid frost edge; toe & base deposits | | |
| 20 | JSC Mars-1 | AOR | 317 – 2997 | Crest; mid & base | 2989 – 4354 | Mid & base | 883 – 4354 | Toe deposits | | |
| Control* | JSC Mars-1 | AOR | | | | | | | | |
| 21 | JSC Mars-1 | AOR | 124 – 3777 | Mid; mid & crest | | | 2482 – 2496 | Toe deposits | | |
| 22 | JSC Mars-1 | AOR | 333 – 5018 | Mid to crest | | | 335 – 5159 | Toe dust deposits; base deposits | | |
| 23 | JSC Mars-1 | AOR | 168 – 6500 | Mid; mid & crest | 570 – 4863 | Base & mid | 328 – 7187 | Base & toe deposit pitting; mid eroded areas pitting | | |
| 24 | JSC Mars-1 | AOR | 51 – 6762 | Mid; crest | 189 – 6762 | Mid, base & toe | 3821 – 6762 | Base & toe boiling deposits; crest to toe pitting. | | |
| 25 | CsAORr1 | AOR | 1560 – 1563 | RHS Mid (ice) | 1563 – 7320 | Mid & crest | | | 0 – 6880 | Entire slope |
| 26 | CsAORr2 | AOR | 4702 – 4703 | RHS Mid | 1000 – 5193 | Base, mid & crest edges | | | 0 – 5193 | Entire slope |

Notes: Empty cells indicate no observed activity. *Initial slope angle based on mid-slope zone (Figure 3.4a). Control run (no $CO_2$ admitted to chamber). [§]TC = Thermocouple.

volumes. Fourteen of the 26 runs were affected by creep (Table 3.4). Creep was not confined to any particular slope region; however, it was frequently present at the boundaries of retreating surface ice accumulations. These movements presented as narrow (<1 cm wide) bands of sediment, adjacent to and following the trailing edge of the retreating ice.

Sixteen of the 26 runs displayed obvious signs of gas entrainment of regolith particles. Although a common phenomenon, entrainment did not appear to be an effective sediment transport process on its own. Entrainment was most obvious at the toe of the slope, where sediment was deposited over surface frost. In these instances, the dusty surface gave the impression of boiling, owing to the vigorous sublimation of the shallowly buried frost. Evidence of escaping gas was also frequently observed where the thermocouple stations came close to, or in some cases became exposed at, the slope surface. These circular areas of activity were typically smaller and less active than the active areas at the slope base. For runs with JSC Mars-1 at initial slope angles less than the angle of repose, fine dust deposits on the upslope box boundaries suggest that dust particles were entrained in the flow of $CO_2$ gas escaping from under the regolith along the warming box edge.

The fourth sediment transport type was the rolling and tumbling of individual, isolated grains; henceforth simply referred to as tumbling. Although tumbling grains of frost were common for many of the runs, they had no apparent effect on the underlying regolith; nor were they observed to trigger other modes of transport. Tumbling regolith particles were only observed in the two coarse sand runs (Table 3.4). This may be due in part to the much smaller, more uniform grain sizes of JSC Mars-1 and fine sand (Table 3.1). As for creep, accelerated video playback speeds facilitate observation of these small (1–2 particle diameters) movements

which occurred over the entire extent of the slope. As for tumbling ice particles, tumbling sediment neither moved substantial volumes of material, nor did it trigger other sediment movements.

### 3.4.3 Regolith-specific results

#### 3.4.3.1 JSC Mars-1

##### 3.4.3.1.1 JSC Mars-1 sediment movement types

JSC Mars-1 was the most active of the three regolith simulants. Discrete granular flows were detected for all but the one run with the gentlest initial slope angle (11.4 ± 0.1° for run 9 in Table 3.4). Creep was detected in 10 of the 16 runs with JSC Mars-1; and gas entrainment was observed in all but one run (run 12 in Table 3.4). Correlating sediment movements (Table 3.4) with the initial slope angle of the corresponding slope zone (Figure 3.4a), discrete flow initiation was identified on slopes between 12.2° and 39.5°, while creep initiated on slopes between 11.4° and 33.9° (Table 3.3). The observed behaviour of discrete granular flows revealed a dependence on initial slope angle. For JSC Mars-1, run 9 (Table 3.4), with an initial slope angle of *c.* 10°, was the only run that did not display any discrete flow events. Flows became both larger and more numerous with increasing steeper slope angles. The maximum width of flows increased with initial slope angle from *c.* 1 cm at 15° slopes and reaching the full slope width (*c.* 20 cm) for initial slopes of 20°. All runs starting at the AOR displayed discrete flows up to the full width of the slope, with runouts from crest to the bottom limit of the box. Maximum runouts started at less than 2 cm for 15° slopes and increasing to 6 cm at 17.5° initial slopes. For initial slopes below 20°, flows primarily took the form of slumps, leaving an upslope recess and a downslope berm of displaced sediment just below the recess. At steeper angles, flows appeared to skim, rather than slide over, the downslope surface, particularly flows starting at the AOR. For these

steepest runs, flows frequently initiated at the crest, leaving a sharp break of slope, which receded with continued flow activity.

As seen in Table 3.4, creep was detected in runs covering the full span of tested initial slope angles (10° to *c.* 30°). Conspicuously, creep was not detected for any of the runs starting at 20°. With the exception for run 9 (Table 3.4), creep was not detected in the crest zone (Figure 3.4a), and in that instance, was only present at the edges, adjacent to the box. Gas entrainment activity was relatively independent of slope angle, except where it modified deposits from previously transported sediment.

#### 3.4.3.1.2 JSC Mars-1 morphology observations

Slope failures on JSC Mars-1 slopes produced a variety of morphological changes on the surface. Discrete slope failures leave clearly defined areas of erosion and deposition, with distinct boundaries (Figure 3.6). While the steepness of crest regions near the top of the slope did generally decrease, sharp breaks in slope were maintained through crest retreat, observed in several runs. Scarp-like features were frequently observed on eroded slope faces (Figure 3.6a, b). For larger volumes, discrete slope failures, eroded material was carried to the bottom of the slope, colliding with the end of the test section with sufficient energy to create large clouds of dust, briefly obscuring the entire slope. Centimetre-scale puffs of dust, entrained by jets of escaping subsurface gas, were also observed. The timing of these events is difficult to constrain, given their brief duration and small scale, combined with near-vertical camera angles. Broadly, they occurred within the periods of gas entrainment activity listed in Table 3.4, beginning as early as the onset of sublimation up to halfway (48%) through the period, and ending from 32% to 98% through the sublimation period (Table 3.4). Jets adjacent to the box sides left remnant

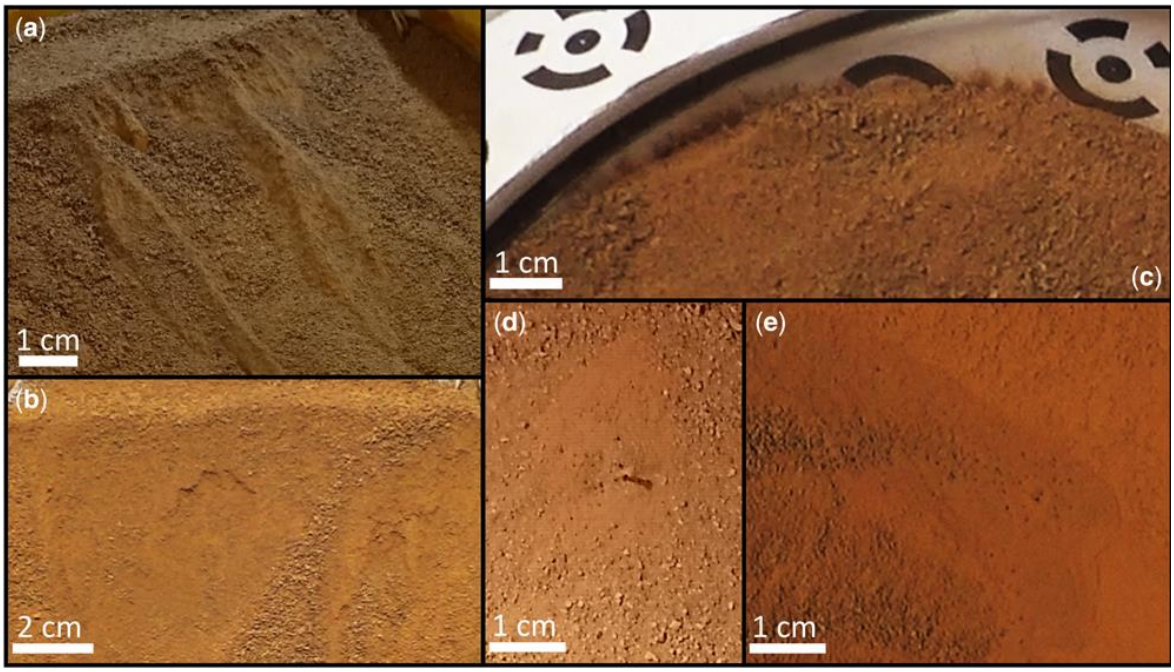


**Figure 3.6.** Resultant slope morphologies. (a) Oblique view of the crest slope zone of Run 20 (Table 3.3) displaying scarp and ridge morphology at the end of the experimental run. The clearly defined areas of failure, delimited by fresh scarps faces at the slope crest, parallel ridges to either side and debris aprons, are typical of the observed discrete sediment flows. (b) Overhead view of a small scarp which formed *c.* 2 cm below the slope crest from (run 23 Table 3.3). (c) Dust fans along back wall of box are the result of centimetre-scale jets of escaping $CO_2$ gas carrying entrained dust (from run 18 Table 3.3). (d) Pitting around the mid-slope thermocouple tree (upper-most thermocouple has been exposed at the surface), caused by escaping $CO_2$ gas (from run 15 Table 3.3). (e) Pitting at the base slope zone from run 24 (Table 3.3).

fans of dust just above the slope on the box sides (Figure 3.6c). Escaping gas also left behind relatively large areas of pitting with millimetre-scale pores, principally at the foot of the slope where surface frost was buried by deposition (Figure 3.6e), and also centred above one or both thermocouple trees (Figures 3.4a & 3.6d).

Looking at the difference raster on the right in Figure 3.7b, the greatest amount of erosion was on the right-hand side of the slope, at and below the original crestline, visible as the darker

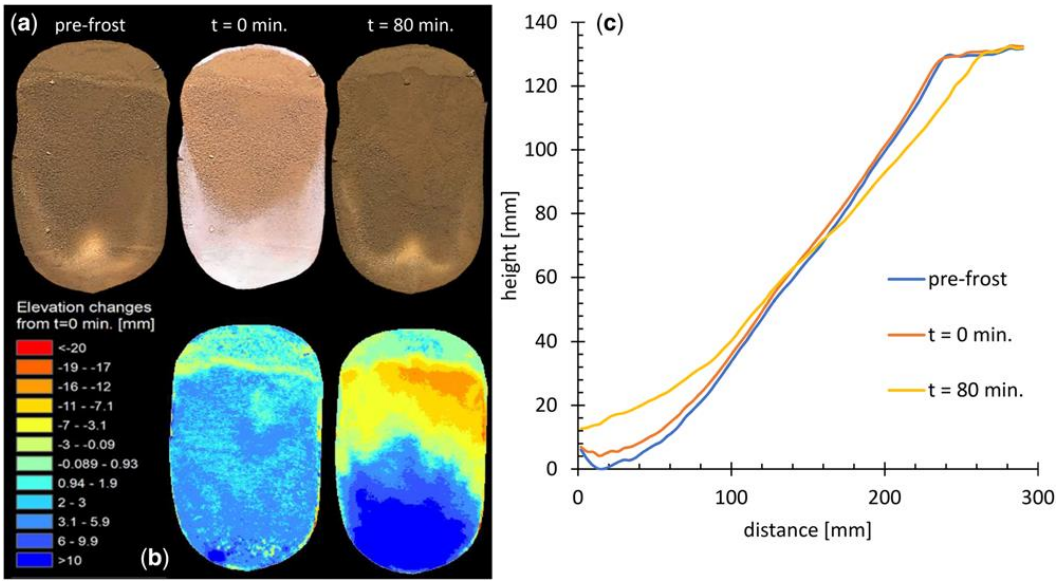


**Figure 3.7.** Slope evolution for run 20 (JSC Mars-1 at AOR): (a) orthophotos showing visible appearance of the surface prior to frost condensation, at t = 0 (the start of sublimation), t = 80 min (the end of sublimation). At t = 0, surface frost is clearly visible as a white beard on the lower half of the slope, and as a smaller, dense accumulation at the back edge of the slope, adjacent to the box. (b) Difference rasters illustrating topographic changes between the pre-frost slope and the slope at the start and end of sublimation. Red represents erosion and blue represents deposition. Both the orthophotos and the difference rasters are oriented with the slope crest at the top of each image. (c) Evolution of the topographic long profiles for the slope pre-frost, and at the start and end of sublimation. The slope zones used to measure the slope angles are indicated in Figure 3.4a.

orange region. Deposition is deepest at the base slope zone (dark blue) and extends into the mid-slope zone, relatively symmetrically along the centreline. The difference raster on the left in Figure 3.8b shows the accumulation of frost at t = 0 min, the start of sublimation. However, over the majority of the slope, the thickness of the condensed frost is on the order of the photogrammetric noise. Hence, the pattern of frost, clearly visible in the corresponding orthophoto at t = 0 min (Figure 3.7a), is not readily visible in the difference raster. The crest of the slope remains well defined and retreats, as seen in the orthophotos (Figure 3.7a) and the long profiles (Figure 3.7c). A small, arcuate alcove is clearly visible in the centre of the crest, along with lobate debris aprons downslope at t = 80 min (Figure 3.7a, b).

By way of comparison, Figure 3.8a–c illustrates the slope evolution for run 14 (JSC Mars-1 at 7.5°), the gentlest slope tested with substantial regolith movement (Table 3.2). In Figure 3.8a & c, we see that, unlike run 20 in Figure 3.7a–c, the initial slope is relatively smooth, with no break of slope at the crest, and curvature at the toe of the slope is confined to the bottom *c.* 30 mm (Figure 3.8c), v. *c.* 100 mm for run 20 (Figure 3.7c). The colour classifications

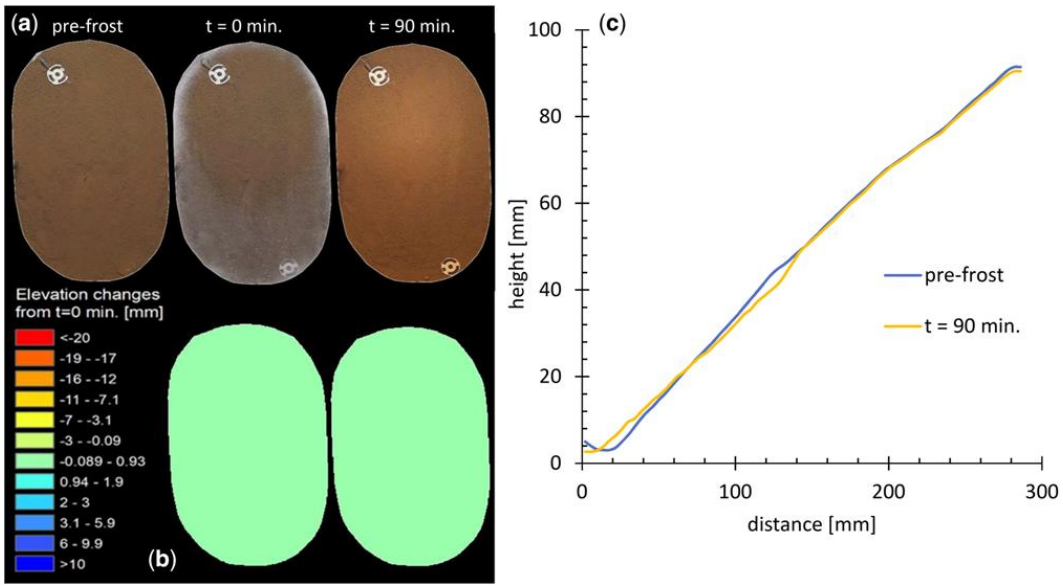


**Figure 3.8.** Slope evolution for run 14 (JSC Mars-1 at 17.5°): (a) orthophotos showing visible appearance of the surface prior to frost condensation, at t = 0 min (the start of sublimation), t = 90 min (the end of sublimation). At t = 0 min, a white beard of surface frost is clearly visible on the base slope zone, a thin (1–2 cm) concentration of frost encircling the balance of the slope along the box edges. (b) Difference rasters illustrating topographic changes between the pre-frost slope and the slope at the start and end of sublimation. The colour classifications representing elevation changes are the same as those in Figure 7. The singular classification illustrates that the scale of slope modifications was much smaller than that of run 20, in Figure 7. (c) Evolution of the topographic long profiles for the slope pre-frost, and at the start and end of sublimation. The slope zones used to measure the slope angles are indicated in Figure 4a.

representing slope elevation changes are repeated from Figure 3.7b to illustrate the relative magnitudes of slope modifications between the two runs. By comparison, all of the changes in run 14 are near the error estimates for elevation change of ±0.69 mm (Table 3.3). Although not

readily apparent in Figure 3.8a, visual observation of the video recordings confirms the location and approximate magnitude of the long profiles in Figure 3.8c. Where essentially the entire slope was modified in the steeper run 20, only the lower half of run 14 underwent substantial alteration.

#### 3.4.3.1.3 Quantitative results for JSC Mars-1

JSC Mars-1 was the most active of the three regolith types tested, undergoing the largest changes in slope elevations, volumetric displacement and the largest slope angle changes for all three slope zones (base, mid-slope and crest; Table 3.3). The maximum elevation change associated with erosion was 47 mm, with a mean of 2.3 mm; and the maximum change owing to deposition was 42 mm, with a mean of 3.0 mm (Table 3.3). The limit of detection for changes in slope height ($\Delta Z$) is 1.4 mm, based on the noise estimates described under Controls and Error Estimation. The maximum erosional volume was 374 $cm^3$, with a mean of 60 $cm^3$, and the maximum depositional volume was 482 $cm^3$, with a mean of 82 $cm^3$ (Table 3.3). The mean decrease in base slope zone angle was 4.9°, with a maximum of 15°. Both the mid-slope and crest zones had a mean decrease in slope of 1.6°, with maximum reductions of 13° and 15°, respectively (Table 3.3).

### 3.4.3.2 Fine Sand

#### 3.4.3.2.1 Fine sand sediment movement types

Fine sand transport was only detected in the three runs starting at the AOR (Table 3.4). For the first run (run 6 in Table 3.4), sediment movement was almost imperceptible. The cumulative magnitude of the minute creep observed along the retreating boundaries of surface frost was only revealed in the photogrammetric results (Table 3.3). For the second run (run 7 in

Table 3.4), slow, steady creep eventually led to a large, slope-wide discrete flow. This was the only run with fine sand that exhibited gas entrainment, which in this case was observed as bubbling of the sediment deposited atop surface frost at the toe of the slope. This event which lasted *c.* 139 s, was an immediate consequence of a discrete flow, which over-topped an accumulation of surface frost at the toe of the slope, just over halfway through the *c.* 2 h run (Table 3.4). For the third run (run 8 in Table 3.4), a single large discrete flow was accompanied by creep, which was most evident in the reshaping of the depositional fan generated by the initial, discrete flow event. For these three runs, the initial slope angle was photogrammetrically measured between 27.6° and 30.5° (Table 3.3). Discrete flows and creep were correlated with photogrammetrically determined slope angles, each between 29° and 35° (Tables 3.3 & 3.4).

#### 3.4.3.2.2 Fine sand morphology observations

Morphological changes of fine sand slopes were restricted to erosional lowering of steeper slope segments and development of depositional fans. Run 8, the most active of the fine sand runs, underwent the greatest slope angle reduction for all three slope zones (Figure 3.4a and Table 3.3). As illustrated in Figure 3.9c, roughly the top third of the long profile was eroded, while the balance of the slope accumulated the associated deposition. Both the pre-frost and t = 100 min profiles highlight the somewhat featureless character of the sand slope. The t = 100 min orthophoto in Figure 3.9a does reveal somewhat extensive depositional features over much of the slope. The t = 100 min profile, recorded along the slope centreline, fails to capture the full depth of erosion visible at the left-hand side of the crest in the difference raster (Figure 3.9b). Noting that interference of the box at the toe of the slope limits interpretation of runout features, depositional material did, in some instances, accumulate along the upslope boundary of dense

surface frost without reaching the box boundary. Subsequent sublimation of this frost left steepened lobate termini.

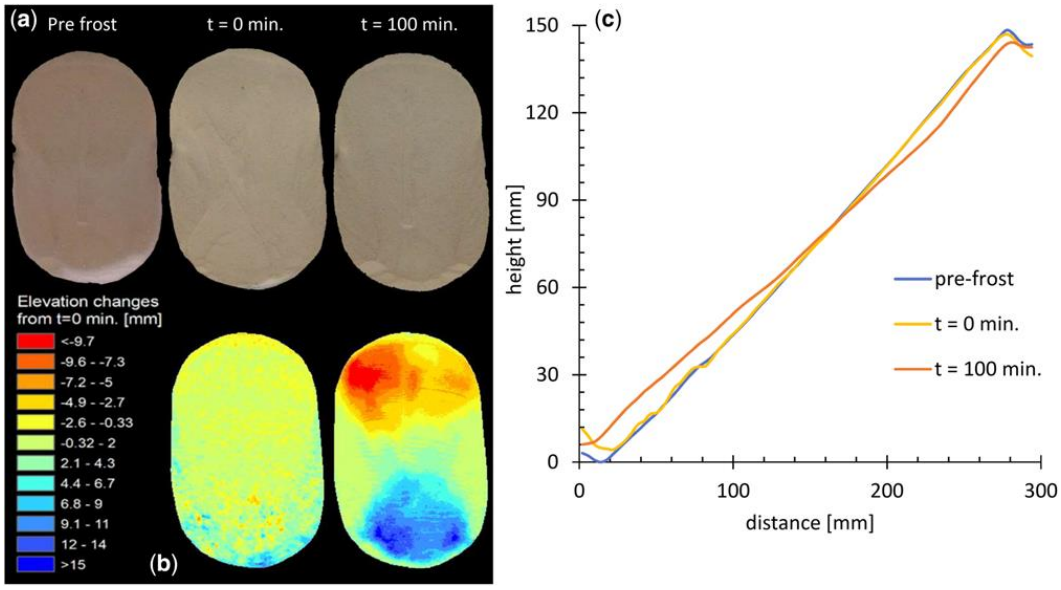


**Figure 3.9.** Slope evolution for run 8 (fine sand at AOR): (a) orthophotos showing visible appearance of the surface prior to frost condensation, at t = 0 (the start of sublimation), t = 80 min (the end of sublimation). At t = 0, surface frost is clearly visible at the toe of the slope, and faintly visible on the lower half of the slope and along the edges of the box. (b) Difference rasters illustrating topographic changes between the pre-frost slope and the slope at the start and end of sublimation. Red represents erosion and blue represents deposition. Both the orthophotos and the difference rasters are oriented with the slope crest at the top of each image. (c) Evolution of the topographic long profiles for the slope pre-frost, and at the start and end of sublimation. The slope zones used to measure the slope angles are indicated in Figure 3.4a.

In comparison with the JSC Mars-1 runs, fine sand slopes remained relatively smooth, with no sharp breaks or scarps. Fine sand did, in contrast, develop more complex depositional features, fans frequently colliding and coalescing (Figure 3.9a). Entrainment features were much less evident than for JSC Mars-1, only one entrainment event being observed.

#### 3.4.3.2.3 Fine sand quantitative results

For the three active fine sand runs (all at the angle of repose, Table 3.2), the maximum change in slope elevation associated with erosion was 12 mm, with a mean of 9.0 mm, compared with a maximum of 47 mm and mean of 10 mm for JSC Mars-1. The maximum change associated with deposition was 23 mm, with a mean of 15 mm, compared with a maximum of 42 mm and mean of 12 mm for JSC Mars-1 (Table 3.3). The fine sand slopes underwent 68.7–88.8 $cm^3$ of erosion, with a mean of 77.8 $cm^3$. Deposition was between 1.55 and 132.0 $cm^3$, with a mean of 59.8 $cm^3$ (Table 3.3). The mean change of angle for the base slope zone was −3.9°. The mid-slope and crest zones were essentially unchanged, the measured values (−1.3° and 0.5° respectively) being well within the estimated error of ±1.4° (Table 3.3). The largest slope angle changes were 4.6°, −3.4° and −5.75° for the crest, mid-slope and base regions respectively – all of these values coming from run 8 (Table 3.3).

### 3.4.3.3 Coarse sand

#### 3.4.3.3.1 Coarse sand sediment movement types

Coarse sand was the least active of the three regolith simulants tested. Only two runs, both at the AOR were conducted with coarse sand, as no appreciable sediment transport was observed. Poor camera placement prevented development of a usable photogrammetric model for run 25; however, minute surface alterations were observed, visually. In that run, a single, shallow (<2 mm deep) discrete sediment flow (*c.* 10 mm wide, 20 mm long) was observed, apparently driven downslope by a similarly small mass of surface frost which broke away from the side of the test section. Creep can be detected along the retreating edges of surface frost in the video recordings. Larger sediment grains can also be seen to roll or tumble in the video recordings.

While this activity is more easily observed than the creep, it does not appear to cause any substantial slope movement.

A single discrete slope failure was observed in run 26, over halfway through the sublimation process; in this case without the influence of frost falling from the box side. The extent of the sediment transport was comparable with that in run 25, and had a similarly limited effect on the surface morphology. As for run 25, rolling and tumbling of larger sediment grains was active throughout the duration of the run, widely distributed across the entire slope. Based on photogrammetric results, the discrete regolith flow was detected between 30° and 32°, and creep was detected at 30°.

#### 3.4.3.3.2 Coarse sand morphological and quantitative results

Only superficial morphological changes were observed for both coarse sand runs. Both runs displayed the tumbling of individual sediment grains. These grains were visually estimated to comprise <5% of all surface grains, distributed widely and uniformly across the entire slope area. These sub-centimetre-scale movements produced no discernible surface features on either of the two coarse sand slopes. Creep was visible across the mid and crest slope zones for run 25, with somewhat more evident movement along the box boundaries. Creep was less widespread in run 26 than in run 25, only apparent along the box edges and in association with the retreating edge of surface frost accumulations. For both runs, creep-induced movements were too small to produce photogrammetrically detectable surface alterations.

Coarse sand, initially at the nominal angle of repose, showed no substantial changes of elevation: on average <1 mm for the entire slope (Table 3.3), which is less than the estimated vertical photogrammetric noise of 1.2 mm (Table 3.3). The measured erosion for run 26 was 10.0

$cm^3$ (0.3% of the total regolith volume), while deposition was 32.2 $cm^3$ (0.9% of the total regolith volume) and the volume of frost was 64.8 $cm^3$ (Table 3.3). To put these volumes in context, the erosion and deposition were 0.3% and 0.9% of the total regolith volume, respectively. Remaining surface frost, visible in the final image pair for run 26, is included in the reported deposition volume. The mean change of slope angle was $-3.21 \pm 0.73°$ for the base slope zone, $-0.6 \pm 0.66°$ for the mid-slope zone and $-3.4 \pm 0.37°$ for the crest zone (Table 3.3).

## 3.5 Discussion

Sylvest et al. (2016) proposed that the observed mass-wasting behaviour of slopes of JSC Mars-1, initially at the angle of repose, was triggered by the sublimation of $CO_2$ frost condensed within the regolith pore space. They hypothesized that the rapid production of gas produced via sublimation caused the pore pressure within the sediment to increase and therefore initiated failure. In this work, we have tested two new substrate types and different initial slope angles, and we found:

(1) volumes of sediment moved by JSC Mars-1 remaining similar down to slope angles of 20° (and are slightly reduced at 17°) and volumes of sediment moving in fine sand experiments of the same magnitude, but only near the angle of repose (little movement was detected at other initial angles) and only very limited sediment transport occurring for coarse sand near the angle of repose;

(2) four different types of sediment movement, discrete flow, creep, gas entrainment and grain tumbling (creep was not reported by Sylvest et al. 2016).

In the following discussion, we integrate our experimental results into a discussion of the physics of these movements and then discuss their applicability to Mars. Our discussion focuses on the discrete and creep flows, as these cause the most sediment transport.

### 3.5.1 Mechanism and physics

In order to assess whether the mass wasting we observe in our experiments is caused by the reduction in friction angle of the sediment owing to the gas flow reducing the intergranular pressure, we consider a simple one-dimensional analytical model. The model solves continuity equations for energy and $CO_2$, and balances downslope gravitational attraction against Coulomb friction.

Suppose that the bed comprises sand with bulk density $\rho_s$, thermal conductivity $\kappa$, permeability $k$, specific heat capacity $c$ and some initial amount of $CO_2$ ice with density $\rho_i$. We assume that at $t = 0$ the bed is all at the sublimation temperature $T_s$, and then a radiant heat flux $Q$ is applied to the surface. We measure distance downwards normal to the surface using the coordinate $x$, and define the point $X(t)$ as the boundary between $CO_2$ ice and pure sand. Initially $X(0) = 0$, but over time, as heat is conducted into the bed, this point will move downwards (increasing $x$). We assume that the heat flux is due only to heat conduction between the sand grains; thus, the temperature $T(t, x)$ satisfies the equation

$$\rho_s c T_t = \kappa T_{xx}, \qquad 0 < x < X(t), \tag{1}$$

where the subscripts $t$ and $x$ are partial derivatives with respect to time and position.

The boundary conditions are

$$Q + \kappa T_x(t,0) = 0 \qquad \text{and} \qquad T(t,X) = T_s, \tag{2}$$

representing the heat flux at the surface, the temperature being at the sublimation temperature at the $CO_2$ ice interface. The movement of the point $X(t)$ is given by a differential equation that describes the heat flux driving the sublimation of the $CO_2$ ice:

$$e\rho_i \dot{X} + \kappa T_x(t,X) = 0, \tag{3}$$

where $e$ is the enthalpy of sublimation. We assume that temperature variations do not significantly affect any material properties, including the carbon dioxide gas density $\rho_g$. The behaviour of the solution is best understood by defining the following time, length and temperatures scales, $t^* = \frac{\kappa \rho_i^2 e^2}{\rho_s c Q^2}$, $x^* = \frac{\kappa \rho_i e}{\rho_s c Q}$ and $T^* = \frac{\rho_i e}{\rho_s c}$. The model is then non-dimensionalised by writing

$$X(t) = x^* f\left(\frac{t}{t^*}\right), \tag{4}$$

and

$$T(t,x) = T_s + T^* g\left(\frac{t}{t^*}, \frac{x}{x^*}\right), \tag{5}$$

where $f$ and $g$ are non-dimensional functions. The resulting non-dimensional system and an approximate analytic solution are described in Appendix B. A key point is that, for time less than the order of $t^*$, most of the heat is going into sublimating ice, and the frost front advances linearly. Conversely, for time greater than $t^*$, the energy balance changes and most of the heat goes into warming ice-free sand, the flux decaying as $1/\sqrt{t}$.

The largest gas flux, and hence highest grain mobility, occurs for short values of time. A power series solution for $f$ and $g$ can be developed in nondimensionalized time, which gives the frost point advance as

$$X(t)=x^*\left(\frac{t}{t^*}\right) - \frac{1}{2}\left(\frac{t}{t^*}\right)^2+\frac{5}{6}\left(\frac{t}{t^*}\right)^3+\ldots \quad (6)$$

Now, the mass production rate of $CO_2$ is $\rho_i\dot{X}$, and we assume that the gas density $\rho_g$ is constant and equal to the value at the sublimation temperature $T_s$ and background pressure $p_0$. The volume flux of $CO_2$ for $x < X(t)$ is therefore

$$q(t) = \frac{\rho_i}{\rho_g}\dot{X}(t) = \frac{\rho_i}{\rho_s}\frac{x^*}{t^*}f_s(s), \quad (7)$$

where the subscript s denotes the derivative. Within the bed, Darcy's law gives the stress on the sand grains as $S = \frac{\nu}{k}q(t)$. If we define the non-dimensional Darcy stress, $S^* = \frac{\nu}{k}\frac{\rho_i}{\rho_g}\frac{x^*}{t^*}\frac{1}{\rho_s g} = \frac{\nu Q}{ke\rho_g\rho_s g}$, then $S = \rho_s g S^* f_s$, $S$ being the reduction in normal stress due to the gas flow. As the maximum shear stress that can be supported by the grains is proportional to the normal stress between the grains, this reduction increases the probability of failure. The Coulomb failure criterion is independent of depth, and after dividing by $x\rho_s g$, at any point $s < X(t)$, it is

$$\sin\theta = \mu[\cos\theta - S^* f_s], \quad (8)$$

where $\mu$ is the coefficient of friction and $\theta$ is the slope angle. Thus, it can be seen that $S^*$ is the key non-dimensional group that determines whether the bed is likely to mobilize, and that this does not depend on the concentration of ice. The ice concentration will, however, determine how long mobilization will occur, owing to the dependence on $t^*$. For short times ($t < t^*$), $f_s = 1$; hence, the $CO_2$ flux can initially be calculated by assuming that all the radiant heat is subliming $CO_2$ ice.

Solving equation (8) for $\theta$, using the parameters for the experimental conditions, gives the new, reduced internal friction angle for the slope under those conditions. This can be solved exactly, but an approximate formula, for small $q$, is more convenient:

$$\tan\theta = \mu\left[1 - \sqrt{1+\mu^2}\, S^*\, f_s\right]. \tag{9}$$

The input experimental parameters are listed in Table B1. If the model provides an accurate description of the physics, then we would expect that the reduction in friction angle corresponds to the initial slopes at which we observe movement in our experiments. Note however, that there is considerable (as much as 5°) stochastic variation in the failure angle of granular materials.

The results of applying our analytical model to our experimental data are presented in Table 3.5. Because coarse sand shows no significant transport, even at the angle of repose, this substrate is expected to have the lowest reduction in friction angle. Conversely, because JSC Mars-1 transports substantial volumes of sediment on slopes down to 17° (Table 3.3), it is expected to undergo the highest reduction in friction angle. Fine sand should therefore be intermediate, between the other two sediments, as it only shows substantial volume transport

near the angle of repose. The different substrates do have the expected relative reductions in friction angle predicted by the model (Table 3.5). The reduction in friction angles for coarse and fine sand under terrestrial gravity (0.5° and 1.9° respectively, Table 3.5) match our experimental results, whereby no appreciable movement is seen for coarse sand, and appreciable movement is only observed near the angle of repose for fine sand. We note that the finer grain fraction in the coarse sand did show some signs of mobilization; however, we infer that the presence of larger grains both impeded mass movement and also increased the substrate permeability, preventing the build-up of pressure within the pore space. For JSC Mars-1, we get a slightly larger change of internal friction angle than expected, of 17.6°. Based on our experimental results, this would imply activity in the 15° experiments, which was not observed. However, unlike fine and coarse sand, we did not make our own independent measurements of the permeability for the JSC Mars-1 material (Sizemore & Mellon 2008), and slight variations can change the outcome of the calculation. Equally, our measurements indicated that the bulk density of the JSC Mars-1 could vary by ±0.07 g $cm^{-3}$, even with similar preparation, which could also contribute to this discrepancy. The volume flux velocity for our experiments was based on the rate of sublimation dictated by the supplied radiant heat and thermodynamic properties of the $CO_2$. As these parameters were held constant for all runs, the volume flux velocity was also constant, at 0.012 m $s^{-1}$ (Table 3.5).

The scale time, $t^*$, is the cross-over time, when radiant heat input transitions from primarily sublimating $CO_2$ frost to primarily heating the regolith. In practice, $t^*$ is neither readily observed nor measured, but we might expect it to have the same order of magnitude as the duration of the phase change. Example experimental temperature traces over the duration of

sublimation for fine sand and JSC Mars-1, both initially near the angle of repose, are presented in Figure 3.10a& b.

The longer scale time ($t^*$) output from our analytical model for JSC Mars-1 might be expected to be evidenced by a delayed start of regolith temperature increase, relative to fine sand. Neither of these predictions is borne out in the temperature data. In Figure 3.10a for fine sand, initially, the deepest parts of the slope begin to warm with the cessation of active cooling and the upper regions continue to cool. Each trace, roughly in order of increasing depth, warms to the sublimation temperature (*c.* −120°C), where it remains constant during sublimation of the condensed frost before continuing to warm. The phase change dominates the temperature curves for hours, v. the <2 min suggested by $t^*$ in our analytical model (Table 3.5). In contrast to fine sand, the behaviour of JSC Mars-1 is different (Figure 3.10b). In this case, all six temperature traces are essentially constant at the onset of the sublimation process, followed by a steady increase. None of the JSC Mars-1 traces displays a plateau suggesting active frost sublimation, hence we cannot compare these data with the sublimation times of the fine sand runs, nor with the predicted $t^*$ values from our analytical results.

An additional complication for understanding the experiments is the complicated geometry and initial conditions. As shown in Figure 3.10, the initial temperature profile is far from uniform, and the entire bed is not at the sublimation temperature as was assumed in the analytical model. To investigate this further, we numerically solved the one-dimensional heat conduction equation with sublimation. We assumed zero heat flux on the lower boundary, and the same radiant heat flux used in the analytical model on the upper boundary (350 W $m^{-2}$, Table 3.5). The frost load was estimated to be 20 kg $m^{-3}$. We attempted a simple match of the initial

temperature profile to the thermocouple readings. The results can be seen in Figure 3.10, along with the experimental traces. We see reasonable agreement between the experimental and

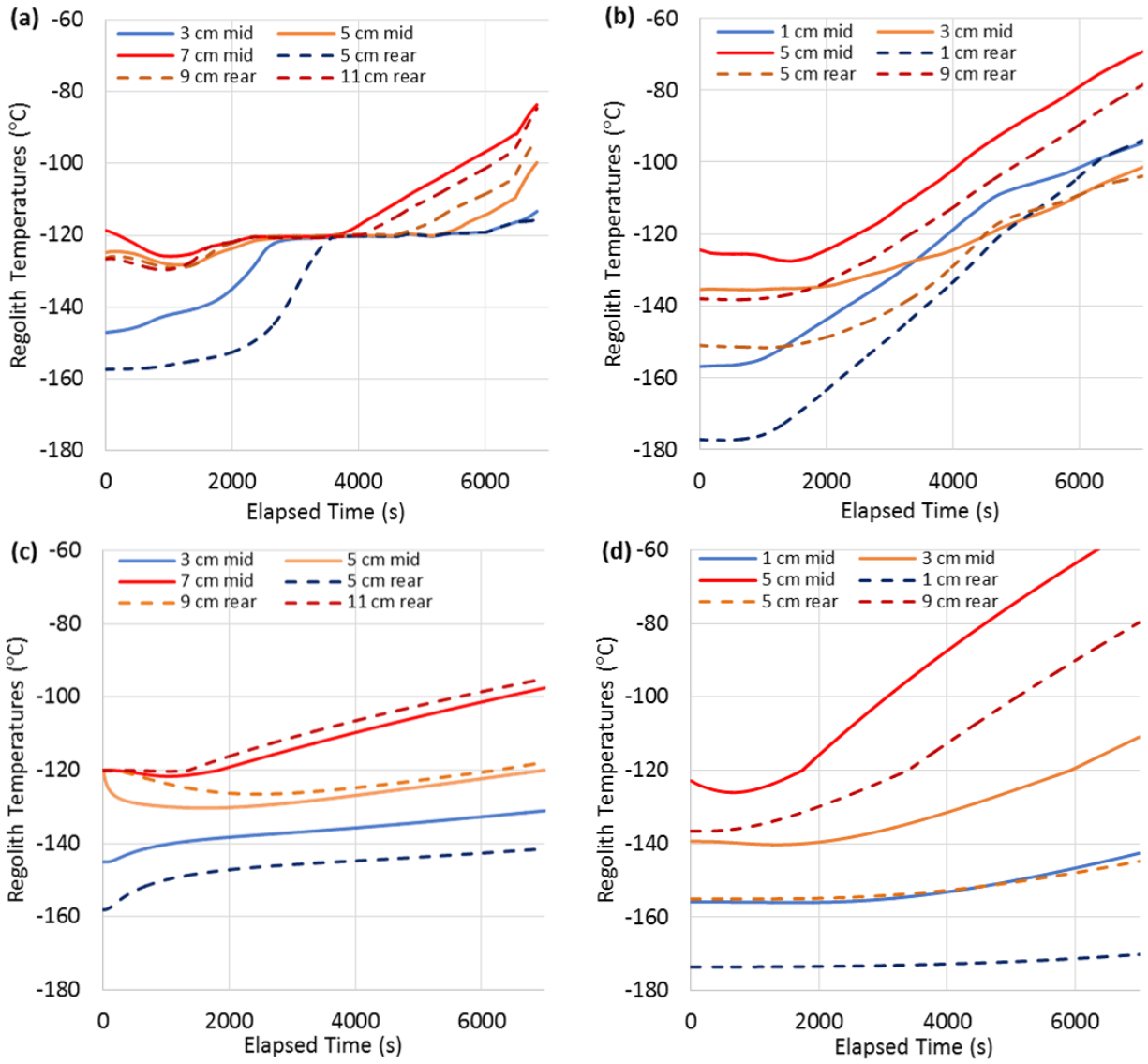


**Figure 3.10.** Experimental and modelled temperature traces during sublimation. (a) Run 8 (fine sand at AOR). (b) Run 23 (JSC Mars-1 at AOR). (c) and (d) Simulations of the one-dimensional heat conduction equation with sublimation for fine sand and JSC Mars-1, respectively. Thermocouple locations are indicated in Figure 3.4a. Vertical positions are in centimetres above the bottom of the box. Solid lines correspond to mid-slope thermocouples; dashed rear. Blue traces correspond to the deepest locations; red traces are the closest to the slope surface and orange are in-between.

numerical traces for JSC Mars-1 (Figure 3.10b, d). The traces for fine sand (Figure 3.10a, c) do not match, which suggests that, although the theory is reasonable, the uncertainties in the initial and boundary conditions substantially affect the energy budget, and thus the sublimation rate.

These null results highlight that the predictive power of these physical models is limited by the quality of the measured parameters, particularly the regolith properties. Thermal conductivity, for example, can vary by an order of magnitude depending on how the regolith was handled during preparation of the slope. JSC Mars-1 provides particularly difficult challenges for modelling, owing to the increased influence of inter-particle interactions compared with even fine sand. However, even with these caveats, we are able to obtain results which capture certain aspects of our experimental results, and that provide a better understanding of the basic physical mechanisms driving the sediment transport in our experiments. This then allows us to transfer our results to Mars, which we present in the following section.

### 3.5.2 Application to Mars

One of the underlying assumptions in the analytical models outlined above was that $CO_2$ ice is emplaced below or within the sediment, in order for sediment transport to occur. This reflects a key observation from both the experiments reported here and in Sylvest et al. (2016): sediment transport is only triggered where $CO_2$ frost is in the subsurface, and not where it has accumulated on the surface. Reporting of $CO_2$ ice on Mars is limited to surface observations of frost and/or slab ice (e.g. Gardin et al. 2010; Appéré et al. 2011; Piqueux et al. 2015). However, when surface $CO_2$ is not present, trapping of $CO_2$ ice within the regolith should be possible, as has been previously formulated for the emplacement of water ice in the subsurface (e.g. Mellon et al. 1993). Assuming Mars' regolith is dry, the atmosphere can diffuse into the subsurface pore

space. The surface of Mars undergoes a diurnal and annual temperature cycle, and therefore the physical processes described in 'Mechanism and physics' section could take place repeatedly on time and depth scales concurrent with diurnal, annual and secular temperature variations. As the surface temperature variation propagates into the regolith, it experiences a lagging and damping effect (for illustration, see Hagermann 2005). This means that there are periods in the subsurface thermal cycle when the temperature wave decreases to below the sublimation point of $CO_2$ such that the $CO_2$ sublimation horizon moves upwards. As atmospheric $CO_2$ diffuses into the soil, subsurface $CO_2$ deposition occurs. At low pressures, this is best described as molecules following the vapour pressure gradient until they are deposited as ice at depth. Our experiments reveal that the nature of the $CO_2$ frost, and exactly where it ends up on or in the slope, should control the type and quantity of sediment transport owing to subsequent sublimation of the frost.

Although beyond the scope of the current study, temperature gradients through the depth of the slope, during the condensation phase of the experiments, are expected to control the depth of subsurface frost formation, and possibly the density of both subsurface and surface frost. Our analytical models demonstrate that these are key factors in determining whether sediment transport will occur.

Given these arguments, we believe that the emplacement of $CO_2$ into the regolith pore-space should be possible on Mars, and therefore, we have applied our simple analytical model above using Martian gravity instead of terrestrial (Table 3.4). This reveals that the reduction in friction angle should be even greater on Mars for any given substrate, compared with the reductions observed on Earth. Hence, these results should be applicable to a larger range of slopes for any given substrate than expected, based on our laboratory results without scaling. The

calculations under Martian gravity suggest that movements in fine sand should be observable on slopes as much as 5° lower than the nominal angle of repose.

In summary, our results predict that mass wasting (creep and discrete granular flows) can be triggered by the sublimation of $CO_2$ frost on Mars, where temperatures in the near-surface regolith dip below the condensation temperature of $CO_2$, and where $CO_2$ surface frost or ice is not present at the surface when the sediment transport occurs. Our experiments do not allow us to directly compare morphologies observed on the Martian surface with morphologies observed in our experiments owing to the difference in scale. However, from our results we can infer likely locations on Mars where this process could occur by examining regions which have similar slopes and grainsizes to those found to be active in our experiments. Many of the present-day sediment transport events associated with Martian gullies fall into this category. Notable exceptions include: (1) polar pit gullies at 68° S, where Raack et al. (2015) noted that the recent dark flows occurred in the spring, when the surface is still covered with $CO_2$ ice; (2) activity in large apron gullies on sand dunes between 40° S and 60° S, which occur in winter, when $CO_2$ frost is still present (Diniega et al. 2010; Pasquon et al., this volume, in review); and (3) mass wasting events on north polar dunes, that are active in the mid-winter, under the $CO_2$ ice slab (which although not strictly gullies, could represent processes active in gullies; Diniega et al. 2017). These three exceptions represent a small proportion of known active gullies. The remaining active gully sites comprise ‘classic’, mid-latitude gullies and linear dune gullies (Auld & Dixon 2016; Conway et al. 2017). As reported in Vincendon (2015) and Dundas et al. (2017), activity in mid-latitude classic gullies is limited to periods when thin (microns to centimetres) and patchy $CO_2$ or H2O frost is present during, or just prior to the noted activity. So far, *c.* 67 such sites have been catalogued as active (Dundas et al. 2017), which is *c.* 18% of monitored

sites in the southern hemisphere, but activity is sporadic, rather than annual. As reported in Reiss & Jaumann (2003), Reiss et al. (2010), Pasquon et al. (2016; this volume, in review and Jouannic et al. (this volume, in review), activity in linear dune gullies happens when the last $CO_2$ ice is disappearing from the pole-facing crest of the dune. Linear dune gullies are particularly active, with most of the 33 sites showing annual changes. Hence, in terms of timing and frost observations for both active 'classic' gullies and active linear gullies, the mechanism we have observed in the laboratory could be at work.

We re-emphasize here that our experiments cannot tell us what role sublimation of subsurface $CO_2$ frost is playing in forming the morphologies of these gully types, and we note that it may only be a secondary process (see further discussion on this point below). However, we think it should be considered among the candidates for morphological changes in these gullies for the following reasons. The substrate type is better known for linear dune gullies than for classic gullies. Sand dunes on Mars have been investigated *in situ* by rovers, the most recent study revealing grains ranging between 50 and 350 μm with a mean size of 113 μm (Ewing et al. 2017). Activity in linear gullies is only found where the crest of the dune is at 20° or higher, but the changes themselves occur on slopes down to 5–10° (Pasquon et al. 2016; Jouannic et al., this volume, in review). Both the substrate type and slope angles used in our experiments are consistent with these data, hence our results would predict movement in this context if $CO_2$ is condensed in to the subsurface. For classic gullies, we must rely on orbital observations, with thermal inertia measurements suggesting that gullies reside in materials classed as unconsolidated 'sand- to pebble-sized grains' (Reiss et al. 2009; Harrison et al. 2014). Source areas for recent motions in classic gullies are usually diffuse, suggesting remobilization of a loose surface cover (Dundas et al. 2017) and source areas of classic gullies range upwards from

20° (median 25°; Conway et al. 2015). Results from our laboratory work and application of our analytical model reveal that these grain sizes and slope angles should be able to sustain the $CO_2$ sublimation-triggered failures that we have investigated in our experiments.

The range of sediments that could be mobilized on Mars could be wider than that encompassed by the fine sand and JSC Mars-1 sediments used in our laboratory work. Our results indicate that the fine component of the sediment plays an important role in triggering activity at angles lower than the angle of repose. On Mars, dust (generally accepted as grains with >30 μm diameter) is abundant on the surface and in the atmosphere (e.g. Christensen 1986; Tomasko et al. 1999). However, further experiments would be required to assess how important this factor might be in triggering movement.

We also consider it possible that the mechanism of $CO_2$ sublimation-triggered failures we observed in the laboratory could also have occurred under climate conditions different from those observed on Mars today, which may explain some of the sediment transport that has contributed to gully formation on timescales of millions of years (Reiss et al. 2004; Schon et al. 2009; de Haas et al. 2015a). However, further modelling work to understand the plausible temporal and spatial extent of this process at the present day would be needed in order to confidently extrapolate this process into the past, an endeavour beyond the scope of this present work.

Our experiments investigated the triggering of failures of unconsolidated materials, and we observed two models of subsequent transport, granular flow and creep. A subtype of recent gully activity termed ‘bright flows’ has been found to have a morphology consistent with a classic granular flow (Pelletier et al. 2008; Kolb et al. 2010). However, other features of recent

(and past) activity, including the transport of metre-scale boulders, the formation of levees and lobate termini (e.g. Dundas et al. 2010, 2014, 2017; Johnsson et al. 2014; de Haas et al. 2015b) require some viscosity or fluidization of the flow beyond that of a simple granular flow. Further, in linear gullies the new morphologies are complex, encompassing albedo changes, formation of pits, channels with levees and complex distributary networks on relatively low slopes (Diniega et al. 2013; Pasquon et al. 2016; this volume, in review; McKeown et al. 2017; Jouannic et al., this volume, in review). As discussed by Stewart & Nimmo (2002), $CO_2$ gas should dissipate too quickly to enable durable fluidization of a sublimation-triggered flow. However, the fluidization of $CO_2$ sublimation-triggered granular flows has not yet been studied in the laboratory and should therefore be a focus of future work in order to substantiate these calculations. Our observations that $CO_2$ sublimation can generate a creep-like movement in unconsolidated sediments is of particular relevance to Mars, because it could provide an explanation for lobate features (Gallagher & Balme 2011; Gallagher et al. 2011; Johnsson et al. 2012; Balme et al. 2013; Soare et al. 2016), which are often associated with Martian gullies. The closest terrestrial analogue for these features is solifluction lobes, which are uniquely associated with creep generated by freeze–thaw cycling of water in the ground, so our results provide a possible alternative that needs to be explored further.

Our laboratory work results only pertain to sediment transport of unconsolidated materials. The present-day observations of activity in classic gullies seem to only encompass the transport of unconsolidated sediments, as outlined above. However, these landforms, which have been dated to millions of years (Reiss et al. 2004; Schon et al. 2009; Johnsson et al. 2014), are incised into consolidated materials including both the ice-rich Latitude Dependent Mantle and bedrock (e.g. Dickson et al. 2015; de Haas et al. 2017). Erosion of the unconsolidated

sublimation lag believed to be on top of the LDM should engender loss of the interstitial ice by sublimation, rendering further sediment available for transport (e.g. Pilorget & Forget 2016). However, for gully alcoves cut into bedrock, it remains an open question as to how material is weathered to render it transportable. It should be acknowledged that whether this is a primary feature of the gully-forming process is under debate (cf. de Haas et al. 2015a; Dickson et al. 2015). The relationship between this weathering and the action of $CO_2$ condensation–sublimation cycles is an area for future work.

### 3.6 Conclusions

We have experimentally investigated the effect of sublimating $CO_2$ on the downslope mass wasting of sediment under Martian atmospheric conditions. We tested three substrate types, fine sand (mean diameter 168 μm), coarse sand (mean diameter 594 μm) and a Mars regolith simulant (JSC Mars-1) over slope angles ranging from 10° to near the angle of repose, adding to the work of Sylvest et al. (2016), which only considered JSC Mars-1 near the angle of repose. We observed four principal movement types: discrete flows, creep, gas entrainment and grain tumbling. Of these, creep and grain tumbling were not reported in Sylvest et al. (2016). The observed sediment movement types were influenced both by initial slope angle and by the nature of the regolith.

We found that significant volumes of sediment were only transported by the discrete flows and creep movements. In fine sand, these processes were only active at slope angles near the angle of repose and the volumes transported were of the same order as those transported in experiments using JSC Mars-1 at the angle of repose (82 $cm^3$ mean erosion for a surface area of 473 $cm^2$). For JSC Mars-1, these processes continued to transport equivalent volumes of

sediment down to 20°, slightly less at 17° and negligible amounts at slope angles <17°. In our previous work we hypothesized that mass wasting was triggered by a lowering of the static friction angle by gas escaping through the substrate from sublimation. We tested this hypothesis by constructing an analytical model describing the physics of this process and found that when applied to our experimental parameters this model successfully predicts the activity observed in our experiments. With this validated model, we were able to predict that, under Martian gravity for equivalent sediment types, mass wasting could be triggered at even lower slope angles (movement should be possible for coarse sand near angle of repose, 25° for fine sand and on any slope for JSC Mars-1). This model also reveals that the reduction in permeability in the JSC Mars-1 owing to the presence of fines could be the key parameter for explaining this substrate's enhanced activity range compared with the two sands. Our results suggest that the absolute amount of $CO_2$ in the subsurface may control the amount of sediment moved. Further the vertical temperature profiles from our experiments reveal that $CO_2$ ice emplacement in the subsurface, in terms of vertical distribution and density, is a key parameter to elucidate in order to better understand the limits of sediment transport by $CO_2$ sublimation.

On Mars, we find that the $CO_2$ sublimation-triggered mass movements observed in our experiments could be applicable for explaining some of the movements seen in present-day mid-latitude gullies and linear dune gullies. Specifically, our experiments and analytical model reveal that the grain sizes and slopes should be compatible with this type of motion. Some of the features, including movements of metre-scale boulders, levees and lobate termini, are features that would require further experimentation to determine if $CO_2$ sublimation can explain them. Finally, we present the first observations of a creep-like motion caused by $CO_2$ sublimation and

this could provide a viable alternative to water–ice freeze–thaw cycles to explain the origin of lobate features often found in association with Martian gullies.

## 3.7 References


Allen, C.C., Morris, R.V., Karen, M.J., Golden, D.C., Lindstrom, M.M., Lockwood, J.P. (1998), Martian Regolith Simulant JSC Mars-1, in *Lunar and planetary science conference XXVIII*, p. 1690.

Appéré, T., Schmitt, B. Langevin, Y., Douté, S., Pommerol, A., Forget, F., Spiga, A., Gondet, B., Bibring, J. 2011. Winter and spring evolution of northern seasonal deposits on Mars from OMEGA on Mars Express. Journal of *Geophysical Research: Planets*, 116(E5). https://doi.org/10.1029/2010JE003762.

Auld, K.S. & Dixon, J.C., 2016. A classification of martian gullies from HiRISE imagery. *Planetatry and Space Science*, 131, 88–101. https://doi.org/10.1016/j.pss.2016.08.002.

Balme, M.R., Gallagher, C.J. & Hauber, E. 2013. Morphological evidence for geologically young thaw of ice on Mars: a review of recent studies using high-resolution imaging data. *Progress in Physical Geography*, 37(3), 289–324. https://doi.org/10.1177/0309133313477123.

Bargery, A.S., Balme, M.R., Warner, N., Gallagher, C.J. & Gupta, S. 2011. A background to Mars exploration and research. *In*: Balme, M.R., Bargery, A.S., Gallagher, C.J. & Gupta, S. (eds) *Martian Geomorphology*. Geological Society, London, Special Publications, 356, 5–20. https://doi.org/10.1144/SP356.2

Cedillo-Flores, Y., Treiman, A.H., Lasue, J., Clifford, S.M. (2011), $CO_2$ gas fluidization in the initiation and formation of Martian polar gullies, *Geophysical Research Letters*, 38(21). https://doi.org/10.1029/2011GL049403.

Christensen, P.R. 1986. Regional dust deposits on Mars: physical properties, age, and history. *Journal of Geophysical Research*, 91(B3), pp.3533–3545. https://doi.org/10.1029/JB091iB03p03533.

Coleman, K.A., Dixon, J.C., Howe, K.L., Roe, L.A. & Chevrier, V. 2009. Experimental simulation of Martian gully forms. *Planetary and Space Science*, 57(5), pp.711–716. https://doi.org/10.1016/j.pss.2008.11.002.

Conway, S.J., Lamb, M.P., Balme, M.R., Towner, M.C., Murray, J.B., 2011a. Enhanced runout and erosion by overland flow at low pressure and sub-freezing conditions: Experiments and application to Mars. *Icarus*, 211, 443–457. https://doi.org/10.1016/j.icarus.2010.08.026.

Conway, S.J., Balme, M.R., Murray, J.B., Towner, M.C., Okubo, C.H. & Grindrod, P.M. 2011b. The indication of Martian gully formation processes by slope-area analysis. *In*: Balme, M.R., Bargery, A.S., Gallagher, C.J. & Gupta, S. (eds) *Martian Geomorphology*. Geological

Society, London, Special Publications, 356, 5–20. https://doi.org/10.1144/SP356.10.

Conway, S.J., Balme, M.R., Kreslavsky, M.A., Murray, J.B. & Towner, M.C. 2015. The comparison of topographic long profiles of gullies on Earth to gullies on Mars: a signal of water on Mars. *Icarus*, 253, 189–204. https://doi.org/10.1016/j.icarus.2015.03.009.

Conway, S.J., Harrison, T.N., Soare, R.J., Britton, A.W., Steele, L.J., 2017. New slope-normalized global gully density and orientation maps for Mars. *In*: Conway, S.J., Carrivick, J.L., Carling, P.A., de Haas, T. & Harrison, T.N. (eds) *Martian Gullies and their Earth Analogues.* Geological Society, London, Special Publications, 467. https://doi.org/10.1144/SP467.3.

de Haas, T., Conway, S.J. & Krautblatter, M. 2015a. Recent (Late Amazonian) enhanced backweathering rates on Mars: paracratering evidence from gully alcoves. *Journal of Geophysical Research: Planets*, 120(12), 2169–2189. https://doi.org/10.1002/2015JE004915.

de Haas, T., Ventra, D., Hauber, E., Conway, S.J. & Kleinhans, M.G. 2015b. Sedimentological analyses of Martian gullies: The subsurface as the key to the surface. *Icarus*, 258, 92–108. https://doi.org/10.1016/j.icarus.2015.06.017.

de Haas, T., Conway, S.J., Butcher, F.E.G., Levy, J., Grindrod, P.M., Goudge, T.A. & Balme, M.R. 2017. Time will tell: temporal evolution of Martian gullies and paleoclimatic implications. *In*: Conway, S.J., Carrivick, J.L., Carling, P.A., de Haas, T. & Harrison, T.N. (eds) *Martian Gullies and their Earth Analogues.* Geological Society, London, Special Publications, 467. https://doi.org/10.1144/SP467.1.

Dickson, J.L., Head, J.W., Kreslavsky, M. 2007. Martian gullies in the southern mid-latitudes of Mars: evidence for climate-controlled formation of young fluvial features based upon local and global topography. *Icarus*, 188(2), pp.315–323. https://doi.org/10.1016/j.icarus.2006.11.020.

Dickson, J.L., Head, J.W., Goudge, T.A., Barbieri, L. 2015. Recent climate cycles on Mars: stratigraphic relationships between multiple generations of gullies and the latitude dependent mantle. *Icarus*, 252, pp.83–94. https://doi.org/10.1016/j.icarus.2014.12.035.

Diniega, S., Byrne, S., Bridges, N.T., Dundas, C.M., McEwen, A.S., 2010 Seasonality of present-day Martian dune-gully activity. *Geology*, 38(11), pp.1047–1050. https://doi.org/10.1130/G31287.1.

Diniega, S., Hansen, C.J., McElwaine, J.N., Hugenholtz, C.H., Dundas, C.M., McEwen, A. S., Bourke, M.C., 2013. A new dry hypothesis for the formation of martian linear gullies. *Icarus*, 225(1), pp.526–537. https://doi.org/10.1016/j.icarus.2013.04.006.

Diniega, S., Hansen, C.J., Allen, A., Grigsby, N., Li, Z., Perez, T. & Chojnacki, M. 2017. Dune-slope activity due to frost and wind throughout the north polar erg, Mars. *In*: Conway, S.J., Carrivick, J.L., Carling, P.A., de Haas, T. & Harrison, T.N. (eds) *Martian Gullies and their Earth Analogues.* Geological Society, London, Special Publications, 467.

https://doi.org/10.1144/SP467.6.

Dundas, C.M., McEwen, A.S., Diniega, S., Byrne, S., Martinez-Alonso, S., Alonso, S.M., Martinez-Alonso, S., 2010. New and recent gully activity on Mars as seen by HiRISE. *Geophysical Research Letters*, 37(7). https://doi.org/10.1029/2009GL041351.

Dundas, C.M., Diniega, S., Hansen, C.J., Byrne, S., McEwen, A.S., 2012. Seasonal activity and morphological changes in martian gullies. *Icarus*, 220(1), pp.124–143. https://doi.org/10.1016/j.icarus.2012.04.005.

Dundas, C.M., Diniega, S., McEwen, A.S., 2015. Long-term monitoring of martian gully formation and evolution with MRO/HiRISE. *Icarus*, 251, pp.244–263. https://doi.org/10.1016/j.icarus.2014.05.013.

Dundas, C.M., McEwen, A.S., Diniega, S., Hansen, C.J., Byrne, S., McElwaine, J.N., 2017. The formation of gullies on Mars today. *In*: Conway, S.J., Carrivick, J.L., Carling, P.A., de Haas, T. & Harrison, T.N. (eds) *Martian Gullies and their Earth Analogues.* Geological Society, London, Special Publications, 467. https://doi.org/10.1144/SP467.5

Ewing, R.C., Lapotre, M.G.A. Et Al. 2017. Sedimentary processes of the Bagnold Dunes: implications for the eolian rock record of Mars. *Journal of Geophysical Research: Planets*, 122(12), pp.2544-2573. https://doi.org/10.1002/2017JE005324.

Gallagher, C.J. & Balme, M.R. 2011. Landforms indicative of ground-ice thaw in the northern high latitudes of Mars. *In*: Balme, M.R., Bargery, A.S., Gallagher, C.J. & Gupta, S. (eds) *Martian Geomorphology*. Geological Society, London, Special Publications, 356, pp.87–110. https://doi.org/10.1144/SP356.6.

Gallagher, C., Balme, M.R., Conway, S.J., Grindrod, P.M. 2011. Sorted clastic stripes, lobes and associated gullies in high-latitude craters on Mars: landforms indicative of very recent, polycyclic ground-ice thaw and liquid flows. *Icarus*, 211(1), pp.458–471. https://doi.org/10.1016/j.icarus.2010.09.010.

Gardin, E., Allemand, P., Quantin, C., Thollot, P., 2010. Defrosting, dark flow features, and dune activity on Mars: Example in Russell crater. *Journal of Geophysical Research: Planets*, 115(E6). https://doi.org/10.1029/2009JE003515.

Goodman, T.R. 1958. The heat-balance integral and its application to problems involving a change of phase. *Transactions of the ASME Journal*, 80, 335–342.

Hagermann, A. 2005. Planetary heat flow measurements. *Philosophical Transactions of the Royal Society: A. Mathematical, Physical and Engineering Science*, 363, pp.2777–2791. https://doi.org/10.1098/rsta.2005.1664.

Hansen, C.J., Bourke, M., Bridges, N.T., Byrne, S., Colon, C., Diniega, S., Dundas, C., Herkenhoff, K., McEwen, A., Mellon, M., Portyankina, G., Thomas, N., 2011. Seasonal Erosion and Restoration of Mars' Northern Polar Dunes. *Science (New York, N.Y.)*, 331(6017), pp.575–578. https://doi.org/10.1126/science.1197636.

Harrison, T.N., Osinski, G.R., Tornabene, L.L., Jones, E., 2015. Global Documentation of Gullies With the Mars Reconnaissance Orbiter Context Camera and Implications for Their Formation. *Icarus*, 252, pp.236-254. https://doi.org/http://dx.doi.org/10.1016/j.icarus.2015.01.022.

Hess, S.L., Henry, R.M., Tillman, J.E., 1979. The seasonal variation of atmospheric pressure on Mars as affected by the south polar cap. *Journal of Geophysical Research: Solid Earth*, 84(B6), pp.2923–2927. https://doi.org/10.1029/JB084iB06p02923.

Hess, S.L., Ryan, J.A., Tillman, J.E., Henry, R.M. & Leovy, C.B. 1980. The annual cycle of pressure on Mars measured by Viking Landers 1 and 2. *Geophysical Research Letters*, 7(3), pp.197–200. https://doi.org/10.1029/GL007i003p00197.

Johnsson, A., Reiss, D., Hauber, E., Zanetti, M., Hiesinger, H., Johansson, L. & Olvmo, M. 2012. Periglacial mass-wasting landforms on Mars suggestive of transient liquid water in the recent past: insights from solifluction lobes on Svalbard. *Icarus*, 218(1), 489–505. https://doi.org/10.1016/j.icarus.2011.12.021.

Johnsson, A., Reiss, D., Hauber, E., Hiesinger, H. & Zanetti, M. 2014. Evidence for very recent melt-water and debris flow activity in gullies in a young midlatitude crater on Mars. *Icarus*, 235, pp.37–54. https://doi.org/10.1016/j.icarus.2014.03.005.

Jouannic, G., Gargani, J., Conway, S.J., Costard, F., Balme, M.R., Patel, M.R., Massé, M., Marmo, C., Jomelli, V., Ori, G.G., 2015. Laboratory simulation of debris flows over sand dunes: Insights into gully-formation (Mars). *Geomorphology*, 231, pp.101–115. https://doi.org/10.1016/j.geomorph.2014.12.007.

Jouannic G., Gargani J., Costard F., Massé M., Bourgeois O., Conway S.J., Carter J., Schmidt F, Marmo C, Ori G.G., Nachon M., Pasquon K., 2018. Morphological characterization of landforms produced by springtime seasonal activity on Russell dune (Mars). , *In*: Conway, S.J., Carrivick, J.L., Carling, P.A., de Haas, T. & Harrison, T.N. (eds) *Martian Gullies and their Earth Analogues.* Geological Society, London, Special Publications, SP467.

Kolb, K.J., Pelletier, J.D. & McEwen, A.S. 2010. Modeling the formation of bright slope deposits associated with gullies in Hale Crater, Mars: implications for recent liquid water. *Icarus*, 205(1), pp.113–137. https://doi.org/10.1016/j.icarus.2009.09.009.

Malin, M.C., Edgett, K.S., 2000. Evidence for Recent Groundwater Seepage and Surface Runoff on Mars. *Science*, 288(5475), pp.2330–2335. https://doi.org/10.1126/science.288.5475.2330.

McEwen, A.S., Ojha, L., Dundas, C.M., Mattson, S.S., Byrne, S., Wray, J.J., Cull, S.C., Murchie, S.L., Thomas, N., Gulick, V.C., 2011. Seasonal flows on warm Martian slopes. *Science (New York, N.Y.)*, 333(6043), pp.740–743. https://doi.org/10.1126/science.1204816.

McGlynn, I.O., Fedo, C.M. & McSween, H.Y. 2011. Origin of basaltic soils at Gusev crater, Mars, by aeolian modification of impact-generated sediment. *Journal of Geophysical Research: Planets*, 116(E7). https://doi.org/10.1029/2010JE003712.

Mc Keown, L.E., Bourke, M.C., McElwaine, J.N., 2017. Experiments On Sublimating Carbon Dioxide Ice And Implications For Contemporary Surface Processes On Mars. *Scientific Reports*, 7(1), p.14181. https://doi.org/10.1038/s41598-017-14132-2.

Mellon, M.T., Jakosy, B.M., Haberle, R.M. 1993. Geographic variations in the thermal and diffusive stability of ground ice on Mars. *Journal of Geophysical Research: Planets*, 98(E2), 3345–3364. https://doi.org/10.1029/92JE02355.

Pasquon, K., Gargani, J., Massé, M., Conway, S.J., 2016. Present-day formation and seasonal evolution of linear dune gullies on Mars. *Icarus*, 274, pp.195–210. https://doi.org/10.1016/j.icarus.2016.03.024.

Pasquon, K., Gargani, J., Nachon, M., Conway, S.J., Massé, M., Jouannic, G., Balme, M.R., Costard, F., Vincendon, M., 2017. Are the different gully morphologies due to different formation processes on the Kaiser dune field? *In*: Conway, S.J., Carrivick, J.L., Carling, P.A., de Haas, T. & Harrison, T.N. (eds) *Martian Gullies and their Earth Analogues.* Geological Society, London, Special Publications, 467.

Pelletier, J.D., Kolb, K.J., Mcewen, A.S. & Kirk, R.L. 2008. Recent bright gully deposits on Mars: wet or dry flow? *Geology*, 36(3), pp.211–214. https://doi.org/10.1130/G24346A.1.

Pilorget, C., Forget, F., 2016. Formation of gullies on Mars by debris flows triggered by $CO_2$ sublimation. *Nature Geosciences*, 9, pp.65–69. https://doi.org/10.1038/ngeo2619.

Piqueux, S., Kleinböhl, A., Hayne, P.O., Kass, D.M., Schofield, J.T. & Mccleese, D.J. 2015. Variability of the Martian seasonal $CO_2$ cap extent over eight Mars Years. *Icarus*, 251, pp.164–180. https://doi.org/10.1016/j.icarus.2014.10.045.

Raack, J., Reiss, D., Appéré, T., Vincendon, M., Ruesch, O., Hiesinger, H., 2015. Present-day seasonal gully activity in a south polar pit (Sisyphi Cavi) on Mars. *Icarus*, 251, pp.226-243. https://doi.org/http://dx.doi.org/10.1016/j.icarus.2014.03.040.

Raack, J., Conway, S.J., Herny, C., Balme, M.R., Carpy, S. & Patel, M.R. 2017. Water-induced sediment levitation enhances downslope transport on Mars. *Nature Communications*, 8(1), p.1151. https://doi.org/10.1038/s41467-017-01213-z.

Reiss, D., Jaumann, R., 2003. Recent debris flows on Mars: Seasonal observations of the Russell Crater dune field. *Geophysical Research Letters*, 30(6), pp.3–6. https://doi.org/10.1029/2002GL016704.

Reiss, D., Van Gasselt, S., Neukum, G. & Jaumann, R. 2004. Absolute dune ages and implications for the time of formation of gullies in Nirgal Vallis, Mars. *Journal of Geophysical Research: Planets*, 109(E6). https://doi.org/10.1029/2004JE002251.

Reiss, D., Hiesinger, H., Hauber, E. & Gwinner, K. 2009. Regional differences in gully occurrence on Mars: a comparison between the Hale and Bond craters. *Planetary and Space Science*, 57(8), 958–974. https://doi.org/10.1016/j.pss.2008.09.008.

Reiss, D., Erkeling, G., Bauch, K.E. & Hiesinger, H. 2010. Evidence for present day gully

activity on the Russell crater dune field, Mars. *Geophysical Research Letters*, 37(6). https://doi.org/10.1029/2009GL042192.

Schon, S.C., Head, J.W. & Fassett, C.I. 2009. Unique chronostratigraphic marker in depositional fan stratigraphy on Mars: evidence for ca. 1.25 Ma gully activity and surficial meltwater origin. *Geology (Boulder)*, 37(3), pp.207–210. https://doi.org/10.1130/G25398A.1.

Seiferlin, K., Ehrenfreund, P. Et Al. 2008. Simulating Martian regolith in the laboratory. *Planetary and Space Science*, 56(15), pp.2009–2025. https://doi.org/10.1016/j.pss.2008.09.017.

Siegler, M., Aharonson, O., Carey, E., Choukroun, M., Hudson, T., Schorghofer, N. & Xu, S. 2012. Measurements of thermal properties of icy Mars regolith analogs. Journal of *Geophysical Research: Planets*, 117(E3). https://doi.org/10.1029/2011JE003938.

Sizemore, H.G.& Mellon, M.T. 2008. Laboratory characterization of the structural properties controlling dynamical gas transport in Mars-analog soils. *Icarus*, 197, pp.606–620. https://doi.org/10.1016/j.icarus.2008.05.013.

Soare, R.J., Conway, S.J., Gallagher, C. & Dohm, J.M. 2016. Sorted (clastic) polygons in the Argyre region, Mars, and possible evidence of pre- and post-glacial periglaciation in the Late Amazonian Epoch. *Icarus*, 264, pp.184–197. https://doi.org/10.1016/j.icarus.2015.09.019.

Stewart, S.T. & Nimmo, F. 2002. Surface runoff features on Mars: testing the carbon dioxide formation hypothesis. *Journal of Geophysical Research*, 107(E9), pp.7-1-7-12. https://doi.org/10.1029/2000JE001465.

Sylvest, M.E., Conway, S.J., Patel, M.R., Dixon, J.C., Barnes, A., 2016. Mass wasting triggered by seasonal $CO_2$ sublimation under Martian atmospheric conditions: Laboratory experiments. *Geophysical Research Letters*, 43, pp.12,363-12,370. https://doi.org/10.1002/2016GL071022.

Tomasko, M.G., Doose, L.R., Lemmon, M., Smith, P.H. & Wegryn, E. 1999. Properties of dust in the Martian atmosphere from the Imager on Mars Pathfinder. *Journal of Geophysical Research: Planets*, 104(E4), pp.8987. https://doi.org/10.1029/1998JE900016.

Vincendon, M., 2015. Identification of Mars gully activity types associated with ice composition. *Journal of Geophysical Research: Planets*, 120(11), pp.1859–1879. https://doi.org/10.1002/2015JE004909.

## 3.8 Appendix A

### 3.8.1 Method details

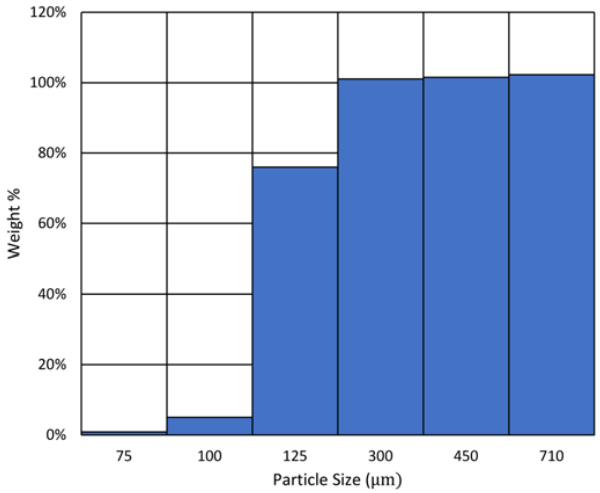


**Figure 3.11.** Grain size distribution for fine sand.

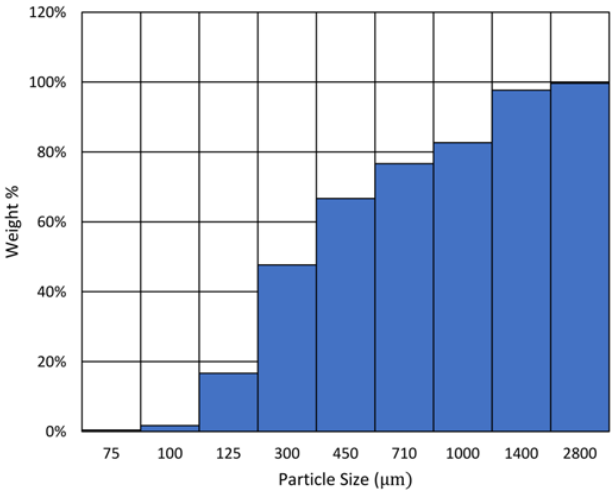


**Figure 3.12.** Grain size distribution for coarse sand.

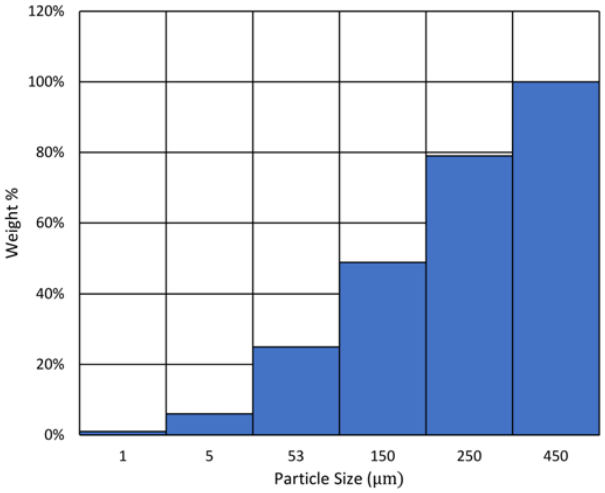


**Figure 3.13.** Grain size distribution for JSC Mars-1.

**Table 3.5.** Summary of experimental parameters

| Parameter | Value |
|---|---|
| Heat lamp wattage | 500 W |
| Maximum insolation intensity* | 350 W $m^{-2}$ |
| Chamber pressure at start of cooling | 350 mbar |
| Maximum surface temperature at start of condensation | -120℃ |
| Target chamber pressure during sublimation | 5 – 7 mbar |

*The heat transfer analysis used to estimate the maximum insolation intensity is presented in the Supporting Information from Sylvest *et. al*, (2016).

**Table 3.6.** Slope temperatures during the sublimation process

| Run ID | Sediment | Initial angle | Initial slope temperature (°C) | | | Final slope temperature (°C) | | |
|---|---|---|---|---|---|---|---|---|
| | | | Surface | Mean | Basal | Surface | Mean | Basal |
| 1 | Fine Sand | 10° | -120.3 | -132.2 | -156.3 | -31.3 | -62.5 | -93.9 |
| 2 | Fine Sand | 15° | -118.3 | -124.7 | -137.3 | 12.7 | 10.6 | 11.1 |
| 3 | Fine Sand | 20° | -133.1 | -142.9 | -163.5 | -30.9 | -59.2 | -87.7 |
| 4 | Fine Sand | 25° | -123.7 | -139.9 | -160.7 | -38.7 | -64.1 | -85.4 |
| 5 | Fine Sand | 25° | -128.4 | -141.0 | -160.6 | -40.3 | -64.8 | -96.7 |
| 6 | Fine Sand | AOR | -127.0 | -135.7 | -150.2 | -108.7 | -116.9 | -117.8 |
| 7 | Fine Sand | AOR | -121.5 | -131.9 | -169.6 | -48.7 | -73.4 | -83.0 |
| 8 | Fine Sand | AOR | -122.6 | -138.0 | -165.3 | -84.2 | -99.0 | -102.9 |
| 9 | JSC Mars-1 | 10° | -135.0 | -141.2 | -169.2 | -25.3 | -50.6 | -99.3 |
| 10 | JSC Mars-1 | 15° | -133.8 | -139.4 | -167.5 | -13.6 | -47.2 | -99.9 |
| 11 | JSC Mars-1 | 15° | -134.6 | -142.1 | -167.9 | -24.8 | -50.5 | -90.0 |
| 12 | JSC Mars-1 | 15° | -132.4 | -142.6 | -167.6 | -21.4 | -51.4 | -99.5 |
| 13 | JSC Mars-1 | 17.5° | -127.3 | -140.9 | -167.3 | -0.6 | -44.9 | -90.0 |
| 14 | JSC Mars-1 | 17.5° | -128.5 | -140.9 | -167.4 | -7.0 | -45.6 | -93.8 |
| 15 | JSC Mars-1 | 17.5° | -122.4 | -136.4 | -161.6 | -11.1 | -44.5 | -89.3 |
| 16 | JSC Mars-1 | 17.5° | -128.6 | -141.1 | -165.4 | -20.4 | -45.1 | -70.3 |
| 17 | JSC Mars-1 | 20° | -133.1 | -140.0 | -167.0 | -18.6 | -51.1 | -48.5 |
| 18 | JSC Mars-1 | 20° | -127.6 | -141.6 | -166.7 | -64.0 | -89.4 | -101.3 |
| 19 | JSC Mars-1 | 20° | -124.4 | -138.6 | -144.5 | -44.3 | -79.8 | -51.6 |
| 20 | JSC Mars-1 | AOR | -121.1 | -128.6 | -161.8 | -52.6 | -76.7 | -109.6 |
| 21 | JSC Mars-1 | AOR | -120.3 | -143.5 | -171.2 | -25.7 | -61.8 | -76.1 |
| 22 | JSC Mars-1 | AOR | -119.9 | -143.4 | -162.2 | -34.9 | -86.7 | -109.6 |
| 23 | JSC Mars-1 | AOR | -123.3 | -143.6 | -167.1 | -37.8 | -76.3 | -91.6 |
| 24 | JSC Mars-1 | AOR | -122.1 | -120.7 | -80.2 | -36.8 | -55.8 | -33.4 |
| 25 | Coarse Sand | AOR | -124.9 | -135.8 | -150.2 | 13.4 | 12.1 | 14.3 |
| 26 | Coarse Sand | AOR | -112.2 | -127.9 | -143.6 | -43.0 | -77.2 | -98.6 |

**Table 3.7.** Potential sources of error

| Error Source | Comments |
|---|---|
| Noise in the captured video frames | |
| Lens distortion | The camera alignment procedure in PhotoScan determines internal camera parameters through self-calibration, which can be less effective than a laboratory-type camera calibration. A virtual set of camera locations with convergent geometry was employed to minimise this error. |
| Scanning distortion | Although a high frame rate was used (60 fps progressively scanned), this type of rolling shutter means very rapid movements can be offset from one edge of the charge coupled device (image sensor) to the other. |
| Poor placement of the cameras | Particularly important with only two cameras. The spacing and angles of the cameras relative to the slope surface can influence the accuracy of the resulting 3D measurements. |
| Errors in the physical measurement of the photogrammetric markers | The measurements are within < 1 mm. |
| Errors in the placement of the photogrammetric reference markers in each of the captured video frames | Placements are within < 1 mm. |
| Differences in lighting | |
| Differences in surface texture | |

**Table 3.8.** Photogrammetric error estimates

| Run ID | $X$ rms (mm) | $Y$ rms (mm) | $Z$ rms (mm) | $V_{noise}$ ($cm^3$) | $\%V_{noise}$ ($cm^3$) |
|---|---|---|---|---|---|
| 1 | 1.00 | 0.94 | 0.57 | 4.20 | 0.12 |
| 2 | 1.01 | 1.52 | 0.47 | 6.01 | 0.18 |
| 3 | 1.27 | 1.35 | 0.82 | 24.85 | 0.79 |
| 4 | 1.35 | 1.25 | 0.64 | 14.37 | 0.53 |
| 5 | 1.38 | 1.75 | 0.54 | 10.45 | 0.30 |
| 6 | 1.00 | 0.84 | 1.32 | 58.75 | 1.73 |
| 7 | 1.69 | 1.60 | 0.59 | 11.34 | 0.37 |
| 8 | 1.66 | 2.69 | 2.29 | 100.89 | 2.91 |
| 9 | 2.02 | 2.68 | 0.58 | 13.68 | 0.41 |
| 10 | 1.00 | 1.04 | 0.54 | 31.19 | 0.75 |
| 11 | 1.02 | 0.93 | 0.57 | 15.18 | 0.35 |
| 12 | 0.98 | 0.89 | 1.00 | 42.50 | 1.10 |
| 13 | 1.64 | 2.42 | 0.83 | 34.11 | 0.86 |
| 14 | 1.05 | 0.94 | 0.69 | 20.67 | 0.56 |
| 15 | 1.00 | 0.93 | 0.43 | 3.02 | 0.07 |
| 16 | 2.52 | 3.06 | 0.72 | 4.70 | 0.12 |
| 17 | 0.96 | 8.87 | 0.70 | 23.27 | 0.67 |
| 18 | 0.99 | 0.97 | 0.71 | 24.43 | 1.06 |
| 19 | 1.03 | 1.08 | 0.55 | 1.75 | 0.08 |
| 20 | 0.23 | 1.30 | 0.79 | 8.49 | 0.18 |
| 21 | 0.53 | 1.21 | 0.95 | 24.79 | 0.61 |
| 22 | 0.96 | 1.12 | 1.32 | 59.02 | 1.25 |
| 23 | 4.37 | 0.69 | 1.37 | 49.88 | 1.71 |
| 24 | 0.59 | 0.60 | 0.55 | 1.18 | 0.03 |
| 25 | n/d | n/d | n/d | n/d | n/d |
| 26 | 1.21 | 1.12 | 1.20 | 46.97 | 1.30 |

rms = root mean square error, n/d: No data. $X$ = long-slope coordinate, $Y$ = cross-slope coordinate.

### 3.8.2 Results

**Table 3.9.** Pearson correlation coefficients

| | Initial angle v. erosion | Initial angle v. deposition | Frost volume v. erosion | Frost volume v. deposition |
|---|---|---|---|---|
| JSC Mars-1 | 0.707 | 0.675 | 0.195 | 0.361 |
| Fine sand | 0.530 | 0.098 | -0.378 | 0.065 |

Note: Correlation coefficients for coarse sand would be meaningless, as there were only two runs with this sediment.

## 3.9 Appendix B

### 3.9.1 Physical model

The system of equations (4 and 5) does not have a similarity solution in simple functions, but approximate solutions can be generated by a variety of methods. For long times, most of the heat has gone into heating the sand, and only a smaller fraction into subliming $CO_2$. In this regime $X(t) \propto \sqrt{t}$. For short times, however, most of the heat goes into subliming $CO_2$, and $X(t) \propto t$. A simple method to get an approximate solution is to assume an approximate temperature profile of the form

$$T(t,x) = \begin{cases} T_s + \left(1 - \frac{x}{X(t)}\right)\left(T_1(t) + T_2(t)\frac{x}{X(t)}\right), \ x \in [0, X(t)] & 0 \le x \le X(t) \\ T_s & x > X(t) \end{cases} \quad \text{(B1)}$$

This is similar to the approach of Goodman (1958). All three boundary conditions are satisfied if

$$T_1 = X\frac{\rho_i e\dot{X} + Q}{2\kappa} \quad \text{(B2)}$$

$$T_2 = X\frac{\rho_i e\dot{X} - Q}{2\kappa} \tag{B3}$$

The final equation comes from requiring that the mean error in the conduction equation is zero, or that the total heat input matches the sublimation energy and heat increase in the sand. That is

$$Qt = \rho_i eX + \int_0^X \rho_s c(T - T_s)dx \tag{B4}$$

This equation simplifies to an ODE in $f(s)$

$$f^2 f' + \frac{f^2}{2} + 3f = 3s \tag{B5}$$

This equation cannot be solved exactly. It is like an Abel equation, but with a quartic, rather than a cubic, form. It can easily be solved numerically, or approximated numerically. We are primarily concerned with the derivative, $f'$, since this sets the gas flux. This is well approximated by

$$f' = \frac{1 + 3s/5}{\sqrt{1 + 3s + 2s^2 + s^3/25}} \tag{B6}$$

and has the exact large and small $s$ behaviour. The flux rate falls to half its initial value when $s \approx 2.5$. With the numbers in Table B1 (Mars conditions), we get a 5.1° reduction of bed friction angle, $\theta$, for fine sand and a 50.3° reduction for JSC Mars-1. The unphysically large reduction

for JSC Mars-1 (greater than the angle of repose) implies that the sublimed $CO_2$ gas is capable of levitating grains of this regolith at any angle, which is consistent with the observed entrainment behaviour described above. The much smaller reduction of bed friction angle for fine sand is also consistent with our results, these slopes only failing at angles near the static angle of repose.

**Table 3.10.** *Model parameters for internal friction angle calculations*

| Symbol | Value | | | Definition |
|---|---|---|---|---|
| $Q$ | 350 $W \cdot m^{-2}$ | | | Radiant heating |
| $p_0$ | 510 Pa | | | Atmospheric pressure |
| $g$ | 9.81 $m \cdot s^{-2}$ | | | Terrestrial gravity |
| $g_M$ | 3.71 $m \cdot s^{-2}$ | | | Martian gravity |
| $e$ | $5.7 \times 10^5$ $J \cdot kg^{-1}$ | | | Enthalpy of sublimation for $CO_2$ |
| | $1.3 \times 10^{-5}$ Pa·s | | | Dynamic viscosity of $CO_2$ |
| $\rho_g$ | $5 \times 10^{-2}$ $kg \cdot m^{-3}$ | | | Gas density of $CO_2$ |
| $\rho_i$ | 15 $kg \cdot m^{-3}$ | | | Solid density of interpore $CO_2$ frost |
| | $\tan 30°$ | | | Bed friction‡ |
| | Fine Sand | JSC Mars-1 | Coarse Sand | |
| $\kappa$ | 0.2 $W \cdot m \cdot K^{-1}$ | 0.08 $W \cdot m \cdot K^{-1}$ [*] | 0.2 $W \cdot m \cdot K^{-1}$ | Thermal conductivity |
| $c$ | 680 $J \cdot kg^{-1} \cdot K^{-1}$ | 448 $J \cdot kg^{-1} \cdot K^{-1}$ [†] | 680 $J \cdot kg^{-1} \cdot K^{-1}$ | Heat capacity |
| $\rho_s$ | $1.68 \times 10^3$ $kg \cdot m^{-3}$ | $0.871 \times 10^3$ $kg \cdot m^{-3}$ | $1.70 \times 10^3$ $kg \cdot m^{-3}$ | Bulk density |
| $k$ | $1.51 \times 10^{-10}$ $m^2$ | $3.0 \times 10^{-11}$ $m^2$ | $5.99 \times 10^{-10}$ $m^{-2}$ | Permeability |

[*](*Seiferlin et al.* 2008)
[†](*Siegler et al.* 2012)
‡Where 30° is the assumed initial internal friction angle

## 3.10 Appendix C

### 3.10.1 Authorship Certification

UNIVERSITY OF ARKANSAS

**Arkansas Center for Space and Planetary Sciences**
**Stone House North**
**University of Arkansas**
**Fayetteville AR 27201**

**http://www.spacecenter.uark.edu**

E-mail: csaps@uark.edu

Office: (479) 575-7625
Fax: (479) 575-7778

April 13, 2018

To Whom it May Concern:

I hereby certify that my students Matthew Sylvest is the first author of this paper "CO2 sublimation in Martian Gullies: Laboratory experiments at varied slope angle and regolith grain sizes" and that he completed more than 51% of the work reported in the paper.

Sincerely

John C. Dixon
Professor Emeritus and Dissertation Director

# 4 $CO_2$ Sublimation in Martian Gullies: Laboratory Results Under Terrestrial and Martian Conditions Compared

M. E. Sylvest[1,2], J. C. Dixon[1], S. J. Conway[2,3], M. R. Patel[2,4], A. Barnes[5], J. N. McElwaine[6,7]

[1]Arkansas Center for Space and Planetary Sciences, University of Arkansas, Fayetteville, Arkansas, USA.

[2]School of Physical Sciences, Open University, Milton Keynes, UK.

[3]CNRS UMR 6112, Laboratoire de Planétologie et Géodynamique Université de Nantes, Nantes, France.

[4]Space Science and Technology Department, STFC Rutherford Appleton Laboratory, Oxfordshire, UK.

[5]Center for Advanced Spatial Technologies, University of Arkansas, Fayetteville, Arkansas.

[6]Department of Earth Sciences, Durham University, Durham, UK.

[7]Planetary Science Institute, Tucson, Arizona, USA.

## 4.1 Abstract

The surface of Mars is an active, evolving landscape, as highlighted by observations of ongoing modification and extension of martian gullies. The locations and timings of these modifications appear to be related to the seasonal sublimation of $CO_2$ frost. While the sublimation of water-ice is a familiar process in terrestrial landscape modification, the sublimation of $CO_2$ frost under martian conditions is not. To date, few experimental studies have examined the effects sublimating $CO_2$ frost might have on martian hillslopes. This work seeks to

provide context for understanding the interaction between seasonal $CO_2$ frost and unconsolidated sediment slopes, through comparison of laboratory experiments under terrestrial and martian atmospheric conditions. We conclude that the rate of pressurisation within the pore space of sediment slopes controls both the type and amount of mass wasting triggered. Further, we propose that the rates of sublimation for $H_2O$ ice under terrestrial conditions are too low to trigger mass wasting, evolving $H_2O$ vapour having ample time to diffuse through the pore space and vent to the atmosphere.

## 4.2 Introduction

Ongoing modification and extension of martian gullies (e.g. Diniega et al., 2013; Dundas et al., 2017; Hansen, 2013; Raack et al., 2014) may be the result of the sublimation of seasonal $CO_2$ frost deposits. Several studies have noted that this gully activity is consistently observed during late winter, when seasonal frost is beginning to sublimate (Dundas et al., 2017, 2015, 2012, 2010; Hansen et al., 2015; Pasquon et al., 2017, 2016). Only a few experimental studies have examined the potential role of sublimating $CO_2$ frost in hillslope processes. Two of the existing studies, Diniega et al. (2013) and Mc Keown et al. (2017) have focused specifically on linear dune gullies. Diniega et al. (2013) proposed that blocks of $CO_2$ ice could break off from cornices of accumulated seasonal frost, and slide down the dune slopes, levitated by a cushion of $CO_2$ gas. They demonstrated the feasibility of this model by successfully reproducing levied channel forms consistent with linear gully observations in a series of field experiments. Mc Keown et al. (2017) performed laboratory experiments, under terrestrial temperature and pressure that demonstrated the levitation of $CO_2$ ice blocks placed on relatively hot sediment.

They also confirmed the potential for the burrowing of these blocks which might account for terminal pits, unique to linear gullies.

In this work, we compare the results of three interrelated experimental studies, in order to identify commonalities and differences in the response of slopes to sublimating $CO_2$ frost, under terrestrial and martian atmospheric conditions. In summary, the aim of the first study was to determine whether the sublimation of $CO_2$ ice could trigger mass wasting on slopes of unconsolidated sediment in a terrestrial environment. Based on the positive results from this previously unpublished work, the second study (Sylvest et al., 2016) was developed to test the ability of condensed $CO_2$ surface frost to similarly mobilise slopes of unconsolidated sediment under martian atmospheric conditions. After condensing $CO_2$ frost on/in slopes of JSC Mars-1 regolith simulant near the angle of repose, the frost was sublimated at martian atmospheric temperature and pressure. Based on these experiments (runs 43-47 in Table 4.1), Sylvest et al. (2016) suggested that the observed mass wasting was triggered by the reduction of the static friction angle of the slope, due to increased pore pressure resulting from the rapid evolution of gas from frost sublimating within the slope. Lastly, the aim of the third study (Sylvest et al., 2018) was to quantitatively evaluate this hypothesised mechanism. To that end, Sylvest et al. (2018) developed an analytical model that successfully predicted the results of additional experimental simulations under martian atmospheric conditions (the balance of runs 24-49), over a range of initial slope angles, using fine and coarse sand, as well as JSC Mars-1.

## 4.3 Approach

This study encompasses forty-nine experiments conducted in six sets. The first three sets were conducted under terrestrial conditions, in a cold-room at the University of Arkansas Poultry Science Center, Fayetteville, US. The last three sets were conducted under martian atmospheric conditions, in the Mars Simulation Chamber (MSC) at the Open University, Milton Keynes, UK (Figure 4.1). While the details of each set varied significantly, all followed a common, three-step outline: (1) preparation of a regolith simulant slope in a sample container, (2) placement of $CO_2$ ice on or in the slope, and (3) sublimation of the $CO_2$ ice. All of the runs were video-recorded for detailed observation and, for later sets, photogrammetric modelling. Table 4.2 provides a summary of the experimental parameters for each run. Grain size distributions for the three

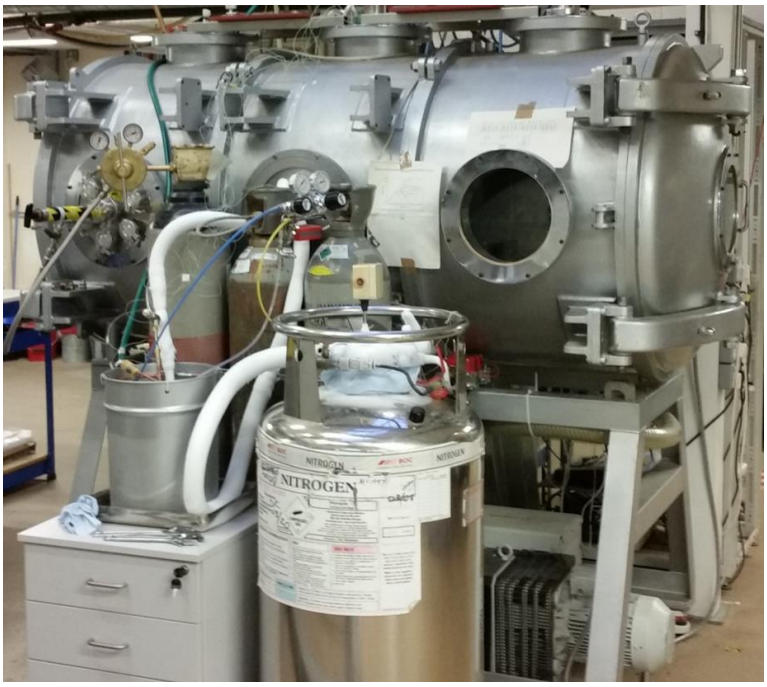


**Figure 4.1.** The Mars Simulations Chamber (top) in which Sets IV-VI were conducted, at the Open University, Milton Keynes. Large vacuum pump (lower right), liquid nitrogen Dewar (lower center) and $CO_2$ gas cooler (left).

sediments used are presented in Figure 3.11. Details of the apparatus and procedure specific to each set are presented below.

### 4.3.1 Sets I-III: (1-23) terrestrial conditions

Atmospheric conditions in the cold-room were relatively cold and humid by terrestrial standards. The temperature varied during and between each run, ranging from 3°C to 13°C, with a mean of 8°C. Relative humidity ranged from 52% to 79% between all runs, with a mean of 64%. There was limited control over the cold-room temperature, and no humidity control.

For all of the cold-room experiments, the regolith simulant was pre-cooled to a uniform temperature of approximately -20°C before use. For each experiment, a base layer of regolith simulant was first added to a box, and then granulated $CO_2$ ice, or $CO_2$ ice and regolith mixture, was added to the base layer. A shaved-ice machine was used to prepare the granular $CO_2$ ice for both convenience and consistency, yielding ice grains of roughly 2 mm on average, with a maximum size of approximately 5 mm. The rate of sublimation was enhanced with a 150 W halogen flood lamp mounted approximately 22-33 cm above the centre of each slope. Further details specific to the apparatus and procedure for each set are presented in the following sections.

#### 4.3.1.1 Set I (1-11)

The sample container for Set I was a Lexan box, 18 cm long, 12 cm wide and 12 cm tall (Figure 4.2). First, a 5 mm to 10 mm thick base layer of chilled JSC Mars-1 regolith simulant was spread loosely (without compaction) over the bottom of the box. Next, a mixture of granular $CO_2$ ice and additional JSC Mars-1 was spread over the base layer, to a depth of up to 5 mm. The

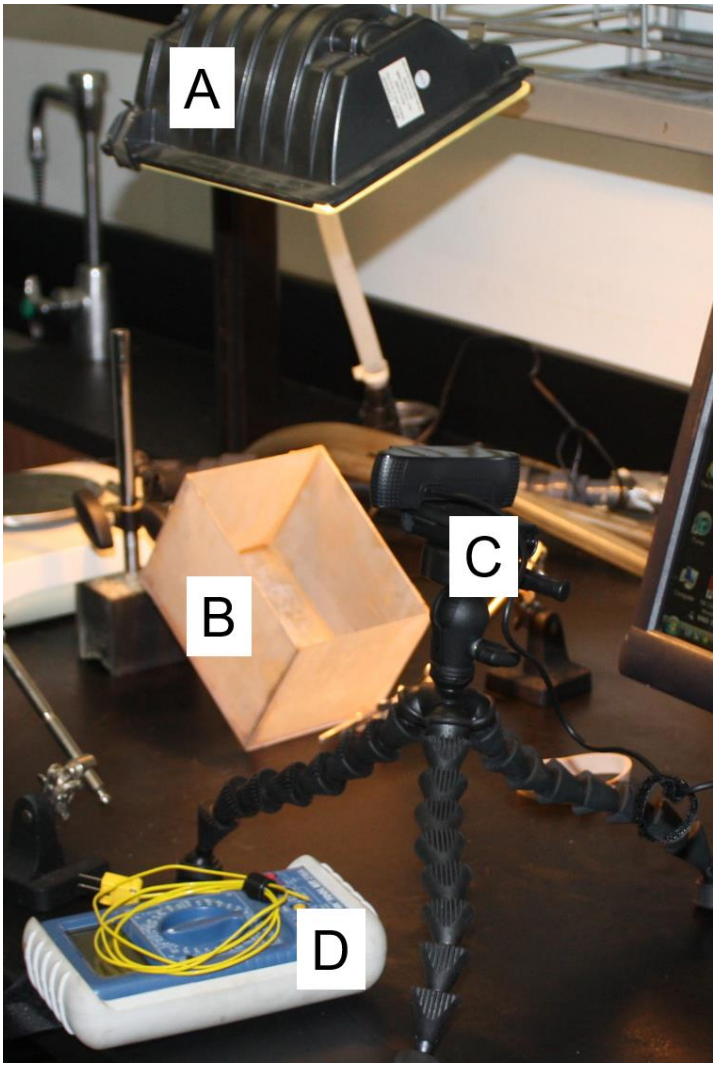


**Figure 4.2.** Set I experimental apparatus in the cold-room. (A) 150 W halogen heat lamp, (B) Lexan box, (C) HD webcam and (D) type K thermocouple.

layering process was conducted with the box positioned horizontally on the worktop, facilitating the formation of uniform layers, parallel to the box bottom. Finally, the container was carefully placed at an angle from 20° to 35° from horizontal, underneath the heat lamp (Figure 4.2). These experimental runs became active from the moment the $CO_2$ ice was introduced to the box, as the room conditions were well above the sublimation point for $CO_2$ ice. Consequently, it was not

possible to observe the initial, undisturbed slope. Run duration and recording were predicated on observed activity and visible $CO_2$ ice; typically, approximately 40 min.

#### 4.3.1.2 **Set II (12-15)**

The sample container for Set II was a Plexiglass box, 30 cm long, 12 cm wide and 16 cm tall, with sloping sides (Figure 4.3). Initially, a vertical baffle was placed inside the box, approximately 12 cm from the rear wall. This cavity was then filled to a depth of approximately 12 cm with loose JSC Mars-1 regolith simulant (pre-cooled to -20°C). Next, a layer of 1-2 cm of granular $CO_2$ ice was placed on top of the column and covered with 5-10 mm of regolith spread over the ice. Next, the box was placed under heat lamp, and the baffle removed, allowing the

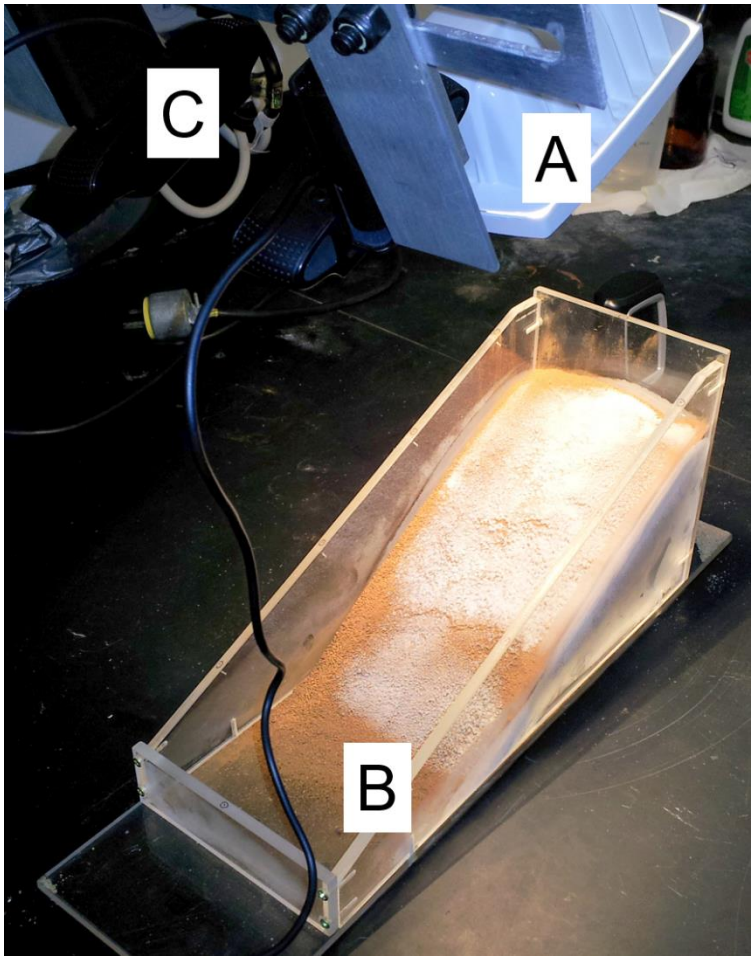


**Figure 4.3.** Set II experimental apparatus in the cold-room. (A) 150 W halogen heat lamp, (B) Plexiglass box, (C) pair of matching HD webcams.

layered ice and regolith column to collapse and settle at the angle of repose. The lamp was approximately 33 cm above slope base for these runs. As for Set I, run durations were approximately 40 min.

Run 13 was unique, in that it was conducted following the same Set II protocol, fine sand was used in lieu of JSC Mars-1. Run 15 was also different, in the placement of the small, Lexan box from Set I within the larger, Set II Plexiglass box. This arrangement was used to test the effect of insulation below layers of regolith and ice parallel to smooth-bottomed box (Figure 4.4).

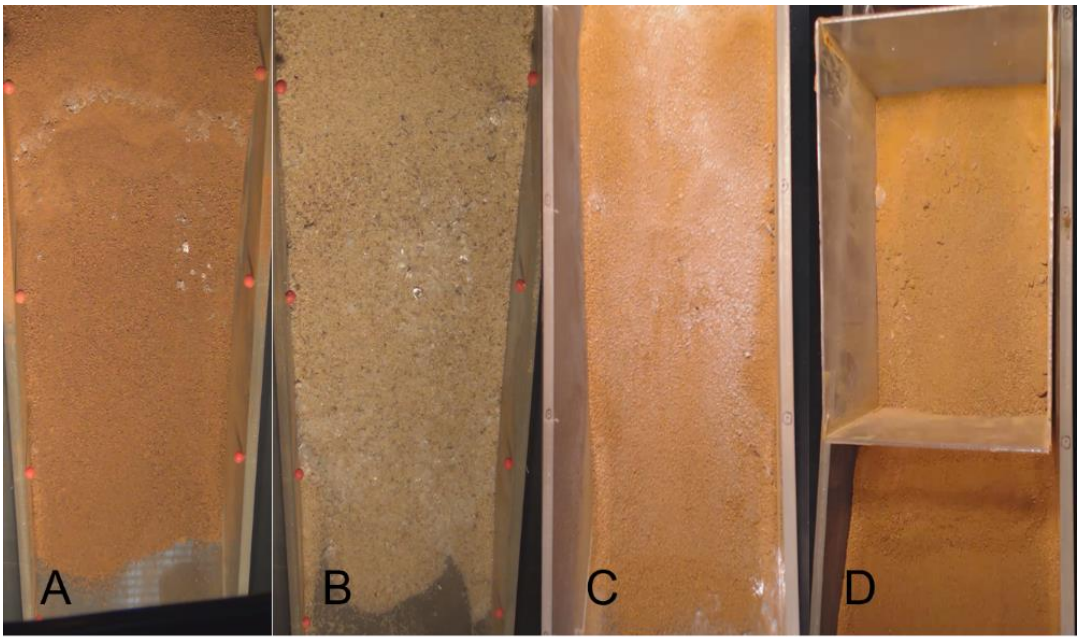


**Figure 4.4.** Initial slopes for runs 12-15. (A) Run 12, with an exposed unit of $CO_2$ ice, mantled in sediment at and above the slope crest. (B) Run 13 was unique within Set II in its use of fine sand, rather than JSC Mars-1 regolith simulant. (C) The uniform distribution of condensed H2O frost on the surface of run 14 suggests a similarly uniform distribution of granular $CO_2$ ice, below the surface. (D) For run 15 the placement of the small, Lexan box from Set I was intended to provide a comparison of the smooth-bottom box with and without insulation underneath the box.

#### 4.3.1.3 **Set III (16-23)**

The sample container for Set III was a copper box, 30 cm long, 15 cm wide and 13 cm high, with sloping sides (Figure 4.5). As for Set II, a baffle was employed to initially form a column of JSC Mars-1 regolith simulant into an approximately 10 cm high column, at the rear of the box. The baffle was then removed, allowing the regolith to slide into a slope, at or near the angle of repose.

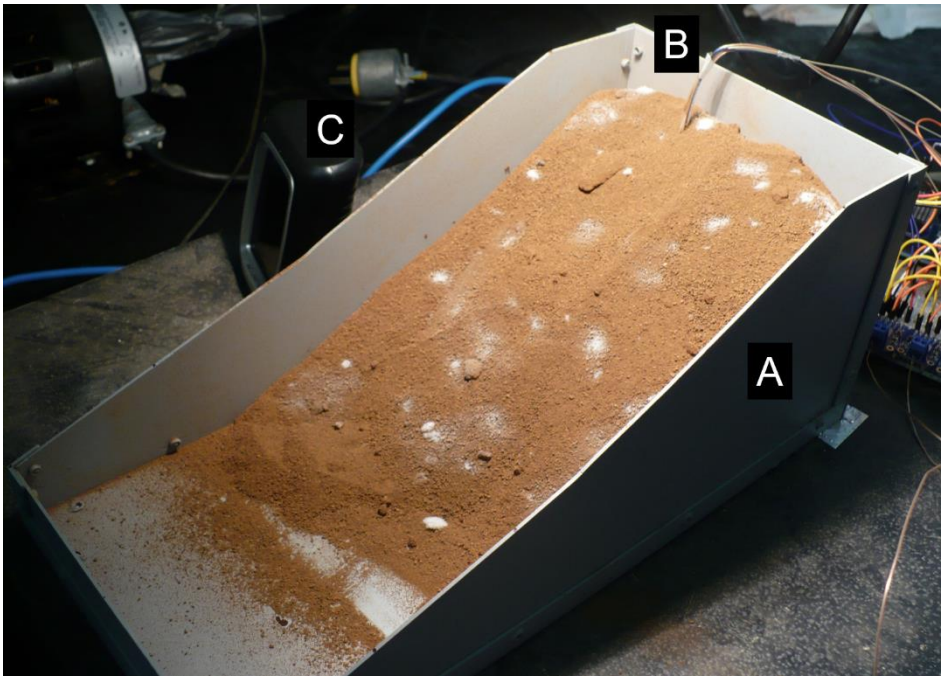


**Figure 4.5.** Set III experimental apparatus. (a) Copper box, (b) thermocouple tree, (c) digital humidity meter. The image is of run 17, after approximately 6 minutes of sublimation. Note patches of condensed $H_2O$ frost, indicative of buried $CO_2$ ice.

Finally, the granular $CO_2$ ice was spread on top of the slope. All eight runs in Set III were initially prepared with a layer of $CO_2$ ice covering from 20-95% of the slope surface (Figure 4.6). The maximum depth of the ice layer varied from 0.5 cm to 3 cm for run 17. In an effort to steepen the slope, a plastic paddle was used to sweep the slope up towards the back of the box. In doing so, a 3-6 mm thick layer of solidified ice and sediment was broken up into 2-4 $cm^2$ blocks,

which were largely mixed into the sediment as it was built up at the rear of the slope; hence the lack of $CO_2$ ice on the initial surface for run 17 in Figure 4.6.

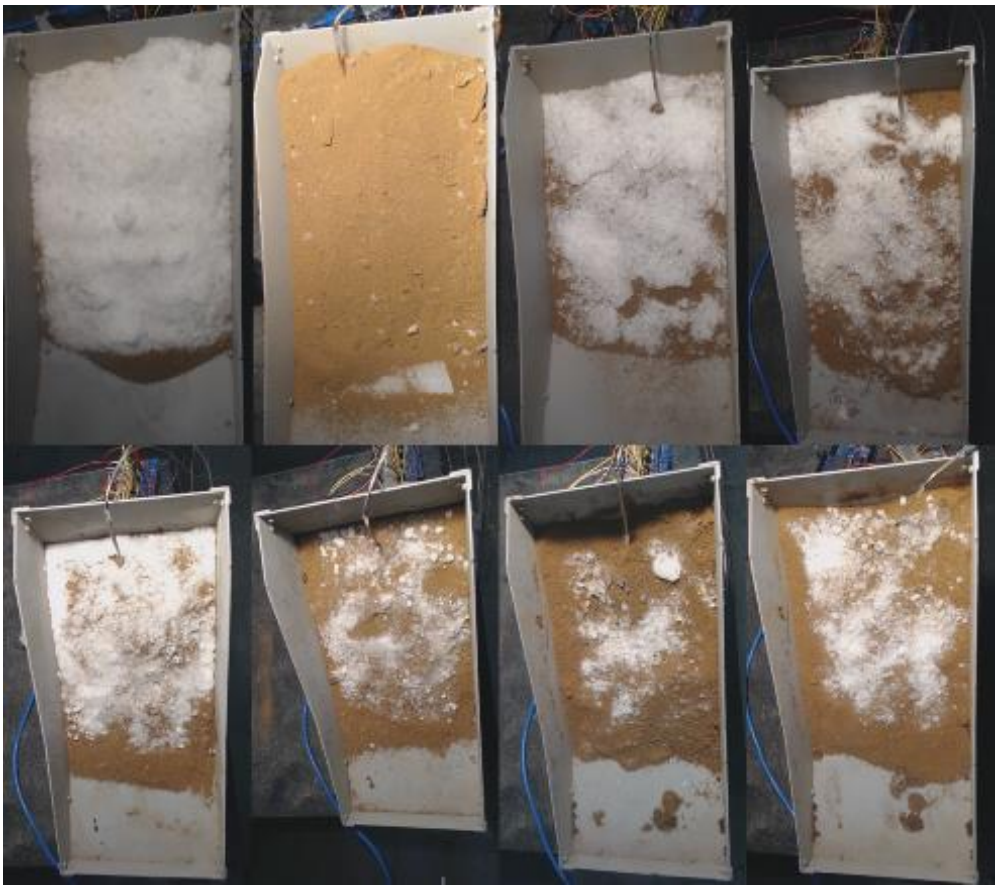

**Figure 4.6.** Set III initial slopes (runs 16-23 from top-left to bottom-right), illustrating relative $CO_2$ ice volumes and distributions.

For runs 19 through 23, the box was carefully positioned with the bottom at a slight incline, increasing the initial slope angle. While some of the regolith simulant did move, the presence of both $CO_2$ ice, and condensed $H_2O$ ice are thought to have stabilised the slope, allowing for these over-steep angles. Run durations varied from approximately 30-60 min., largely dependent on the quantity of $CO_2$ ice emplaced.

### 4.3.2 Sets IV-VI: (24-49) martian conditions

Moving the experiments from the cold-room into the 2 m long, 1 m diameter MSC (Figure 4.1 and Figure 4.7) required a fundamentally different approach for the emplacement of the $CO_2$ ice. To this end, $CO_2$ frost was condensed on the surface of the regolith slope, inside the MSC. Sets IV-VI used a common apparatus and set of procedures, the principle difference

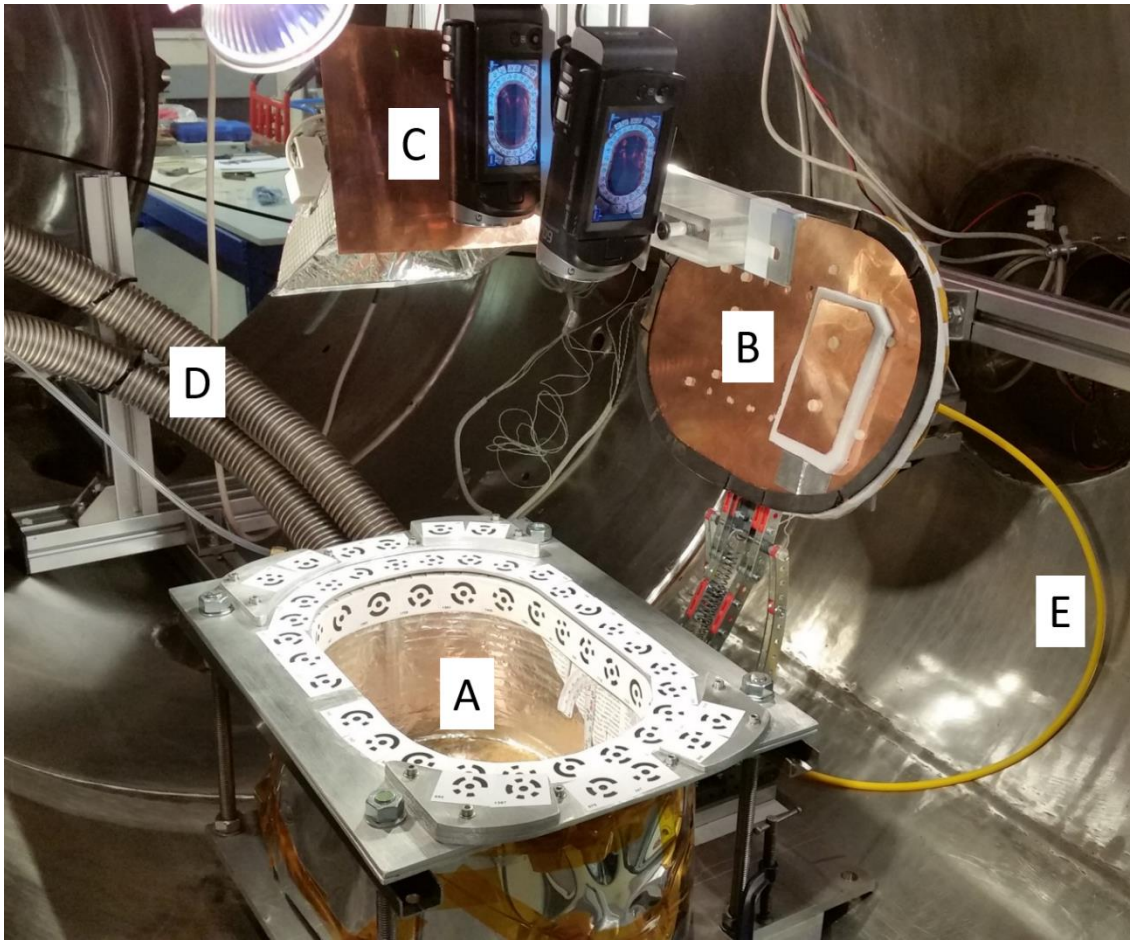


**Figure 4.7.** Inside the MSC. (A) Copper coil box with photogrammetric coded targets encircling the top. (B) Copper sheet lid mounted on hinged opening mechanism. The small rectangle attached to right edge of lid is an open-cell foam diffuser, to prevent inflowing $CO_2$ gas from disrupting slope sediment. (C) Copper heat shield, mounted between the halogen heat lamp in back, and the pair of matching Sony camcorders in front. (D) Liquid nitrogen supply and exhaust tubing. (E) $CO_2$ gas supply tubing, feeding into the box through the diffuser, when the lid is closed.

between each set of runs being the regolith simulant used, as listed in Table 4.1 and Table 4.2. Here, we briefly summarize the four-step condensation procedure employed. See Sylvest et al., (2016) for full details.

As for the previous sets, the first step was the preparation of the regolith simulant slope. For these runs, the sample container was an approximately 30 cm long, 20 cm wide, 12 cm deep box, formed from a single, continuous coil of copper tubing, with a brazed copper sheet bottom and removable copper sheet top (Figure 4.7). The regolith simulant was initially placed loosely within the box, and vacuum-dried in the MSC before use. Then, the regolith was swept up to the target initial slope angle by means of a flexible, wide, plastic spatula. A spirit-level protractor was used to guide slope preparation.

The second step in the procedure was to cool the regolith sufficiently to allow $CO_2$ gas to condense onto and into the slope surface. With the box lid closed, to prevent disruption of the slope surface, the MSC was purged with dry $N_2$. Next, liquid nitrogen was flowed through the box coils until the maximum regolith temperature was below the frost point for $CO_2$. Temperatures within the slope were monitored by two sets of type-K thermocouples, assembled on vertical rakes, which were inserted into the slope, along the centreline, one at mid-slope and the second at the slope crest (Figure 4.12). Wires were taped to the bottom and sides of the box to avoid mechanical interference with any triggered sediment movement.

The third step was the introduction of $CO_2$ gas, above the slope surface. The flow of liquid nitrogen was maintained and the box lid kept closed, throughout the condensation procedure, in order to minimise raising the temperature of the regolith due to the release of latent

heat. Additionally, the exhaust liquid nitrogen was used to pre-cool the $CO_2$ gas prior to injection into the MSC.

The final step in the procedure was to open the box lid and stereographically record the sublimation of the condensed $CO_2$ frost. For this step, the flow of liquid nitrogen was stopped and the 500 W halogen heat lamp was switched on. The pressure was manually regulated to maintain approximately 6 mbar inside the MSC throughout the sublimation step. The duration of the sublimation step was the lesser of the time required for all recorded slope temperatures to exceed the frost temperature under MSC conditions, or 100 min.

#### 4.3.2.1 **Videography & Photogrammetric methods**

For the first set of experiments, a single Logitech C920 HD webcam was used to record the sublimation process to facilitate observations and document the slope behaviour (Figure 4.2). Starting with Set II, an additional webcam was added to allow stereographic recording for the purpose of generating digital elevation models (DEMs) of the evolving slopes. Although the details of the photogrammetric methods evolved with each set of experiments, the four basic procedural steps were fundamentally the same for each set. (1) A set of control points were affixed to the apparatus and surveyed to acquire their relative 3D coordinates, (2) stereographic video was recorded, (3) synchronised screen captures were acquired from each pair of videos and (4) the pairs of screen captures were used, along with the coordinates of the control points, to develop scaled, co-referenced DEMs situated within a local reference frame (Barnes, 2011).

##### **4.3.2.1.1 Sets II & III**

As a first attempt at stereographic video recording, two matching Logitech C920 HD webcams were mounted on a purpose-built mount with a stereo baseline of 9 cm (Figure 4.3). A

fine point marker was used to place black dots (control points) at several locations on the perimeter of each box rim. The positions of the control points were then determined using close-range photogrammetric software (EOS PhotoModeler v2012) and a calibrated DSLR camera and lens. Although the reported horizontal resolution was 0.34 mm, the resulting models are not appropriate for quantitative comparisons. They do, however, illustrate the relative scale, timing and positions of sediment movements.

#### 4.3.2.1.2 Sets IV-VI

Here we summarise the photogrammetric methods used for Sets IV-VI. Full details were previously reported by Sylvest et al. (2018 & 2016). Two matched Sony HDR-CX330 camcorders were mounted above the slope, inside the MSC (Figure 4.7). Coded photogrammetric targets were affixed to plates, mounted at multiple heights, around the perimeter of the copper-coil box (Figure 4.7). These precisely located targets established a three-dimensional frame of reference and scale for photogrammetric modelling. Additional targets were mounted vertically, inside the rim of the box as tie points, to facilitate image registration. Although each frame capture consisted of only two images, photogrammetric estimation of the camera parameters was performed by supplementing the pair with images recorded from a variety of angles, before each run.

## 4.4 Observations

Sylvest et al. (2016) identified four types of sediment movement for series IV, under martian conditions. These were (1) discrete sediment flow, (2) creep, (3) tumbling of individual grains and (4) gas entrainment of sediment particles. Of these, only discrete granular flow and creep were found to trigger movement of significant volumes of sediment (Sylvest et al., 2016).

Neither grain tumbling nor entrainment where observed in any of the runs for series I-III, under terrestrial conditions.

In order to provide a basis of comparison over the wide range of experimental conditions, a subjective assessment of all forty-nine experimental runs was made, based on repeated observation of video recordings over a range of playback speeds. While higher playback speeds facilitate detection of very slow creep movements, normal playback is required to avoid miscategorising faster creep movements as discrete flows. Each run was rated on a scale from 0 to 5 for level of slope activity and volume transport attributed to each of discrete granular flow and creep, Table 4.1. As reliable quantitative results were only available for sets IV-VI (Sylvest et al., 2018), the same subjective procedure was applied to these runs as well, the quantitative results only being referenced to check for consistency in the estimated ratings.

**Table 4.1.** Estimated Activity & Volume Levels for Discrete Sediment Flow & Creep.

| Run | | | | Initial | Granular Flow | | Creep | | Combined | |
|---|---|---|---|---|---|---|---|---|---|---|
| ID | Set | Conditions | Regolith | Slope | Activity | Volume | Activity | Volume | Activity | Volume |
| 1 | I | Terrestrial | JSC Mars-1 | 30.5° | 5 | 5 | 5 | 5 | 5 | 5 |
| 2 | I | Terrestrial | JSC Mars-1 | 24.0° | 3 | 2 | 3 | 3 | 3 | 2.5 |
| 3 | I | Terrestrial | JSC Mars-1 | 29.0° | 5 | 4 | 5 | 5 | 5 | 4.5 |
| 4 | I | Terrestrial | JSC Mars-1 | 20.0° | 2 | 3 | 5 | 5 | 3.5 | 4 |
| 5 | I | Terrestrial | JSC Mars-1 | 34.0° | 5 | 5 | 5 | 3 | 5 | 4 |
| 6 | I | Terrestrial | JSC Mars-1 | 28.0° | 4 | 3 | 4 | 5 | 4 | 4 |
| 7 | I | Terrestrial | JSC Mars-1 | 24.0° | 4 | 1 | 5 | 4 | 4.5 | 2.5 |
| 8 | I | Terrestrial | JSC Mars-1 | 31.0° | 5 | 1 | 5 | 5 | 5 | 3 |
| 9 | I | Terrestrial | JSC Mars-1 | 23.0° | 4 | 1 | 5 | 5 | 4.5 | 3 |
| 10 | I | Terrestrial | JSC Mars-1 | 26.0° | 5 | 5 | 5 | 5 | 5 | 5 |
| 11 | I | Terrestrial | JSC Mars-1 | 28.0° | 5 | 5 | 5 | 5 | 5 | 5 |
| 12 | II | Terrestrial | JSC Mars-1 | 36.0° | 4 | 2 | 3 | 4 | 3.5 | 3 |
| 13 | II | Terrestrial | Fine Sand | 30.0° | 4 | 4 | 4 | 4 | 4 | 4 |
| 14 | II | Terrestrial | JSC Mars-1 | 26.9° | 1 | 1 | 3 | 5 | 2 | 3 |
| 15 | II | Terrestrial | JSC Mars-1 | 30.0° | 3 | 2 | 4 | 3 | 3.5 | 2.5 |
| 16 | III | Terrestrial | JSC Mars-1 | 25.1° | 0 | 0 | 0 | 0 | 0 | 0 |
| 17 | III | Terrestrial | JSC Mars-1 | 26.0° | 1 | 1 | 2 | 2 | 1.5 | 1.5 |
| 18 | III | Terrestrial | JSC Mars-1 | 24.3° | 1 | 1 | 2 | 2 | 1.5 | 1.5 |
| 19 | III | Terrestrial | JSC Mars-1 | 32.9° | 1 | 1 | 5 | 4 | 3 | 2.5 |
| 20 | III | Terrestrial | JSC Mars-1 | 37.0° | 2 | 4 | 3 | 4 | 2.5 | 4 |
| 21 | III | Terrestrial | JSC Mars-1 | 42.0° | 4 | 5 | 3 | 5 | 3.5 | 5 |
| 22 | III | Terrestrial | JSC Mars-1 | 31.5° | 3 | 2 | 3 | 3 | 3 | 2.5 |
| 23 | III | Terrestrial | JSC Mars-1 | 31.2° | 1 | 1 | 1 | 1 | 1 | 1 |
| 24 | IV | Martian | Fine Sand | 12.0° | 0 | 0 | 0 | 0 | 0 | 0 |
| 25 | IV | Martian | Fine Sand | 16.9° | 0 | 0 | 0 | 0 | 0 | 0 |
| 26 | IV | Martian | Fine Sand | 22.0° | 0 | 0 | 0 | 0 | 0 | 0 |
| 27 | IV | Martian | Fine Sand | 23.3° | 0 | 0 | 0 | 0 | 0 | 0 |
| 28 | IV | Martian | Fine Sand | 24.3° | 0 | 0 | 0 | 0 | 0 | 0 |
| 29 | IV | Martian | Fine Sand | 31.0° | 0 | 0 | 1 | 2 | 0.5 | 1 |
| 30 | IV | Martian | Fine Sand | 30.4° | 1 | 3 | 4 | 4 | 2.5 | 3.5 |
| 31 | IV | Martian | Fine Sand | 31.0° | 4 | 4 | 3 | 3 | 3.5 | 3.5 |
| 32 | V | Martian | JSC Mars-1 | 11.4° | 0 | 0 | 1 | 1 | 0.5 | 0.5 |
| 33 | V | Martian | JSC Mars-1 | 14.5° | 1 | 1 | 1 | 1 | 1 | 1 |
| 34 | V | Martian | JSC Mars-1 | 15.2° | 1 | 1 | 1 | 1 | 1 | 1 |
| 35 | V | Martian | JSC Mars-1 | 17.9° | 1 | 1 | 1 | 1 | 1 | 1 |
| 36 | V | Martian | JSC Mars-1 | 18.3° | 5 | 1 | 1 | 1 | 3 | 1 |
| 37 | V | Martian | JSC Mars-1 | 16.9° | 3 | 1 | 0 | 0 | 1.5 | 0.5 |
| 38 | V | Martian | JSC Mars-1 | 18.3° | 2 | 2 | 3 | 2 | 2.5 | 2 |
| 39 | V | Martian | JSC Mars-1 | 17.8° | 2 | 1 | 2 | 1 | 2 | 1 |
| 40 | V | Martian | JSC Mars-1 | 18.0° | 1 | 1 | 0 | 0 | 0.5 | 0.5 |
| 41 | V | Martian | JSC Mars-1 | 19.2° | 4 | 2 | 0 | 0 | 2 | 1 |
| 42 | V | Martian | JSC Mars-1 | 17.0° | 4 | 2 | 0 | 0 | 2 | 1 |
| 43 | V | Martian | JSC Mars-1 | 34.1° | 5 | 5 | 2 | 1 | 3.5 | 3 |
| 44 | V | Martian | JSC Mars-1 | 26.6° | 3 | 3 | 0 | 0 | 1.5 | 1.5 |
| 45 | V | Martian | JSC Mars-1 | 27.5° | 5 | 5 | 0 | 0 | 2.5 | 2.5 |
| 46 | V | Martian | JSC Mars-1 | 25.0° | 5 | 5 | 2 | 1 | 3.5 | 3 |
| 47 | V | Martian | JSC Mars-1 | 29.4° | 5 | 5 | 5 | 5 | 5 | 5 |
| 48 | VI | Martian | Coarse Sand | [1]~30° | 0 | 0 | 1 | 1 | 0.5 | 0.5 |
| 49 | VI | Martian | Coarse Sand | 33.8° | 1 | 1 | 1 | 1 | 1 | 1 |

[1]No recorded measurement available. This is a conservative estimate based on the slope being near the angle of repose.

For Sets I-III, carried out in the cold-room, the presence of visible $CO_2$ ice clasts and accumulations of $H_2O$ frost allowed estimation of the distribution of $CO_2$ ice, independently from any resulting sediment movement. While surface frost was readily apparent at the start of most runs in Sets IV-VI, the distribution of ice within the slope was less reliably suggested by plateaus in temperature traces recorded over the course of the condensation and sublimation stages of the experimental procedures. For comparison with Sets I-III, observations for Sets IV-VI, reported by Sylvest et al., (2016 and 2018) will be briefly summarised below.

### 4.4.1 Set I (1-11) JSC Mars-1 under Terrestrial Conditions

Both granular flows and creep were observed in all eleven runs (Table 4.1), activity starting within the first two minutes of each run. The areal extent of the combined sediment movement varied from approximately one-third of the slope surface to slope-wide. Granular flows typically started as small bursts of a few to several grains, followed by larger flows from 1 cm to 3 cm wide, with up to 5 cm of runout. Surface activity was consistently concentrated in regions where mantled $CO_2$ ice was present.

Run 5 developed a broad scarp region across the full width of the slope. This appears to be the result of the substantial sliding, accumulation and failure of material from the uppermost end of the slope, the bare box bottom becoming visible upslope of the scarp (Figure 4.8). All of the other runs in Set I resulted in essentially smooth slopes with no discernible morphology. The average estimated activity levels for granular flow and creep were 4.3 and 4.7, respectively; while average estimated volume transport levels were 3.2 and 4.5 (Table 4.1). These levels suggest that creep is dominant to discrete flow for these runs.

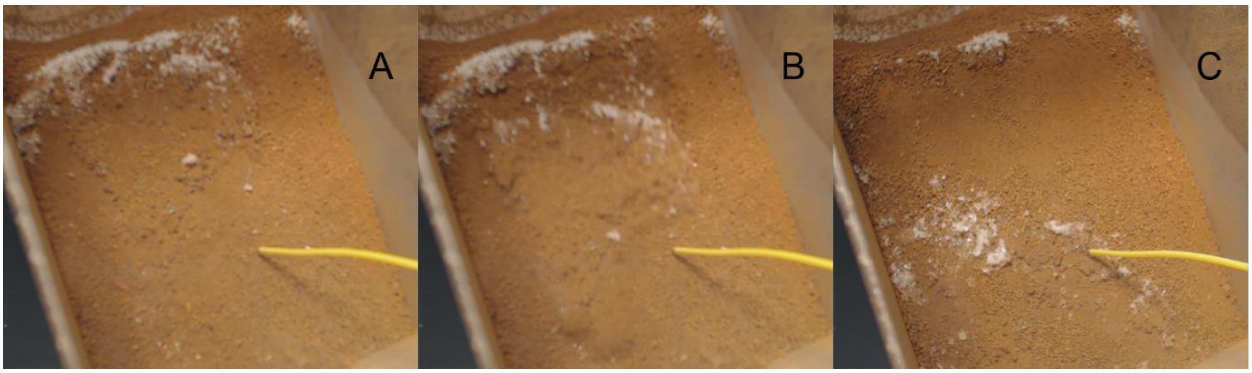


**Figure 4.8.** Image sequence depicting a large granular flow in run 5 (Set I). The bare box bottom is visible in the upper left corner of all three panels, illustrating the tendency of the sediment to slide along the smooth surface. The accumulation of $H_2O$ frost, initially along the slope crest, suggests the location of the granular $CO_2$ ice just below the surface. $CO_2$ ice clasts are also visible, generally larger than the $H_2O$ crystals. (A) Slope surface 0.07s after onset of flow. (B) The right-hand side of the crest accumulation of $H_2O$ frost is flowing downslope 0.04s later. (C) The slope became static 1.2s after the flow event began, a mixture of $H_2O$ and $CO_2$ ice crystals are now scattered along the bottom limit of the flow runout.

### 4.4.2 Set II (12-15) JSC Mars-1 & Fine Sand Under Terrestrial Conditions

Both creep and granular flow started immediately for all four runs. Activity and volume levels were consistent for all four runs in Set II. The lack of significant differences in the behaviour of runs 13 and 15 are of particular interest, due to their singular, exploratory preparations. Run 13 was unique in the use of fine sand, rather than JSC Mars-1 (Figure 4.4B), while run 15 was arranged to insulate the bottom of the sloped box (Figure 4.4D).

The distinguishing characteristics for runs 12-14 were the nature and distribution of the slope movements, which appear to be related to the distribution of the $CO_2$ ice. The ice emplacement for run 12 resulted in a concentration of $CO_2$ ice in a mantled layer of regolith at and above the crest of the slope, exposed as an approximately 1 cm thick unit, just below the slope crest (Figure 4.4A). For runs 13 and 14, the ice was distributed uniformly across the entire slope; large and small clasts partially mantled for run 13, and no $CO_2$ ice visible in run 14.

Mantled $CO_2$ ice clasts were visible over much of the slope in run 15 (Figure 4.4D), although the rapid development of $H_2O$ frost on the upper slope surface points to the concentration of $CO_2$ ice in that region. For runs 12 and 15, most activity occurred in the crest regions where $CO_2$ ice was concentrated, and to a lesser degree where ice clasts (exposed or mantled) were visible. Likewise, sediment movement for runs 13 and 14 was widely distributed across the slope surface, consistent with the distribution of $CO_2$ ice. The combined activity and transport levels for run 13, with a fine sand slope, were both 4, significantly higher than the average levels for Set II, which were 3.3 and 3.1, respectively. Comparing run 15 to the runs in Set I, insulating the bottom of the slope did appear to reduce the estimated levels of activity and volume transport (3.5 for combined activity and 2.5 for combined transport, compared to averages of 4.5 and 3.9 for Set I). The average estimated activity levels for Set II were 3.0 for discrete granular flow and 3.5 for creep. The average volume levels were 2.3 for discrete flow and 4.0 for creep. These levels suggest that creep was dominant to granular flow for these runs.

### 4.4.3 Set III (16-23) JSC Mars-1 under Terrestrial Conditions

The runs in Set III fall into two groups, based on the initial extent of $CO_2$ ice coverage of the slope surface. For the first group of runs (16, 18 and 19) more than 80% of each slope was initially covered with a dense layer of $CO_2$ ice, over 1 cm thick (Figure 4.6). Although the initial areal ice coverage of the slope for run 20 was estimated at 80-85%, the maximum estimated thickness of the ice layer is only between 4-5 mm. No sediment movement was observed for run 16, while discrete flow was minimal for runs 18 and 19 with estimated activity and volume levels of 1 (Table 4.1). The onset of the few discrete flow events for these two runs was apparently delayed by the initial lack of free surface grains. Creep was also active in runs 18 and 19. There appears to be an increasing trend in activity and volume levels for creep with

decreasing surface ice coverage (Table 4.1), which would be consistent with the stabilisation of the slope due to the widespread, dense ice layer. However, additional work is needed to more rigorously explore this hypothesis.

For the second group of runs (20-23), initial slope ice coverage was less substantial. The estimated areal extent of $CO_2$ ice coverage was between 80-85% for run 20, 50-60% for run 21, 20-30% for run 22 and 25-33% for run 23. In all four cases the maximum estimated ice depth was less than 1 cm. Runs 20-22 are the only runs in Set III that demonstrated substantial discrete flow. Estimated creep activity and transported volume levels for runs 20-22 were comparable to those for runs 18 and 19. These observations suggest that widespread, contiguous ice coverage tends to prevent granular flow and reduce creep. Gaps in the ice coverage allowed for some creep movement, and very limited discrete flows. With decreasing ice layer thickness, creep was able to overcome the stabilising effect of the surface ice. Thinner ice layers were also more readily broken up by sublimation, providing gaps in the coverage where discrete flow and creep were released. Although apparently consistent with the configuration for the runs in this group, the estimated activity and volume levels for run 23 were much lower than those for runs 20-22.

Run 17 does not fit into either of the groups described above. As detailed in the methods section, the preparation of this slope was unique to all other runs, the surface ice layer being broken up and mixed into the slope. Over the course of the run, patches of $H_2O$ frost (up to ~4 $cm^2$) formed on the surface, marking concentrations of buried $CO_2$ ice (Figure 4.5). Creep and discrete granular flow, both distributed widely across the slope, started within the first minute of the run. Discrete flows were very small, consisting of only a few grains, and with runouts less

than 1 cm. Estimated activity and volume transport levels for granular flow were both 1, creep was more active and more productive, with estimated levels of 2 (Table 4.1).

The only significant morphological change observed in Set III occurred during run 21. Initially slow to start moving, approximately 14 minutes into the run a singular slope failure revealed a crust of ice on the top half of the slope, leaving an overhang of ice above a fresh, steepened face (Figure 4.9). This run displayed more discrete sediment flow than the other runs in Set III, most of that activity being on the freshly exposed surface below the ice shelf.

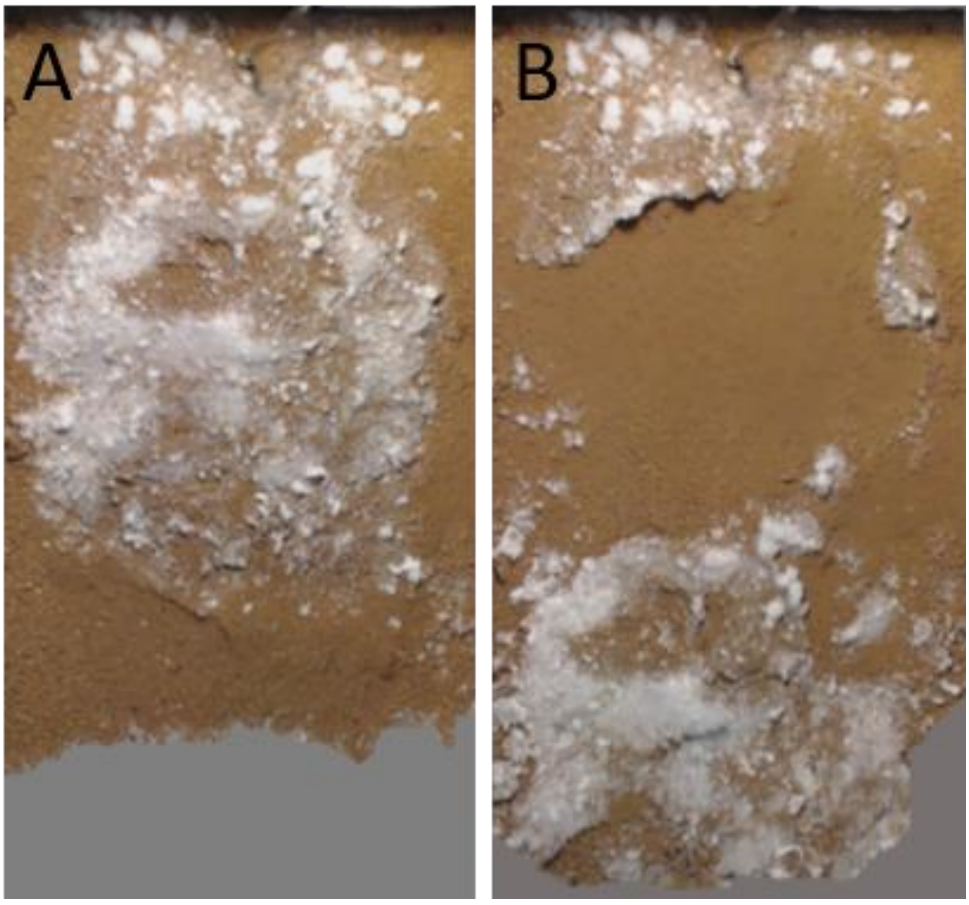


**Figure 4.9.** Example of slope surface induration due to surface ice. (A) Slope surface immediately before slope failure. (B) Resulting morphology after slope became static. Shadow near upper left-hand corner identifies undermined ice shelf.

### 4.4.4 Set IV (runs 24-31) Fine Sand under Martian Atmospheric Conditions

Sediment movement was only detected in runs 29-31, for which the fine sand slope was initially near the angle of repose. Creep was detected in all three of these runs, while granular flows were only observed in runs 30 and 31 (Table 4.1). Sediment activity and transported volume varied widely over these three runs, run 29 showing minimal activity and transport; while run 31 was very active, significantly altering the slope profile (Sylvest et al., 2018). Morphological changes to the fine sand slopes were limited to the smoothing and lowering of the slope, and the formation of depositional aprons. Averaged over all eight runs, the average activity levels for discrete flow and creep were 0.6 and 1.0, respectively; while the levels volume transport were 0.9 and 1.1. Considering only the active runs, near the angle of repose, the average activity levels are 1.7 and 2.7 for discrete flow and creep; and the average volume levels are 2.3 and 3.0. These levels suggest creep is more active and moves more sediment than discrete granular flow for these runs.

### 4.4.5 Set V (runs 32-47) JSC Mars-1 under Martian Conditions

Some degree of activity was observed for all JSC Mars-1 slopes under simulated Mars conditions (Sylvest et al., 2018). The average estimated activity levels for sediment flow and creep were 2.9 and 1.2, respectively, over all sixteen runs in Set V. The corresponding average volume levels were 2.3 and 0.9. These levels suggest that sediment movement was predominantly driven by discrete granular flows. Considering only the runs with initial slope angles within the range of the terrestrial sets (20°-42°), the average activity levels for discrete flow and creep were 4.6 and 1.8; while the average volume levels were 4.6 and 1.4. This suggests that the dominance of discrete granular flow increases with steepening initial slope angles, consistent with the observations of Sylvest et al. (2018), that discrete flow behaviour

appeared to be dependent on initial slope angle, flow events becoming larger and more frequent with steeper angles. For slopes near the angle of repose, flows often appeared to skim over, without disrupting, the downslope surface (Sylvest et al., 2018). Although less dominant than discrete flow, creep was detected at slope angles from 10° to near the angle of repose. Discrete flows frequently produced clearly defined areas of erosion and deposition, as well as small scarp-like features on eroded faces (Sylvest et al., 2018).

### 4.4.6 Set VI (runs 48 & 49) Coarse Sand under Martian Conditions

Minute creep movement was observed in both runs with coarse sand, primarily along the retreating edges of sublimating surface frost. However, the scale of those movements was too small to be resolved using close-range photogrammetry (Sylvest et al., 2018). A single small (*c.* 10 mm wide, 20 mm long, <2 mm deep) sediment flow, observed late in run 49, transported a negligible volume of sediment (Sylvest et al., 2018). Estimated activity and volume levels are correspondingly low. The average activity level for sediment flow was 0.5, and the level for creep 1.0. The average volume levels for sediment flow and creep were 0.5 and 1.0, respectively. Given the very low levels of activity and volume transport over only two runs, these observations are perhaps best used as input for additional study.

## 4.5 Discussion

Based on results from laboratory experimentation under martian atmospheric conditions (Table 4.1, Sets IV-VI), Sylvest et al. (2016 & 2018) developed and validated an analytical model for the triggering of mass wasting by sublimating $CO_2$ frost, condensed within the pore space of unconsolidated sediment slopes. Observations from Sets I-III, under terrestrial atmospheric conditions, provide additional support for this model. The wide variety of

experimental conditions and procedures for the six sets of experiments provide a rich basis for comparisons. Here, our primary focus is on identifying similarities and differences associated with terrestrial atmospheric conditions compared to martian conditions. Sylvest et al. (2016 & 2018) provide detailed observations and analyses of the variations between runs under martian conditions. Figure 4.10 summarises the estimated activity and volume transport levels for all six sets of experiments, but only includes runs in Sets IV and V with initial slopes consistent with those of the terrestrial runs, 24°-42° (Table 4.1).

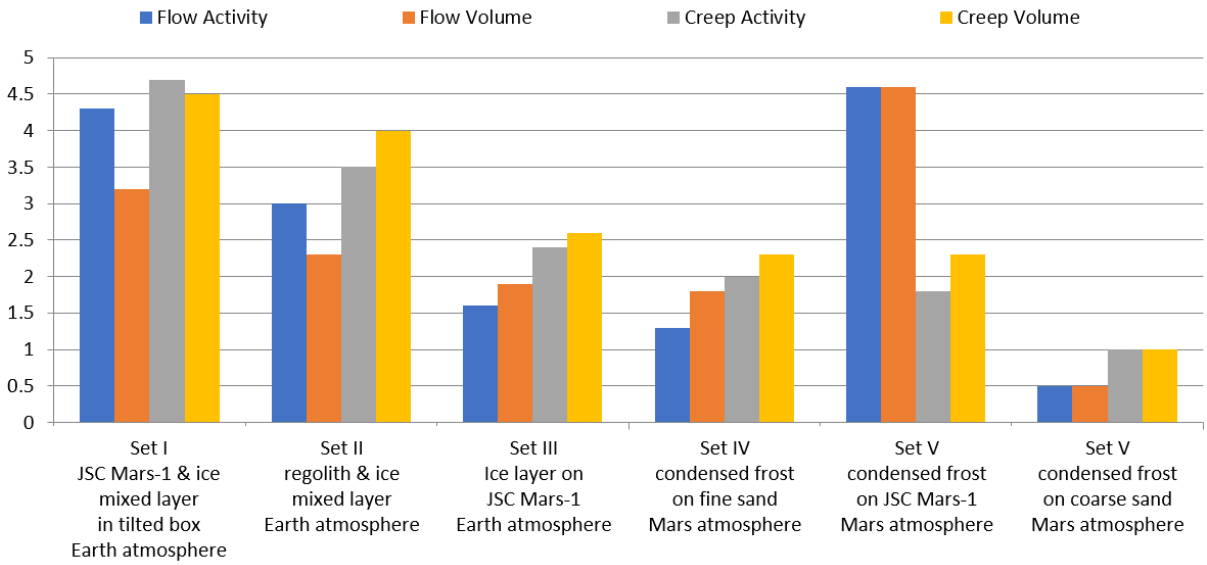


**Figure 4.10.** Estimated activity and volume transport levels for slope angles within the range of terrestrial runs (24°-42°).

### 4.5.1 Sets I & II

Set I had the highest levels of activity and volume transport (Figure 4.10). Several differences between this set and the others may contribute to the higher levels. Perhaps the most significant difference was the configuration of the slope as layers of sediment and $CO_2$ ice, parallel to the smooth, sloping bottom of the Lexan box. The reduced friction of the smooth box provided a plane of structural weakness within the slope, not present in the configurations of the other sets. The arrangement also allowed air to circulate beneath the bottom of the box (Figure

4.2), providing only ~1 cm of sediment to insulate the ice layer from below, possibly enhancing the rate of sublimation. To evaluate this latter effect, run 15 was configured to provide an insulating mass of sediment below the ice, comparable to the configuration of Set II (Figure 4.4D). For run 15, the averaged activity and volume levels for flow and creep combined were 3.5 and 2.5, respectively; a clear reduction from the Set I mean levels of 4.5 and 3.9 (Table 4.1 and Figure 4.10). This reduction suggests that the lack of bottom insulation for Set I is likely responsible in part, for the higher levels of activity and transport. The combined activity level for run 15 was still slightly higher than the Set II level of 3.3, which might imply some effect due to the smooth, sloping box bottom, but the difference is well within the variation in levels within Set II (Table 4.1).

### 4.5.2 Sets II & III

The only significant difference in the preparation of Sets II and III was in the placement of the crushed $CO_2$ ice on the surface of the slopes for Set III, as opposed to incorporating the ice into the top layer of sediment. The slopes for Sets II and III were all comprised of JSC Mars-1 (with the exception of run 13 from Set II, which used fine sand as described above), initially near the angle of repose. The estimated activity and volume transport levels for Set III were significantly lower than those of Set II (Figure 4.10). While there was some sediment transport, sublimation of ice on the surface of the slope did not trigger substantial sediment movement. For both terrestrial and martian atmospheric conditions, sediment movement appeared to be attenuated by the induration of the surface where large areas were covered with relatively thick layers of $CO_2$ ice.

Run 17 was similar to the other runs in Set III, with the exception of the burial of a combination of $CO_2$ and $H_2O$ ice within the top several centimetres of the slope. Contrary to the expectation that run 17 might behave similarly to the runs in Sets I and II, which similarly had ice mixed into the sediment, the activity and sediment transport levels were significantly lower. The level of combined creep and flow activity was estimated at 1.0, and the combined volume transport level at 2.0, both lower than the average combined levels for Set III - 2.0 for activity and 2.3 for volume transport.

### 4.5.3 Set IV – Fine sand

Although the initial slope geometry for the runs in Set IV were similar to those in Sets II and III, there were three significant differences: (1) the use of fine sand versus JSC Mars-1, (2) condensation of the $CO_2$ frost *in situ* and (3) sublimation of the frost under martian atmospheric conditions. With regard to the sediment, fine sand was used for all of the runs in Set IV, whereas Sets II and III used JSC Mars-1, with the exception of run 13. The fine sand slope of run 13, displayed higher combined activity and volume transport levels (each 4.0) than the average levels for Set II (activity was 3.3 and volume transport 3.2). Run 13 was significantly more active than the Set IV runs at comparable slope angles, which had a combined activity level of 2.2, and combined volume level of 2.7 (Table 4.1). While direct measurement of the ice volume was not made for run 13, a rough estimate based on the procedure for Set II is on the order of 140 $cm^3$. This is double the highest reported volume of $CO_2$ frost for Set IV by Sylvest et al. (2018), likely accounting for some, if not all of the increases in activity and volume levels.

The decrease in estimated activity and volume transport levels from Set II to Set IV (Figure 4.10) is consistent with the analytical model of Sylvest et al. (2018), which predicts

reductions of internal friction angle of 17.6° for JSC Mars-1 under terrestrial conditions, compared to 5.1° for fine sand under martian conditions (including the effect of reduced gravity relative to Earth). The estimated levels of activity and volume transport for Set IV were only slightly lower than those for Set III; both sets having significantly lower estimated levels than Set II. In other words, the activity and volume transport levels under martian conditions for the sublimation of frost condensed on fine sand slopes were only slightly lower than the levels for crushed $CO_2$ ice on the surface of JSC Mars-1 slopes under terrestrial conditions (Figure 4.10). This result neither supports nor contradicts the Sylvest et al. (2018) analytical model, as that the model is explicitly based on ice sublimating from within the slope pore space. For Set IV, the model suggests a reduction in activity and volume transport for fine sand compared to JSC Mars-1, ultimately due to the sediment properties. While for Set III, strictly based on our observations, accumulations of surface ice are weaker sources of sublimating gas to raise pore pressure and ultimately trigger sediment movement. So, although two distinct mechanisms are at work, both tend to reduce triggering of mass wasting.

### 4.5.4 Set V – JSC Mars-1

Based on the runs in Set V, Sylvest et al. (2016 & 2018) reported that $CO_2$ frost condensed on/in slopes of JSC Mars-1 regolith simulant triggered both creep and granular flow on slopes down to 17°, under martian atmospheric conditions. Sets I-III demonstrated that creep and granular flow were also active and transported substantial volumes of sediment for JSC Mars-1 slopes under terrestrial conditions when $CO_2$ ice was in the near-surface of the slope, for initial angles down to 24°. Considering only those runs with initial slope angles between 24°-42° (the range for Sets I-III), the estimated activity and volume transport levels for sediment flow are notably higher for Set V than for any other set.

In order to assess the effect of the sublimation process under martian versus terrestrial atmospheric conditions, we focus on Set II, which provides the most direct comparison to Set V. Both sets used slopes of JSC Mars-1 near the angle of repose, and both had some proportion of $CO_2$ frost within the top layers of the slopes. Although Set I also used JSC Mars-1 near the angle of repose, comparisons between Set I and Set V are complicated by the high levels of activity and volume transport for Set I, thought to be an artefact of the smooth, sloped bottom of the box used for those runs. The combined activity and volume transport levels are similar for both Sets II and V; 3.3 and 3.2, respectively for Set II; 3.2 and 3.5 for Set V. However, Set V exhibited a strong dominance of discrete granular flow over creep, both in terms of activity level and volume transport (Figure 4.10). This is in contrast to the somewhat lesser dominance of creep over granular flow for Set II.

We propose that the controlling factor for the dominance of creep or granular flow is the pressure gradient between the pore space and the atmosphere, higher gradients expected to yield more explosive sediment movements consistent with the observed small-scale granular flows in most JSC Mars-1 runs. For a given sediment, the maximum attainable pore pressure is constrained by the rate of gas production, and hence sublimation. When the rate of sublimation is relatively low, pore pressure may rise to a level sufficient to trigger creep; granular flow requiring more rapid accumulation of pore pressure to provide the sudden impulse to trigger. Blackburn et al. (2010) developed a heat transfer-based model for the sublimation rate of $CO_2$ under martian conditions (Eq. 1).

$$E_S = \frac{\left(\sigma(1-\alpha)(T_W^4 - T_S^4)\right) + \left(\frac{k_{CO_2}(T_{atm} - T_S)}{L}\right)}{\rho_{ice}\Delta H^{sub}_{T_s,P_{atm}}} \quad (1)$$

where: $E_S$ is rate of $CO_2$ ice sublimation in units of thickness over time. The numerator on the right-hand side of the equation is the sum of the radiative heat transfer between the chamber walls and the surface of the ice, and the conductive heat transfer between the chamber atmosphere and the ice. The denominator represents the latent heat of the sublimating ice mass. $T_W$ is the temperature of the chamber walls, $T_s$ is the temperature of the ice surface and $T_{atm}$ is the temperature of the chamber atmosphere. (See Table 4.3 for a full list of variables and their definitions). In the cold-room, the lowest temperature of the walls and atmosphere was ~6°C, while the temperature of the $CO_2$ ice was ~-79°C. The wall temperature for the MSC was ~20°C, and at the start of sublimation, the $CO_2$ ice was ~-112°C. Using the property values from Blackburn et al., (2010), strictly for purposes comparing the relative effect of the temperature differences in the cold-room and MSC, the sublimation rate using Eqn. 1 was ~17% higher in the MSC than in the cold-room.

Likewise, the Knudsen-Langmuir equation predicts a higher rate of sublimation in the MSC than the cold-room, due to larger difference between the saturated vapour pressure of the $CO_2$ frost and the partial pressure of atmospheric $CO_2$ (~61 bar at 20°C for the MSC and ~41 bar at 6°C for the cold-room). While neither of these models, Blackburn et al., (2010) nor Knudsen-Langmuir explicitly address both temperature and pressure gradients, each predicts significantly higher rates of sublimation under martian atmospheric conditions. We assert that the higher sublimation rate under martian atmospheric conditions also accounts for evidence of gas entrainment, which was only observed under martian atmospheric conditions (Sylvest et al., 2018). Once creep is established, the pore pressure in the vicinity of the creep has a potential mechanism for relieving the stress in the slope, which might tend to suppress granular flow in that region, unless the creep itself results in destabilising the slope through over-steepening.

### 4.5.5 Set VI – Coarse sand

Set VI was the least active of the six sets. Due to the lack of observed activity (Sylvest et al., 2018), only two runs were executed for this set, which used coarse sand near the angle of repose. Volume transport for Set VI was limited to the finer grain fraction of the slope and was on the order of the photogrammetric noise in the quantitative analysis of Sylvest et al. (2018). The large proportion of coarse grains (Figure 4.11) is thought to allow evolving gas to escape more readily than fine grains, preventing substantial increase of pressure in the pore space (Sylvest et al., 2018).

## 4.6 Conclusions

- Like condensed $CO_2$ frost under martian atmospheric conditions, granular $CO_2$ mixed into the top ~1 cm of regolith did trigger creep and granular flows. This supports the model proposed by Sylvest et al. (2016) that suggests that $CO_2$ condenses within the regolith pore space, allowing an increase of pore pressure which can trigger grain movements.

- When restricted to the slope surface, the sublimation of $CO_2$ ice was much less effective than subsurface ice as a triggering mechanism for mass wasting under both martian and terrestrial conditions.

- Evidence of gas entrainment was only observed under martian atmospheric conditions, likely due to the smaller difference between the vapour pressure of the $CO_2$ ice and the partial pressure of atmospheric $CO_2$ under terrestrial conditions.

- For slopes between 24° and 42°, creep was the dominant form of mass wasting in all cases, other than slopes of JSC Mars-1 under martian atmospheric conditions.

- The dominance of granular flow over creep for JSC Mars-1 under martian conditions may be the result of the faster increase of pore pressure, due to the higher rate of sublimation compared to terrestrial conditions. We have shown that both the Knudsen-Langmuir equation and the Blackburn et al. (2010) heat transfer-based model predict substantially higher rates of sublimation (*c.* 50% and *c.* 17%, respectively), based on our experimental conditions. Variations in atmospheric temperature and pressure on Mars, combined with variations in surface temperature, may result in a corresponding range of sublimation rates, based on location and season, which may in turn trigger both creep and sediment flow. Future modelling efforts are needed to assess the viability of this hypothesis.

- Finally, we wish to encourage experimental planetary geomorphological studies, even when simulation facilities like the MSC are not available. The cost and complexity of work in a vacuum chamber demand a level of preparedness, both in terms of experimental plan and procedure, which is facilitated by exploratory work outside the chamber. The terrestrial environment can also serve as a control for comparisons with chamber results.

## 4.7 Acknowledgements

We thank Dr. Casey Owen Hanning, Department of Poultry Science, University of Arkansas, for providing us with long-term access to the walk-in freezer. We also thank Gen Ito for his collaboration, as well as hours of his diligent and enthusiastic work in the cold-room.

Funding was provided for MES by the Open University, the Sturgis International Foundation, the University of Arkansas Graduate School, the Royal Astronomical Society and Europlanet. JNM acknowledges funding from NASA MFRP NNX14AO21G. Europlanet 2020 R.I. has received funding from the European Union's Horizon 2020 research and innovation programme under grant agreement no. 654208.

## 4.8 References

Barnes, A., 2011. Close-range photogrammetry: A guide to good practice. [WWW Document]. *Guides to Good Practice*, Archaeology Data Service, University of York, UK. URL http://guides.archaeologydataservice.ac.uk/g2gp/Photogram_Toc.

Blackburn, D.G., Bryson, K.L., Chevrier, V.F., Roe, L.A., White, K.F., 2010. Sublimation kinetics of $CO_2$ ice on Mars. *Planetary Space Science,* 58(5), pp.780-791. https://doi.org/10.1016/j.pss.2009.12.004.

Diniega, S., Hansen, C.J., McElwaine, J.N., Hugenholtz, C.H., Dundas, C.M., McEwen, A. S., Bourke, M.C., 2013. A new dry hypothesis for the formation of martian linear gullies. *Icarus*, 225(1), pp.526–537. https://doi.org/10.1016/j.icarus.2013.04.006.

Dundas, C.M., Diniega, S., Hansen, C.J., Byrne, S., McEwen, A.S., 2012. Seasonal activity and morphological changes in martian gullies. *Icarus,* 220(1), pp.124–143. https://doi.org/10.1016/j.icarus.2012.04.005.

Dundas, C.M., Diniega, S., McEwen, A.S., 2015. Long-term monitoring of martian gully formation and evolution with MRO/HiRISE. *Icarus,* 251, pp.244–263. https://doi.org/10.1016/j.icarus.2014.05.013.

Dundas, C.M., McEwen, A.S., Diniega, S., Byrne, S., Martinez-Alonso, S., Alonso, S.M., Martinez-Alonso, S., 2010. New and recent gully activity on Mars as seen by HiRISE. *Geophysical Research Letters*, 37(7). https://doi.org/10.1029/2009GL041351.

Dundas, C.M., McEwen, A.S., Diniega, S., Hansen, C.J., Byrne, S., McElwaine, J.N., 2017. The formation of gullies on Mars today. *In*: Conway, S.J., Carrivick, J.L., Carling, P.A., de Haas, T. & Harrison, T.N. (eds) *Martian Gullies and their Earth Analogues.* Geological Society, London, Special Publications, 467. https://doi.org/10.1144/SP467.5

Hansen, C.J., Bourke, M., Bridges, N.T., Byrne, S., Colon, C., Diniega, S., Dundas, C., Herkenhoff, K., McEwen, A., Mellon, M., Portyankina, G., Thomas, N., 2011. Seasonal Erosion and Restoration of Mars' Northern Polar Dunes. *Science (New York, N.Y.),* 331(6017), pp.575–578. https://doi.org/10.1126/science.1197636.

Hansen, C.J.J., Diniega, S., Bridges, N., Byrne, S., Dundas, C., McEwen, A., Portyankina, G.,

2015. Agents of change on Mars' northern dunes: $CO_2$ ice and wind. *Icarus*, 251, pp.264-274. https://doi.org/10.1016/j.icarus.2014.11.015.

Mc Keown, L.E., Bourke, M.C., McElwaine, J.N., 2017. Experiments On Sublimating Carbon Dioxide Ice And Implications For Contemporary Surface Processes On Mars. *Scientific Reports*, 7(1), p.14181. https://doi.org/10.1038/s41598-017-14132-2.

Pasquon, K., Gargani, J., Massé, M., Conway, S.J., 2016. Present-day formation and seasonal evolution of linear dune gullies on Mars. *Icarus*, 274, pp.195–210. https://doi.org/10.1016/j.icarus.2016.03.024.

Pasquon, K., Gargani, J., Nachon, M., Conway, S.J., Massé, M., Jouannic, G., Balme, M.R., Costard, F., Vincendon, M., 2017. Are the different gully morphologies due to different formation processes on the Kaiser dune field? *In*: Conway, S.J., Carrivick, J.L., Carling, P.A., de Haas, T. & Harrison, T.N. (eds) *Martian Gullies and their Earth Analogues.* Geological Society, London, Special Publications, 467.

Raack, J., Reiss, D., Appéré, T., Vincendon, M., Ruesch, O., Hiesinger, H., 2015. Present-day seasonal gully activity in a south polar pit (Sisyphi Cavi) on Mars. *Icarus*, 251, pp.226-243. https://doi.org/http://dx.doi.org/10.1016/j.icarus.2014.03.040.

Sylvest, M., Dixon, J., Conway, S., Patel, R., McElwaine, J., Hagermann, A., Barnes, A., 2018. $CO_2$ sublimation in martian gullies: laboratory experiments at varied slope angle and regolith grain sizes, *In*: Conway, S.J., Carrivick, J.L., Carling, P.A., de Haas, T. & Harrison, T.N. (eds) *Martian Gullies and their Earth Analogues.* Geological Society, London, Special Publications. https://doi.org/10.1144/SP467.11.

Sylvest, M.E., Conway, S.J., Patel, M.R., Dixon, J.C., Barnes, A., 2016. Mass wasting triggered by seasonal $CO_2$ sublimation under Martian atmospheric conditions: Laboratory experiments. *Geophysical Research Letters*, 43, 12,363-12,370. https://doi.org/10.1002/2016GL071022.

## 4.9 Appendix

### Table 4.2. Summary of experimental parameters.

| Run ID | Set | Regolith | Initial Slope | Mean Relative Humidity (%) | Mean Pressure (mbar) | Mean Temperatures (°C) | | | | | Duration (s) |
|---|---|---|---|---|---|---|---|---|---|---|---|
| | | | | | | Atmosphere | Regolith | | Slope Surface | | |
| | | | | | | | Initial | Final | Initial | Final | |
| 1 | I | JSC Mars-1 | 30.5° | n/d | 1000 | 3.3 | -48.7 | 7.9 | -40.7 | 8.6 | 1800 |
| 2 | I | JSC Mars-1 | 24° | 58 | 1000 | 7.0 | -66.2 | -27.8 | -50.3 | -18.5 | 1800 |
| 3 | I | JSC Mars-1 | 29° | 76 | 1000 | 5.0 | -40 | 3.8 | -39.0 | 4.7 | 1800 |
| 4 | I | JSC Mars-1 | 20° | 72 | 1000 | 6.0 | -55.5 | 4.4 | -40.3 | 6.8 | 1740 |
| 5 | I | JSC Mars-1 | 34° | 77 | 1000 | 6.0 | -65.4 | -1.5 | -53.0 | 4.9 | 1740 |
| 6 | I | JSC Mars-1 | 28° | 72 | 1000 | 6.0 | -58.7 | 1.9 | -52.3 | 5.8 | 2460 |
| 7 | I | JSC Mars-1 | 24° | 57 | 1000 | 10.0 | n/d | n/d | n/d | n/d | 3000 |
| 8 | I | JSC Mars-1 | 31° | 79 | 1000 | 7.0 | n/d | n/d | n/d | n/d | 2700 |
| 9 | I | JSC Mars-1 | 23° | 56 | 1000 | 13.0 | n/d | n/d | n/d | n/d | 2940 |
| 10 | I | JSC Mars-1 | 26° | n/d | 1000 | 2.7 | n/d | n/d | n/d | n/d | 3240 |
| 11 | I | JSC Mars-1 | 28° | n/d | 1000 | 2.8 | n/d | n/d | n/d | n/d | 3180 |
| 12 | II | JSC Mars-1 | 36° | n/d | 1000 | n/d | n/d | n/d | n/d | n/d | 6780 |
| 13 | II | Fine Sand | 30° | n/d | 1000 | n/d | n/d | n/d | n/d | n/d | 3960 |
| 14 | II | JSC Mars-1 | 26.9° | n/d | 1000 | n/d | n/d | n/d | n/d | n/d | 5520 |
| 15 | II | JSC Mars-1 | 30° | n/d | 1000 | n/d | n/d | n/d | n/d | n/d | 4020 |
| 16 | III | JSC Mars-1 | 25.1° | 55 | 1000 | 11.2 | -17.0 | -2.0 | -25.3 | -10.5 | 3900 |
| 17 | III | JSC Mars-1 | 26° | 51 | 1000 | 12.0 | -14.0 | 5.2 | -28.8 | 9.8 | 3934 |
| 18 | III | JSC Mars-1 | 24.3° | 61 | 1000 | 8.1 | -18.8 | -11.7 | -41.8 | -9.0 | 2460 |
| 19 | III | JSC Mars-1 | 31.6° | 57 | 1000 | 9.0 | -19.2 | 7.1 | -4.9 | 7.0 | 3360 |
| 20 | III | JSC Mars-1 | 46.1° | 58 | 1000 | 9.1 | -19.7 | 7.0 | -32.5 | 6.8 | 3720 |
| 21 | III | JSC Mars-1 | 42.4° | 66 | 1000 | 9.2 | -5.6 | 5.7 | -11.0 | 6.3 | 2400 |
| 22 | III | JSC Mars-1 | 31.4° | 63 | 1000 | 8.5 | -10.3 | 5.7 | -10.0 | 1.2 | 1500 |
| 23 | III | JSC Mars-1 | 34.2° | 65 | 1000 | 7.3 | -11.9 | 2.8 | -38.0 | 7.8 | 2400 |
| 24 | IV | Fine Sand | 12.0° | 0 | 6 | 20 | -132.2 | -62.5 | -120.3 | -31.3 | 6884 |
| 25 | IV | Fine Sand | 16.9° | 0 | 6 | 20 | -124.7 | 10.6 | -118.3 | 12.7 | 7042 |
| 26 | IV | Fine Sand | 22.0° | 0 | 6 | 20 | -142.9 | -59.2 | -133.1 | -30.9 | 7524 |
| 27 | IV | Fine Sand | 23.3° | 0 | 6 | 20 | -139.9 | -64.1 | -123.7 | -38.7 | 6960 |
| 28 | IV | Fine Sand | 24.3° | 0 | 6 | 20 | -141 | -34.8 | -128.4 | -40.3 | 6480 |
| 29 | IV | Fine Sand | 31.0° | 0 | 6 | 20 | -135.7 | -116.9 | -127 | -108.7 | 3120 |
| 30 | IV | Fine Sand | 30.4° | 0 | 6 | 20 | -131.9 | -73.4 | -121.5 | -48.7 | 6720 |
| 31 | IV | Fine Sand | 31.0° | 0 | 6 | 20 | -138 | -99 | -122.6 | -84.2 | 6120 |
| 32 | V | JSC Mars-1 | 11.2° | 0 | 6 | 20 | -141.2 | -50.6 | -135 | -25.3 | 6120 |
| 33 | V | JSC Mars-1 | 14.5° | 0 | 6 | 20 | -139.4 | -47.2 | -133.8 | -13.6 | 6060 |
| 34 | V | JSC Mars-1 | 15.2° | 0 | 6 | 20 | -142.1 | -50.5 | -134.6 | -24.8 | 6120 |
| 35 | V | JSC Mars-1 | 17.5° | 0 | 6 | 20 | -142.6 | -51.4 | -132.4 | -21.4 | 6120 |
| 36 | V | JSC Mars-1 | 18.6° | 0 | 6 | 20 | -140.9 | -44.9 | -127.3 | -0.6 | 6180 |
| 37 | V | JSC Mars-1 | 17.4° | 0 | 6 | 20 | -140.9 | -45.6 | -128.5 | -7 | 6060 |
| 38 | V | JSC Mars-1 | 18.3° | 0 | 6 | 20 | -136.4 | -44.5 | -122.4 | -11.1 | 6060 |
| 39 | V | JSC Mars-1 | 17.8° | 0 | 6 | 20 | -141.1 | -45.1 | -128.6 | -20.4 | 6840 |
| 40 | V | JSC Mars-1 | 18.1° | 0 | 6 | 20 | -140.0 | -51.1 | -133.1 | -18.6 | 8100 |
| 41 | V | JSC Mars-1 | 19.2° | 0 | 6 | 20 | -141.6 | -89.4 | -127.6 | -64 | 6060 |
| 42 | V | JSC Mars-1 | 17.0° | 0 | 6 | 20 | -138.0 | -79.8 | -124.4 | -44.3 | 6060 |
| 43 | V | JSC Mars-1 | 34.1° | 0 | 6 | 20 | -113.0 | -92.1 | -66.2 | -52.6 | 5483 |
| 44 | V | JSC Mars-1 | 26.6° | 0 | 6 | 20 | -143.5 | -61.8 | -120.3 | -25.7 | 7728 |
| 45 | V | JSC Mars-1 | 27.5° | 0 | 6 | 20 | -143.4 | -86.7 | -119.9 | -34.9 | 5373 |
| 46 | V | JSC Mars-1 | 25.0° | 0 | 6 | 20 | -143.6 | -76.3 | -123.3 | -37.8 | 7410 |
| 47 | V | JSC Mars-1 | 29.4° | 0 | 6 | 20 | -120.6 | -55.8 | -122 | -36.8 | 8018 |
| 48 | VI | Coarse Sand | n/d | 0 | 6 | 20 | -135.8 | 12.1 | -124.9 | 13.4 | 7320 |
| 49 | VI | Coarse Sand | 33.8° | 0 | 6 | 20 | -127.9 | -77.2 | -112.2 | -43 | 5520 |

n.d. – no data.

**Table 4.3. Definition of symbols**

| Symbol | Definition | Units |
|---|---|---|
| $E_S$ | Sublimation rate | mm $hr^{-1}$ |
| $\sigma$ | Stefan-Boltzmann constant | W $m^{-2}$ $K^{-4}$ |
| $1-\alpha$ | Absorptivity of $CO_2$ ice | |
| $T_W$ | Wall temperature | K |
| $T_S$ | Ice temperature | K |
| $T_{atm}$ | Atmospheric temperature | K |
| $P_{atm}$ | Atmospheric pressure | mbar |
| $L$ | Thermal boundary layer thickness | m |
| $\rho_{ice}$ | Ice density | kg $m^{-1}$ |
| $\Delta H^{sub}_{T_{atm},P_{atm}}$ | Heat of sublimation for CO2 at atmospheric temperature and pressure | J $kg^{-1}$ |

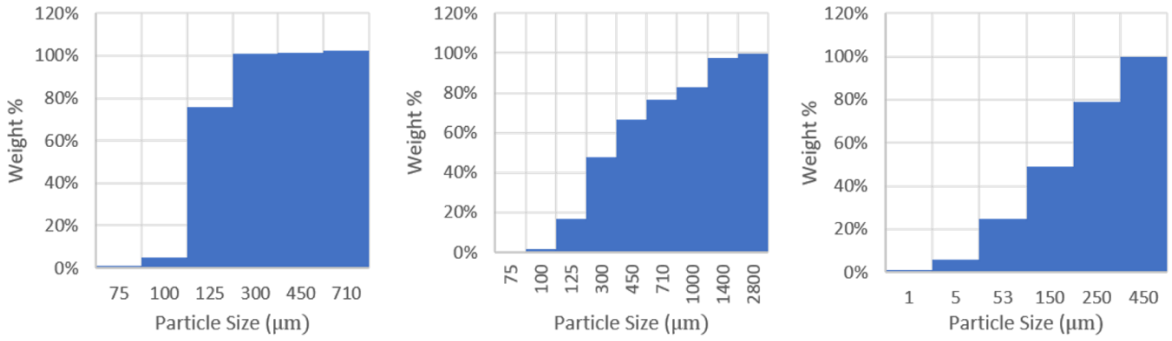


**Figure 4.11.** Grain size distributions for the three regolith simulants used, fine sand (left), course sand (center) and JSC Mars-1 (right).

**Figure 4.12.** Thermocouple placement inside the copper coiled box for Sets IV-VI. The mid-slope thermocouple tree, with three bundled type K thermocouples, is taped to the middle of the box bottom. The larger, rear thermocouple tree has five bundled type K thermocouples. At the far left of image, a single type K thermocouple is affixed to a coded photogrammetric target. This was placed on the surface of the slope. This is a typical arrangement, although for some runs a thermocouple was affixed ~1 cm above the box bottom near the toe of slope (far right in the image).

# 5 Conclusion

In these experiments, we have investigated the ability of $CO_2$ ice sublimation to trigger mass wasting of unconsolidated sediment slopes. We have also broadly constrained the effects of varying initial slope angle and sediment grain size on the frequency of the resulting sediment movements, as well as their type and volume.

## 5.1 JSC Mars-1 Near the Angle of Repose Under Martian Conditions

In our first study under martian atmospheric conditions, we demonstrated for the first time, in the laboratory, that the sublimation of condensed $CO_2$ frost can trigger mass wasting of unconsolidated regolith. These results provide one possible explanation for recent modifications observed in gullies, without the need for liquid water. The observed slope failures were dry granular flows, apparently triggered by the sublimation of $CO_2$ ice condensed in the regolith pore space. Fluidization of regolith over subsurface frost may allow for sediment transport at angles below the dynamic angle of repose. The $CO_2$ frost sublimation trigger mechanism may have broader spatial and temporal applicability on Mars than $CO_2$ slab mechanisms. And, although not directly simulated in these experiments, our results suggest sublimating diurnal $CO_2$ frost may help explain the behavior and distribution of enigmatic martian slope streaks, recently found to correlate with diurnal $CO_2$ frost locations.

## 5.2 Effects of Sediment Grain Size and Initial Slope Angle Under Martian Conditions

In our second study under martian atmospheric conditions, we quantitatively investigated the effect of sublimating condensed $CO_2$ frost on the mass wasting of sediment for three substrate materials, over a range of initial slope angles. The substrates used were fine sand (mean diameter 168 μm), coarse sand (mean diameter 594 μm) and a Mars regolith simulant (JSC

Mars-1); while initial slope angles ranged from 10° to near the angle of repose. We observed four principal movement types: discrete flows, creep, gas entrainment and grain tumbling. The observed sediment movement types were influenced both by initial slope angle and by the nature of the regolith.

Significant volumes of sediment were only transported by discrete flows and creep movements. In fine sand, these processes were only active at slope angles near the angle of repose, and the volumes transported were of the same order as those transported in experiments using JSC Mars-1 at the angle of repose (82 $cm^3$ mean erosion for a surface area of 473 $cm^2$). For JSC Mars-1, these processes continued to transport equivalent volumes of sediment down to 20°, slightly less at 17° and negligible amounts at slope angles <17°.

In our first study, we hypothesized that mass wasting was triggered by a lowering of the static friction angle by gas escaping through the substrate from sublimation. In this second study, we tested this hypothesis by constructing an analytical model describing the physics of this process and found that when applied to our experimental parameters this model successfully predicts the activity observed in our experiments. With this validated model, we were able to predict that, under martian gravity for equivalent sediment types, mass wasting could be triggered at even lower slope angles (movement should be possible for coarse sand near angle of repose, 25° for fine sand and on any slope for JSC Mars-1). This model also reveals that the reduction in permeability in the JSC Mars-1 owing to the presence of fines could be the key parameter for explaining this substrate's enhanced activity range compared with the two sands. These results suggest that the absolute amount of $CO_2$ in the subsurface may control the amount of sediment moved. Further the vertical temperature profiles from these experiments reveal that

$CO_2$ ice emplacement in the subsurface, in terms of vertical distribution and density, is a key parameter to elucidate in order to better understand the limits of sediment transport by $CO_2$ sublimation.

In context on Mars, we found that the $CO_2$ sublimation triggered mass movements observed in our experiments could be applicable for explaining some of the movements seen in present-day, mid-latitude gullies and linear dune gullies. Specifically, our experiments and analytical model reveal that the grain sizes and slopes should be compatible with this type of motion. Some of the features, including movements of meter-scale boulders, levees and lobate termini, are features that would require further experimentation to determine if $CO_2$ sublimation can explain them. Finally, we present the first observations of a creep-like motion caused by $CO_2$ sublimation, which could provide a viable alternative to water–ice freeze–thaw cycles to explain the origin of lobate features often found in association with martian gullies.

### 5.3 Terrestrial *v.* Martian Conditions

In our third study, we compared the results of the first two studies with previously unpublished results from a third series of experiments conducted under terrestrial atmospheric conditions. Like condensed $CO_2$ frost under martian atmospheric conditions, granular $CO_2$ mixed into the top ~1 cm of regolith did trigger creep and granular flows. This supports the model proposed by in the first study, which suggests that on Mars, $CO_2$ condenses within the regolith pore space, allowing an increase of pore pressure which can trigger grain movements. When $CO_2$ ice was restricted to the slope surface, sublimation of the surface ice was a much less effective triggering mechanism for mass wasting than sublimation of subsurface ice, under both martian and terrestrial atmospheric conditions.

Evidence of gas entrainment was only observed under martian atmospheric conditions, likely due to the smaller difference between the vapor pressure of the $CO_2$ ice and the partial pressure of atmospheric $CO_2$ under terrestrial conditions. For slopes between 24° and 42°, creep was the dominant form of mass wasting in all cases, other than slopes of JSC Mars-1 under martian atmospheric conditions. The dominance of granular flow over creep for JSC Mars-1 under martian conditions may be the combined result of fines, restricting the escape of sublimating gas from the slope pore space, and the faster increase of pore pressure, due to the higher rate of sublimation compared to terrestrial conditions.

Finally, we wish to encourage experimental planetary geomorphological studies, even when simulation facilities like the Mars Simulation Chamber are not available. The cost and complexity of work in a vacuum chamber demand a level of preparedness, both in terms of experimental plan and procedure, which is facilitated by exploratory work outside the chamber. The terrestrial environment can also serve as a control for comparisons with chamber results.